

Numerical modelling of detailed interaction of an offshore solar platform array with local hydrodynamics

SENSE-Hub - Activity 3.1



Numerical modelling of detailed interaction of an offshore solar platform array with local hydrodynamics

SENSE-Hub - Activity 3.1

Author(s)

Martin van der Eijk

Désirée Plenker

Erik Hendriks

Numerical modelling of detailed interaction of an offshore solar platform array with local hydrodynamics

SENSE-Hub - Activity 3.1

Client	Rijksdienst voor Ondernemend Nederland (RVO)
Contact	Ruben Hortensius
Reference	MOOI622002
Keywords	Offshore solar, local hydrodynamics, numerical modelling, CFD, flow separation, wake

Document control

Version	1.3
Date	12-08-2024
Project nr.	11209388-002
Document ID	11209388-002-ZKS-0001
Pages	92
Classification	
Status	final

Author(s)

	Martin van der Eijk	Erik Hendriks
	Desiree Plenker	

The allowed use of this table is limited to check the correct order-performance by Deltares. Any other client-internal-use and any external distribution is not allowed.

Doc. version	Author	Reviewer	Approver
1.3	Martin van der Eijk	Lynyrd de Wit	Paul Saager
	Désirée Plenker		
	Erik Hendriks		

Summary

In the coming years, the Dutch government and industry have large ambitions for developing offshore solar (OS) on the North Sea as a part of the energy transition. Currently, it is still uncertain how large-scale roll-out of OS will affect the marine ecosystem. Within the SENSE-Hub project, we aim to close the knowledge gap on the impact of large-scale offshore solar through modelling efforts. A crucial step is to understand how OS arrays interact with the local hydrodynamic conditions. This interaction may lead to the formation of a boundary layer at the water surface and flow separation, thereby leading to a turbulent wake and thus enhanced mixing near the OS array. In this report, we quantify these hydrodynamic processes by modelling them in detail using Computational Fluid Dynamics (CFD), specifically OpenFOAM version 8.0.

This report presents the results of these CFD simulations, where we model an OS array consisting of 5x3 individual solar platforms. These simulations are used to estimate the **turbulent wake size** generated by the array and the **acting forces** and moments on the array itself. We focus on tidal currents only and do not consider wave interaction with the array. Turbulence is modelled using Large-Eddy Simulations (LES), which resolves the smaller turbulent scales. Numerical meshes were set up both in 2D (in fact narrow 3D to accommodate 3D turbulent eddy formation in the LES simulations) and fully 3D. The 2D simulations were required to reduce computational time when assessing wake length. For both the 2D and 3D meshes, we assessed mesh quality and found that the influence of gaps between each solar platform cannot be ignored. Comparing the 2D and 3D results revealed that three-dimensional flow shedding effects are significant, which increases the wake depth beneath the array and shortly downstream. Further downstream of the array, the wake is dominated by the formation of a boundary layer. This meant that we could estimate its length using 2D simulations.

Analysis of the **turbulent wake size** showed that the wake length can be in the order of 0.5 - 1 km for the investigated solar array. Flow separation induced by the array leads to vortex shedding, with a Strouhal number of around 0.06. Analysis of the **acting forces** showed that the pressure forces are several orders of magnitude larger than the viscous forces. A negative heave force was found together with a dominant pitching moment depending on the array dimension.

In our simulations, we varied (amongst others) the following three parameters: (1) **array orientation** relative to the current direction, (2) the **tidal current amplitude**, and (3) the **array length**. The conclusions are separated based on these three variations.

(1) **Array orientation** has a large effect on wake depth, increasing it by a factor of 3. Furthermore, horizontal wake spreading increases by up to 40%, and the forces on the array vary up to several orders of magnitude.

(2) An increase in the **tidal current amplitude**, from 0.4 to 0.8 m/s, decreased the horizontal wake spreading up to 10% while the wake depth hardly changed. The pressure forces seem to scale consistently while viscous forces vary non-linearly. The wake length is not substantially affected.

(3) When the **array length** increases, the frictional forces and wake length are hardly affected. The wake depth increases with array length.

This report provides key insights into the hydrodynamic effects of OS. Ultimately, these findings will contribute to parametrized input for large-scale hydrodynamic and ecosystem models. This will be done in follow-up studies within the SENSE-Hub project.

Contents

	Summary	4
1	Introduction	7
1.1	General information	7
1.2	Brief overview of physical background	7
1.3	Objective	8
1.4	Readers guide	8
2	Solar array layout and hydrodynamic conditions	9
2.1	Representation of solar array	9
2.2	Marine growth	9
2.3	Hydrodynamic conditions	9
3	Methodology and setup	11
3.1	Numerical approach	11
3.2	Model Setup	11
3.2.1	Model domain	11
3.2.2	Boundary conditions	12
3.2.3	Grid	13
3.2.4	Numerical schemes and system solver	13
3.2.5	Reynolds Averaged Navier-Stokes (RANS) simulations	13
3.2.6	Large Eddy Simulations (LES)	14
3.3	Domain and numerical setup	14
3.3.1	Simulations performed in 2D	14
3.3.2	Simulations performed in 3D	16
3.3.3	Solution procedure and initialization	17
3.3.4	Postprocessing	18
4	Mesh quality assessment	20
4.1	Grid convergence study	20
4.2	Wall function criteria & effect	24
4.3	Coverage turbulent kinetic energy	28
4.4	Time coverage 3D-LES	30
5	Analysis of 3D simulations	32
5.1	The effect of gaps between the individual platforms	32
5.1.1	RANS results	32
5.1.2	LES results	33
5.2	Forces & moments	34
5.3	Wake spreading	37

5.4	Wake depth	40
5.5	The effect of current amplitude	42
6	Analysis of 2D simulations	45
6.1	Comparison 2D vs 3D results	45
6.2	Frequency of vortex shedding	47
6.3	Correction force & moment coefficients	48
6.4	Wake length and depth	49
6.5	Effect of array length on forces and wake characteristics	53
6.6	The effect of current amplitude	54
7	Discussion	55
7.1	Comparison with other offshore structures	55
7.2	Recommendations related to CFD	55
8	Conclusions and recommendations	57
9	References	60
A	Simulation results	61
A.1	2D	61
A.1.1	1L – 0.4 m/s	61
A.1.2	2L – 0.4 m/s	63
A.1.3	3L – 0.4 m/s	64
A.1.4	1L – 0.8 m/s	65
A.1.5	1L – 0.4 m/s – rough high-Reynolds wall function	66
A.2	3D	68
A.2.1	0 degree – 0.4 m/s	68
A.2.2	22.5 degree – 0.4 m/s	72
A.2.3	45.0 degree – 0.4 m/s	76
A.2.4	67.5 degree – 0.4 m/s	80
A.2.5	90.0 degree – 0.4 m/s	84
A.2.6	67.5 degree – 0.8 m/s	88

1 Introduction

1.1 General information

In the coming years, the Dutch government and industry have large ambitions for developing offshore solar (OS) on the North Sea as a part of the energy transition. Within the Solar Enhance North Sea Energy Hub (SENSE Hub) project, a consortium of partners investigates the technical, economic, ecological, and legal implications of large-scale deployment of OS.

Within this project, Deltares assesses cumulative ecosystem impacts of OS within offshore wind farms (OWFs). For this, we use a multi-scale modelling approach. We start on a small scale, by investigating how a floating solar platform array interacts with the local hydrodynamics. These results will then be used to parameterize the physical effects of OS, which will be fed into large-scale hydrodynamic and ecosystem models.

This report describes the first step in this approach: the analysis of how a solar platform array interacts with the local hydrodynamics, by modelling it using a Computational Fluid Dynamics (CFD) model. Such an array consists of multiple individual solar platforms connected to each other. Thereby, the total size of a solar platform array can be in the order of hundreds of meters.

In this study, the environmental conditions at the Hollandse Kust Noord Offshore Wind Farm (HKN-OWF) are used. This wind farm is located 18.5 km offshore the Dutch coast, in the west of the Netherlands.

1.2 Brief overview of physical background

The geometry and large extent of the solar platform array make the array comparable to a large flat plate. The interaction of an infinite flat plate with a flowing fluid is a well-established scenario in fluid mechanics. The interaction between the flowing fluid and the rigid plate results in the development of a boundary layer. Outside of the boundary layer, the fluid flow remains unaffected, while inside the boundary layer, the fluid flow is affected due to the viscosity of the fluid. An example of the development of a boundary layer is illustrated in Figure 1.1.

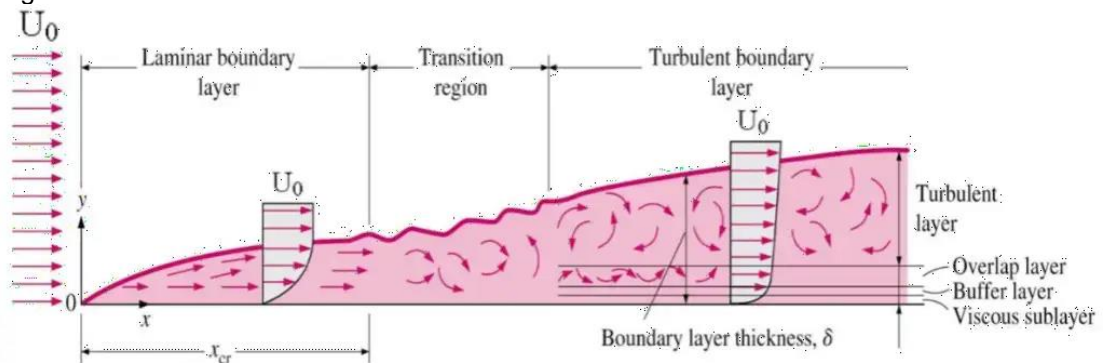


Figure 1.1: Boundary layer development on flat plate resulting eventually in turbulence (Schlichting, 2000).

Within the extent of the boundary layer, described by the boundary layer thickness (δ), the free stream velocity (U_0) is reduced towards the flat plate. The flow within the boundary layer is commonly described by the so-called boundary layer velocity profile, characterizing the flow velocity within the boundary layer parallel to the flat plate. The velocity profile describes the transition from the free stream velocity U_0 to 0 at the flat plate ($y = 0$, see Figure 1.1).

The characteristics of the boundary layer change not only perpendicular to the flat plate but also over the length of the flat plate. The longitudinal development of the boundary layer in Figure 1.1 can be divided into three zones: a laminar part, a turbulent part, and a transition region. The transition of a laminar to a turbulent boundary layer is motivated by the dominance of either viscous or turbulent forces within the boundary layer, which further affects the characteristics of the velocity profile. In the transition region, flow separation happens, and vortices are created. The boundary layer is fully developed as soon as the velocity statistics no longer vary with the distance x (Pope, 2000).

However, although the solar platform is of a large extent, it is finite. To investigate if the turbulent boundary layer can fully develop, the dimensionless Reynolds number can be applied. The Reynolds number Re depends on the flow distance x , the viscosity of water, and the free stream velocity (U_0). According to Patel and Head (1969), the boundary layer flow is fully developed, and no transitional effects are evident anymore for $Re > 3000$. The large extent of the solar platform array (a large x) and the low kinematic viscosity of water results in a high Reynolds number in the order of $Re = 1e7$ and higher. Thus, the interaction with the flow is expected to lead to a fully developed turbulent state and the corresponding turbulent velocity profile. The turbulence due to the interaction with the flat plate further affects the wake and its extent behind the array.

1.3 Objective

The objective of this investigation is to determine to which extent a solar platform array affects the local and surrounding hydrodynamic conditions. By modelling the detailed interaction between the array and the flow dynamics, detailed information on the flow field and turbulence characteristics can be obtained. Based on these, the overall effect can be quantified, which will be used as input for larger-scale models to account for the wake of a solar platform array. The following analysis is performed:

- Acting forces and moments
- Estimation of wake size

To gain a better understanding of the interaction between the array and the flow, the effect of (amongst others) the following aspects will be part of the following investigation:

- Solar array orientation
- Free stream velocity
- Length of the solar array

1.4 Readers guide

This report starts with the methodology and the domain setup in Chapters 1 and 3. In Chapter 4 a mesh quality assessment is discussed. In Chapter 5 a 3D analysis is done of the results on the spreading of the wake for different kinds of environmental conditions. In Chapter 6 the length of the wake for a solar platform array is discussed with 2D simulations. The discussion (Chapter 7) compares the results of a solar array with the wake size of offshore foundations such as monopiles and jackets, and provides specific recommendations for future CFD work. Finally, conclusions and general recommendations are given in Chapter 0. Appendix A consists of contour plane of 2D and 3D simulations for different setups and environmental conditions.

2 Solar array layout and hydrodynamic conditions

The size of a solar platform array can be in the order of kilometres¹. This scale is a couple of orders larger than the characteristic length scales for flow separation and the generation of a boundary layer. The large difference between the size of the boundary layer, the one to capture, the wake, and a solar platform array asked for assumptions to suppress the computational costs of the CFD simulations. These assumptions are well considered such that the relevant physics are still captured.

2.1 Representation of solar array

The solar array is represented as a stiff and fixed structure. Thus, no movements of the solar array due to the interaction with the local hydrodynamics are anticipated in the simulations.

To keep the computational costs of the numerical simulations limited, a limited-size array is studied. This consists of three times eight solar platforms. The solar platforms have a length of 15 meters and a width of 3 meters. The gap between adjacent platforms is 0.4 m. This results in overall array dimensions of length $L = 45.8$ m and a width of $W = 26.8$ m. The submerged depth (d) of the array is 0.15 m (Oceans of Energy, 2023).

In the field, the solar arrays will likely be arranged into significantly larger arrays. However, it is not feasible to investigate a structure of this size with CFD. To get a better understanding of the effect of the array size (length in flow direction) on the development of the boundary layer and successive wake, additional simulations of a thin slice of the solar array with two times ($2L$) and three times ($3L$) the base length are conducted. These simulations are referred to in the following as 2D cases although they are in fact narrow 3D simulations, since the thickness of the slice is negligible in comparison to the dimensions in x and z . A certain amount of cells in y direction is required for solving the turbulence with the LES turbulence model (see Section 3.2.6). The effect of the gaps between the solar platforms is assumed to be small but still considered in the analysis for 3D effects.

2.2 Marine growth

Over the lifetime of the structure, it is expected that marine growth will take place at the submerged part of the solar array. To consider this marine growth, a certain roughness at the bottom of the elements is assumed. This roughness is assessed for the determination of the wall-near velocities. More details on the modelling of the wall near velocities and the deployment of surface roughness will be presented in Section 3.2.3.

2.3 Hydrodynamic conditions

In this study, the interaction between the solar array and a uniform current are investigated. The effect of waves is not part of the investigation. Since waves are influencing the development of a boundary layer and the development of the wake, it is expected that neglecting the effect of waves will result in a larger extent of the wake behind the solar array.

The hydrodynamic conditions in this study are based on the hydrodynamic conditions in the HKN-OWF. The water depth is assumed as constant with a depth of 32 m.

¹ Oceans of Energy, the offshore solar technology developer in the SENSE-Hub project, is working towards a largest standard size offshore solar farm of one by one kilometre squared (approx. 150-200 MW installed capacity).

The current within the domain is assumed to be uniform 0.4 m/s, an average current that is not unusual at HKN-OWF due to tidal effects. However, to investigate the effect of the flow velocity on the interaction with the solar array, also a flow velocity of 0.8 m/s is investigated in a variation of the base simulation.

The effect of waves is not part of this study. However, it is expected that waves will have a significant effect on the development of the boundary layer and, thus, detachment of flow from the platform and consequently on the development of the wake. Waves would induce additional mixing in the water column. By modelling the current only condition, the extent of the boundary layer as well as the wake is likely to be overestimated.

3 Methodology and setup

3.1 Numerical approach

The detailed modelling of the impact of the solar array on local and surrounding hydrodynamics is performed with a CFD approach. The applied software is part of the open-source CFD toolbox OpenFOAM (Weller, 1998), which can solve the interaction between current flows and structures of arbitrary size. Multiple works showed the capabilities of OpenFOAM to capture the flow physics of a boundary layer transition occurring over a flat plate (Beechook, 2015) (Kim M. a., 2019) (Sanjay, 2019).

Due to the large community of open-source software a high number of numerical solvers for specific physical situations as well as libraries, such as turbulence models or meshing tools are available.

For the simulation of the impact of the solar array on local and surrounding hydrodynamics, a one-phase solution is chosen. Thus, the simulation domain is fully submerged, and no free surface is modelled. Since the development of boundary layer flow, flow detachment and wake are expected to be mainly influenced by the resistance of the submerged part of the solar array, the no-slip condition and friction of the solar array bottom, and the development of turbulent features, the simulation of the free surface is not expected to affect the simulation results significantly. By applying a one-phase approach, the computational costs for the simulations are significantly reduced in comparison to a two-phase approach. Further, this study aims to include rather advanced turbulence modelling with LES at a later stage, which is expected to be computationally expensive already for a one-phase solution. Due to the one-phase approach, the pressure presented in this study is equivalent to the dynamic or kinematic pressure component divided by the water density, resulting in pressures with the unit m^2/s^2 .

The simulation is performed with an incompressible, transient OpenFOAM (version 8) application (solver) based on the PIMPLE algorithm. The PIMPLE algorithm combines an inner and an outer iteration loop while solving the governing equations for each timestep. This approach provides a higher stability for unsteady cases and allows to use of larger timesteps without losing accuracy (to a certain extent).

The turbulence in the simulations is modelled via a statistical approach with Reynolds-Averaged Navier-Stokes (RANS) and Large Eddy Simulations (LES). While RANS bring the benefit of being computationally less expensive by modelling only the effect from additional turbulent stresses, LES delivers more detailed results on the turbulent flow by combining the statistical approach of modelling smaller turbulent features via sub-grid modelling while resolving the larger turbulent features.

3.2 Model Setup

3.2.1 Model domain

The computational domain including the solar array is illustrated in Figure 3.1 (top view) and Figure 3.2 (side view). The length of the computational domain is chosen to be 5 times the array length starting at $x = -45.8$ m and ending at 183.2 m. The width of the domain is from $y = -68.7$ m until 68.7 m, which is equivalent to 3 times the length of the array (equal to 5.1 times the width of the array). The chosen domain extent of 5 by 3 array lengths should allow enough space for the development of the wake while avoiding influences from the domain

boundaries. The water depth is 32 m, representing the water depth at HKN-OWF (see section 2.3).

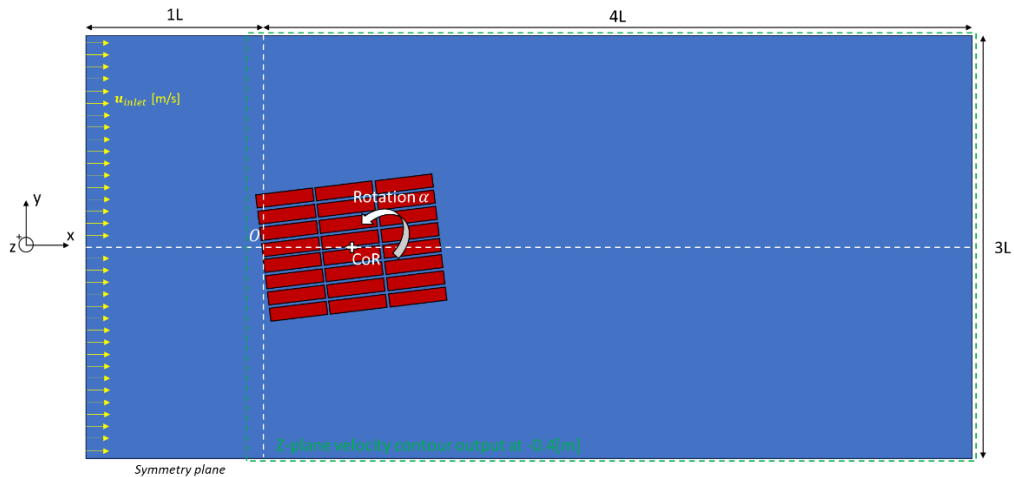


Figure 3.1: Top view of the computational domain for the 3D simulations with a rotation of the solar array of $\alpha = 22.5^\circ$. The origin is given by O. The L stands for the length of the array. CoR means the center of rotation. The green dashed line indicates a z-normal plane that is used in postprocessing for determining the wake development.

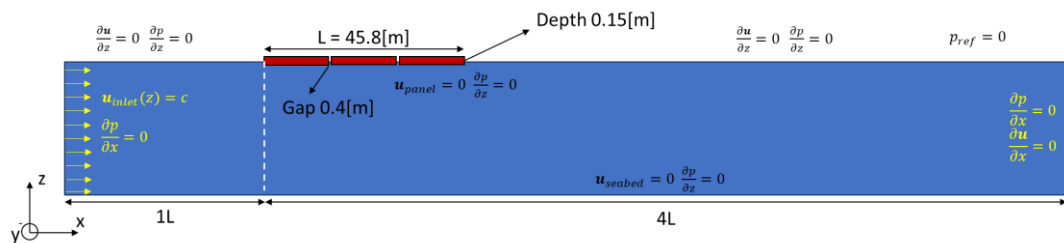


Figure 3.2: Side view of the computational domain. Boundary conditions are given in italic font. The side view is also representative of the 2D simulations (not to scale).

3.2.2 Boundary conditions

The boundary conditions are chosen to resemble the field conditions. The top of the domain is confined by a wall with a free-slip condition for the flow velocity. As a wall, no exchange of mass or momentum can happen over this boundary. The bottom of the domain is treated as a smooth wall and, thus, incorporates a free-slip condition for the velocity. The free-slip condition is chosen since, the water depth is chosen so high, that there is no influence expected between the velocity conditions at the boundary and the flow conditions initiated by the solar array. This assumption has been verified in a sensitivity study. Further, the free-slip conditions reduce computational costs, since resolving the boundary would have required a higher mesh resolution near the boundary.

The x-normal boundary on the left is used as an inlet to initiate the flow in the domain. The velocity is uniform over the boundary and free slip at the domain bottom is applied. In reality there is a vertical gradient in the velocity, but in the top layer at the area of focus this gradient is small. The assumption of a uniform velocity inlet would not affect the interpretation of the boundary layer development around the solar array.

The initial turbulence intensity (given by the turbulent parameters required by the RANS model) defined at the inlet, is based on the assumption of 3% turbulent fluctuations and a turbulent integral length scale of approx. 3 m, being the largest eddy scale expected. The x-normal boundary on the right serves as an outlet. A zero pressure gradient is applied to prevent backward forcing when the wake is not fully diffused.

A reference pressure is defined based on the initial conditions. At the y-normal back and front side of the domain symmetry conditions are applied. At the solar array, partial-slip conditions using a wall function are imposed for the velocity.

3.2.3 Grid

To capture the development of a boundary layer and the flow behaviour within the boundary layer (see section 0), grid refinement is needed at the boundaries representing the solar array. The requirements for the refinement depend on the chosen turbulence model and approach to model the large velocity gradient in the immediate vicinity of the boundary. An indicator to check the refinement concerning the boundary near flow is the dimensionless parameter, representing the required distance from the first calculation point (here equal to the cell centre) to the boundary surface. To capture the large gradient next to the boundary surface either (i) the viscosity-dominated viscous sublayer needs to be sufficiently resolved or (ii) wall functions need to be applied to capture the large gradient while resolving only the Reynolds stress-dominated part of the boundary layer profile (see Figure 3.3). To reduce computational costs, wall functions are applied in this study. The resolution of the grid near the array surface is optimized to satisfy a y^+ value of 5 for resolving most of the turbulent length scales.

The roughness of the surface is considered in the wall functions by the Nikuradse roughness k_s . This is typically a value between 1 and 100 mm for marine growth. In this study, a value of 50 mm is used. The 50 mm is likely to be larger than the first cell with the criteria of $y^+ < 5$ (approx. 1 mm). The influence of applying a rough high-Reynolds wall function over low-Reynolds wall functions needed for low values of y^+ needs to be assessed (see Section 4.2).

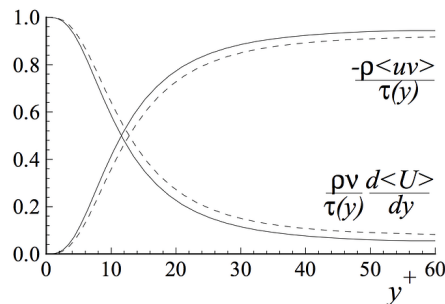


Figure 3.3: Distribution of viscous and Reynolds stresses in the boundary layer based on the distance from the boundary surface indicated by y^+ based on DNS results from (Kim, Parviz, & Moser, 1987) (Pope, 2000).

3.2.4 Numerical schemes and system solver

Discretization in time is performed using the forward Euler scheme. The advective terms are spatially solved using the Gauss linear upwind scheme bounded by a limiter. A Courant number, the maximum a particle can travel in a one-time step concerning a grid cell length, is set to 1.0 to ensure numerical stability, but also the possibility to capture frequency-related effects like shedding.

The system of equations is solved using the PIMPLE algorithm with a tolerance of up to $1e-6$ for all governing variables. The algorithm makes use of 3 inner corrector steps and a maximum of 20 outer corrector steps.

3.2.5 Reynolds Averaged Navier-Stokes (RANS) simulations

The $k\omega$ -SST turbulence model is suitable for determining the boundary layer development on a flat plate (Sanjay, 2019). RANS simulations are performed to reduce the computational costs compared with the Large Eddy Simulations (LES) and for the initialization of these

simulations. The governing equations are averaged to obtain mean equations of fluid flows and model all of the turbulence scales. The initial conditions are based on a turbulence intensity of 3%. RANS simulations are in general known as overestimating the dissipation of the eddies in like jets, strong curvature, and axial strain due to the linear eddy viscosity models. It solves a transport equation to find the eddy viscosity (for all scales) to control the eddies such that they dissipate.

3.2.6 Large Eddy Simulations (LES)

Perform in general better for the prediction of turbulence. Compared to RANS, there is no steady solution, and needs to be used for 3D computational domains to account for vortex stretching. The dynamic k-equation (Kim W.-W. a., 1995) is chosen based on 2D simulations which is only suitable for comparison of models because of the consistency after varying the Courant restriction. Furthermore, it was consistently produced the same shedding frequency being in line with the results of (Rostami, 2019), better than the Smagorinsky model. The wall-adapting local eddy-viscosity (WALE) model showed similar results.

The Van Driest damping function is applied at walls like the array. The function is simplistic and the damping corrects the excessive eddy viscosity predicted by the models near a wall by accounting for the decrease in eddy length scale. Another option are the more sophisticated WALE model, which damps based on the velocity scale.

A LES model needs a filter size that distinguishes which turbulent scales are modelled (smaller than the filter) and resolved (larger than the filter). The filter size is the cubic root of the volume of the corresponding grid cell where the governing equations are solved.

3.3 Domain and numerical setup

3.3.1 Simulations performed in 2D

The simulations performed in 2D are summarized in Table 3.1. The number of grid cells per simulation is in the order of 7 to 8 million cells. The computational domain in Figure 3.4 is lengthened to 500 m ($>10L$) to see how long the wake can be.

We want to emphasize that we call the simulations 2D but also use cells in the y-direction to obtain turbulence. Turbulence is in essence 3D. Using the total 3D computational domain would result in unfeasible computational costs. In y-direction, 11 cells (11 m) are equally distributed for the base mesh. Grid refinements in Figure 3.4 are also performed in y-direction to maintain an aspect ratio near 1, essential for LES simulations.

Another note worthwhile to mention is that in numerical simulations the wake will have a longer extent than in reality. The diffusive effect of turbulence on the wake is in reality larger due to the environmental effects e.g. waves.

The first three simulations that are performed are to determine the grid resolution. A base level size, the size of the coarsest cell is defined: first mesh is 0.5 million with a base level of 2.0 m (dx, dy, and dz), second mesh is 7.6 million with a base level of 1.0 m, and third mesh is 36.7 million cells with a base level of 0.5 m. In Figure 3.4, three refinement zones are shown. The first refinement is with a factor 2 compared to base mesh beginning around 15 m in front and ending around 110 m behind the array, the second refinement is with a factor 4 compared to base mesh beginning around 5 m in front and ending around 55 m behind the array, the third refinement is with a factor 8 just before and after the array, and the last refinement near the solar platform array is a factor 16 compared to base mesh near the array. All refinements are performed in x, y, and z-direction to maintain a cell aspect ratio of 1.

In the last refinement zone, 10 prism layers with a thickness ratio of 1.3 are added to resolve the boundary layer and to meet the y^+ criteria (<5) for the low-Reynolds wall function. This results in a maximum cell height of 0.001 m (dz) at the array.

We need to note that the prism layers are not needed when roughness due to marine growth is considered using rough high-Reynolds wall functions and is discussed in Section 4.2.

In Chapter 4, the mesh quality is discussed in more detail and assessed on several parameters: skewness and aspect ratio, y^+ (wall distance), and in essence for turbulence modelling at least 80% of turbulent kinetic energy resolved.

In the remainder of the study, the middle mesh is used.

Table 3.1: Simulations performed in 2D with different array sizes and domain lengths of 500 m.

Number	Velocity u_{inlet} m/s	Array length [L]
3	0.4	1
4	0.4	2
5	0.4	3

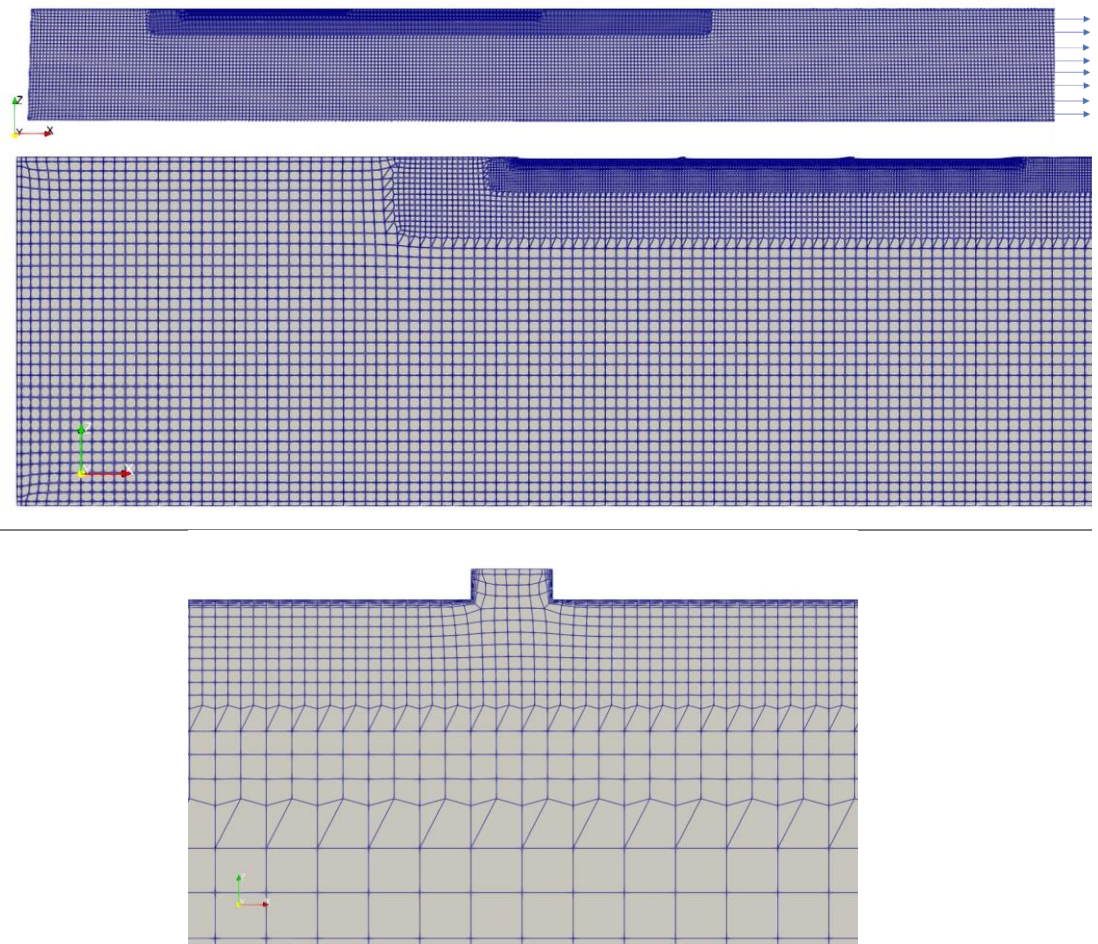


Figure 3.4: Detailed overview of grid for 2D simulations including the boundary layering. Meshing of the domain (top) over the inlet and whole solar array (middle) and detail of the meshing at the gap between two solar platforms (bottom).

3.3.2 Simulations performed in 3D

The simulations performed in 3D are summarized in Table 3.2. The number of grid cells per simulation is in the order of 7~8 million cells. The refinement levels described in Section 3.3.1 are similar for the 3D mesh. However, an additional refinement zone is added. The coarsest cell is 2.0 m with a cell aspect ratio of 1. The first refinement is with a factor 2 compared to base mesh, the second refinement is with a factor 4 compared to base mesh, the third refinement is with a factor 8 compared to base mesh, and the last refinement near the solar platform array is a factor 32 compared to base mesh over an extent of 5 m. All refinements are performed in x, y, and z-direction to maintain a cell aspect ratio of 1. The same prism layers as for 2D are applied.

All the cases are simulated for 1000 seconds such that a water particle at the inlet could travel twice the length of the computational domain with a free stream velocity of 0.4 m/s.

From 2D simulations, it is concluded that the effect of the seabed is negligible (1.25%) on the flow velocity beneath the array. In 3D the amplification will be less due to the non-restricted flow motion. The middle grid in 2D is found as sufficiently accurate and is extruded for the 3D grid to have a comparable grid resolution. For oriented arrays, the refinement zones are stretched based on the corner positions of the total array.

As for the 2D simulations, the 3D mesh quality is assessed in Section 4.

Table 3.2: Simulation performed 3D with array 3 times 8 platforms.

Number	Velocity u_{inlet} [m/s]	Orientation α [deg]
6	0.4	0
7	0.4	22.5
8	0.4	45
9	0.4	67.5
10	0.4	90
11	0.8	67.5

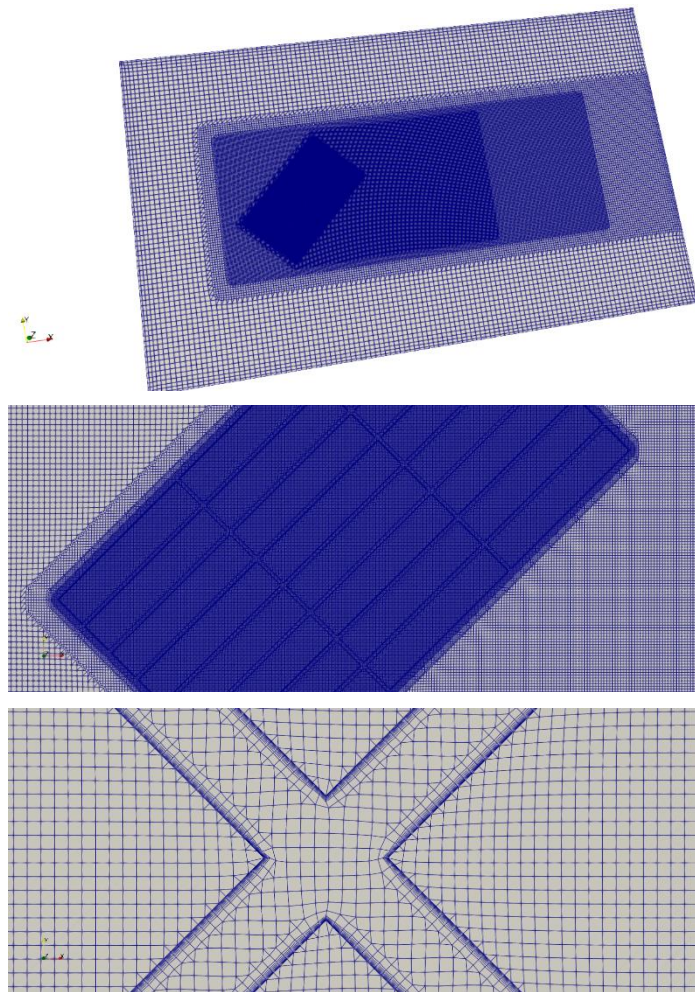


Figure 3.5: Overview of the 3D grid with the orientation of 45° in top view for the whole domain (top), directly at the solar array (middle) and detailed at the gap between solar platforms (bottom).

3.3.3 Solution procedure and initialization

The solution procedure is summarized below for the 3D and 2D simulations:

1. Perform 2D RANS simulations with an array.
 - a. Simulating until 750 s that finds a fully developed profile.
 - b. Check the y^+ criterion around 5 at the array to be sure wall functions can be applied.
 - c. Check if the grid is fine enough such that it can resolve 80% of the turbulent kinetic energy when using LES.

This first step is needed for the initialization of the 3D and 2D simulations and are performed iteratively before starting with the next steps. For the 2D simulations:

1. Map the 2D RANS simulations to the computational domain for LES and use the same inlet conditions.
2. Run LES for another 900 s.
 - a. Note that the restart with LES results in a transition of RANS to LES which needs to be accounted for in the analysis.
 - b. Re-check if 80% of the turbulent kinetic energy is resolved by comparing the total turbulent kinetic energy with the modelled kinetic energy.

For the 3D simulations:

1. Map the 2D RANS simulations and extrude to the 3D computational domain.
2. Perform 3D RANS simulations for the given conditions and orientation.
 - a. Simulating until 750 s that finds a fully developed profile.
 - b. Re-check the y^+ criterion of below 5 at the array to be sure wall functions can be applied.
 - c. Re-check if the grid is fine enough such that it can resolve 80% of the turbulent kinetic energy when using LES.
3. Use the 3D RANS simulations for initialization of LES simulations and perform them.
 - a. Simulation of another 750 s.
 - b. Check for the transition of RANS to LES.
 - c. Re-check if 80% of the turbulent kinetic energy is resolved by comparing the total turbulent kinetic energy with the modelled kinetic energy.

Again both kinds of simulations are iteratively until they match the checks. The last couple of 100 s of the LES simulations are used for post-processing to prevent accounting for the RANS to LES transition.

3.3.4 Postprocessing

During the simulations, the output needs to be generated for performing the analysis of the wake of an array. Two kinds of data are outputted:

Probes measuring on 30 locations over the z-direction with logarithmic spacing up to a depth of 2.5 m beneath the array (see Figure 3.6).

In total 21 probe locations in the XY-plane are used. One of them is fixed in location and used for measuring the undisturbed conditions. The rest rotates with the array. The probes are positioned in any case 1.5 m behind the leading edge of the array or further. This results in a Reynolds number for all probe locations that should correspond with the turbulent region according to (Incropera, 1990). These probes are used for extracting the local instantaneous velocity field. The sampling frequency is 10 Hz to cover the fluctuations.

The output of XY-plane section at multiple heights illustrated in Figure 3.1 by the green dashed line.

The XY-plane is from $x = -1.0$ m until the end of the domain. The z-position is based on the analytical theory of the Blasius turbulent boundary layer thickness (Blasius, 1907) and 2D-performed RANS simulations and should help with determining the extent of the wake. The positions of -0.6 m, -0.4 m, and -0.2 m are used to look at the spreading of the wake. The sampling frequency is 1 Hz for time-averaging purposes.

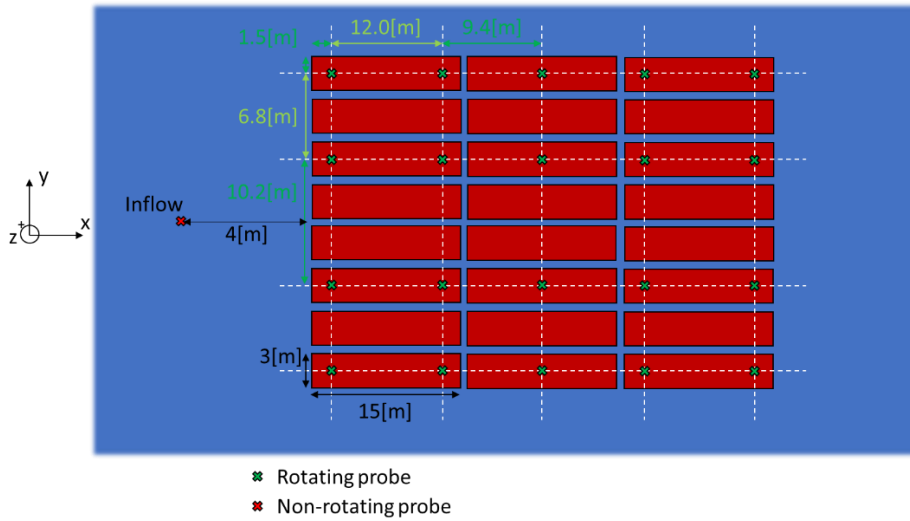


Figure 3.6: Top view zoom-in on the array. Green probes are used for analysing the development of the turbulent boundary layer and rotate with the orientation of the array. The red probe is used for determining the flow amplification.

The output of XZ-plane section at $y = 0.0$ m for 2D simulations.

The XZ-plane is used to determine the depth penetration of the turbulence and the length of the wake. The sampling frequency is 1 Hz for time-averaging purposes.

4 Mesh quality assessment

The mesh quality assessment is conducted to validate a sufficient resolution of the grid to represent the turbulent effects. The assessment is based on three criteria: (1) convergence of the results for grids with different resolutions using 2D RANS results (simulation 1, 2, and 3), (2) the y^+ values at the solar platform should be lower than 30 to have benefits of the applied wall function, (3) resolving at least 80% of the turbulent kinetic energy dominated by the larger scales. Smaller scales are predictable as these behave isotropic.

4.1 Grid convergence study

The study is performed on the XZ-plane and two XY-planes in the 3D computational domain in Figure 3.1 for an orientation of 90° . The first check that is made is the convergence in time. This check is performed for the 3D RANS simulations because LES does not converge in time for this case. The variation of the velocity field from 710 to 750 s is measured for the wake of the array after 45.8 m. The standard deviation for the turbulent kinetic energy (k) is calculated per grid cell using:

$$\sigma = \sqrt{\frac{\sum |k - k_{mean}|^2}{n}},$$

Where the value for n is 5 (every ten seconds) and the mean is the average of the grid cell value over 710 to 750 s. In a similar way the standard deviation for the velocity is calculated.

The standard deviation is normalized by the current velocity of U is 0.4 m/s and the turbulent kinetic energy is normalized by $\frac{3}{2}(UI)^2$ where I is 3% to obtain a percentual value. The solar platform array starts at $x = 0$ m.

The difference showed to be at a maximum 0.06% for the velocity (in front of the solar platform array) and 2.1% for the turbulent kinetic energy (in front of the solar platform array). The percentage of turbulent kinetic energy is higher due to the relatively large increase of turbulent kinetic energy at the beginning of the solar platform, where the value is lower in the wake. The defined time resolution is assumed sufficient for fully developing the flow.

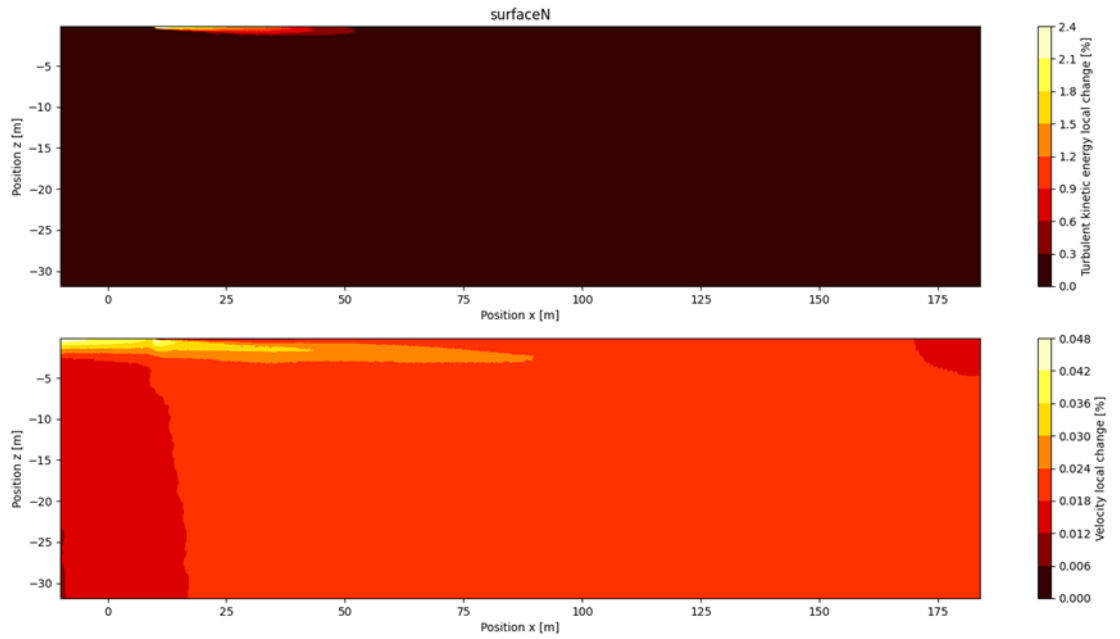


Figure 4.1: XZ-contour planes at $y = 0$ m showing the standard deviation in turbulent kinetic energy and velocity magnitude over 700 to 750 s.

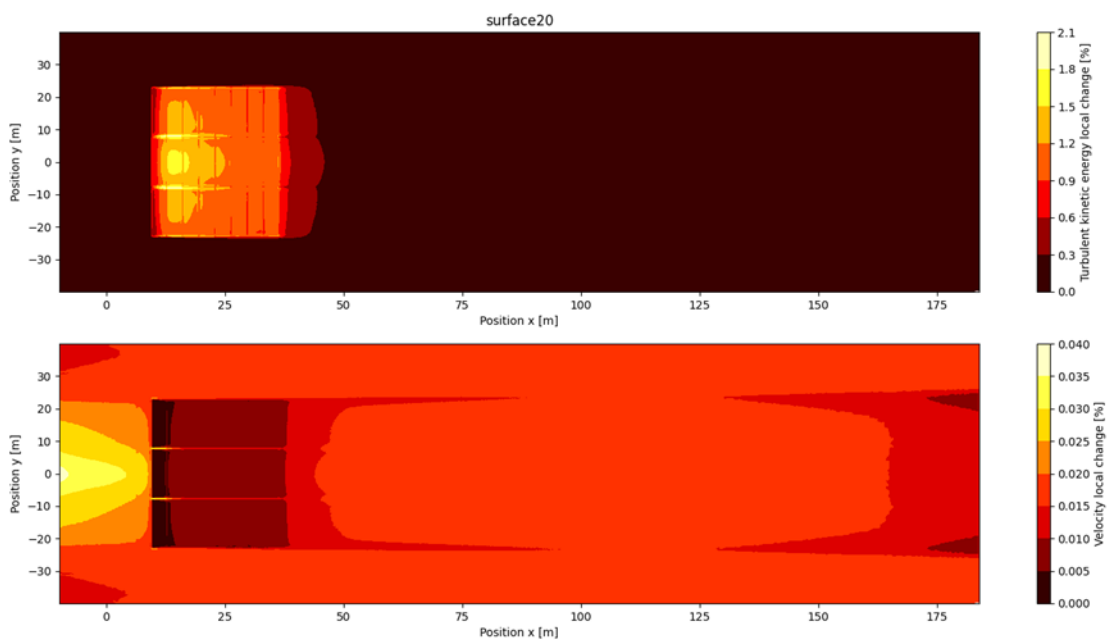


Figure 4.2: XY-contour planes at $z = -0.2$ m showing the standard deviation in turbulent kinetic energy and velocity magnitude over 700 to 750 s.

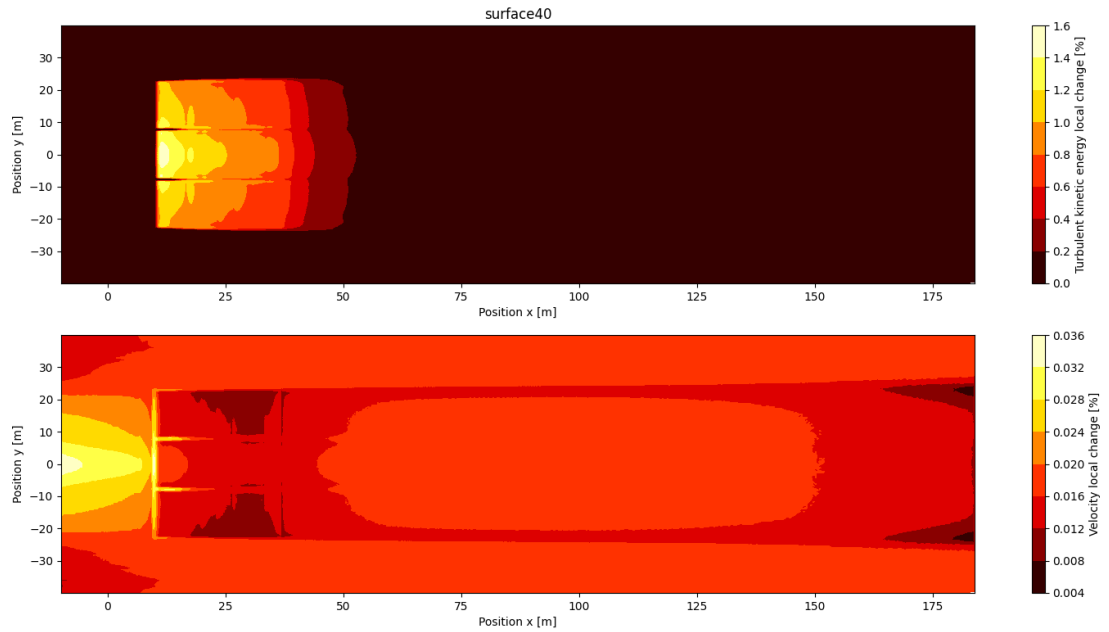


Figure 4.3: XY-contour planes at $z = -0.4$ m showing the standard deviation in turbulent kinetic energy and velocity magnitude over 700 to 750 s.

The convergence in space is analysed using the 2D simulations. Because the 2D grid is the same as the cross-section at the XZ-plane for the 3D simulations, the 2D grid convergence results can be used for 3D. In LES, the very definition of grid convergence is controversial unless the cut-off length scale is completely decorrelated from the computational grid. In our work the LES results from two different grid sizes are averaged over time and then compared to judge grid size sensitivity.

The time-averaged velocity field for the coarse grid and the used-middle grids are plotted. The LES results are averaged over the last 100 s. These are visible in Figure 4.4 and Figure 4.5. The used grid resolution showed still more flow details, read smaller eddies, but similar vertical wake penetration compared to the coarse resolution. The XZ-flow field for both do look similar. The XY-flow field show some difference in between $x = 5-100$ m but further downstream they are more similar. The coarse grid does not show any oscillations anymore after 200 m which could indicate that the grid is too coarse to dissipate the eddies to smaller scales. The middle grid resolution is used in the remainder.

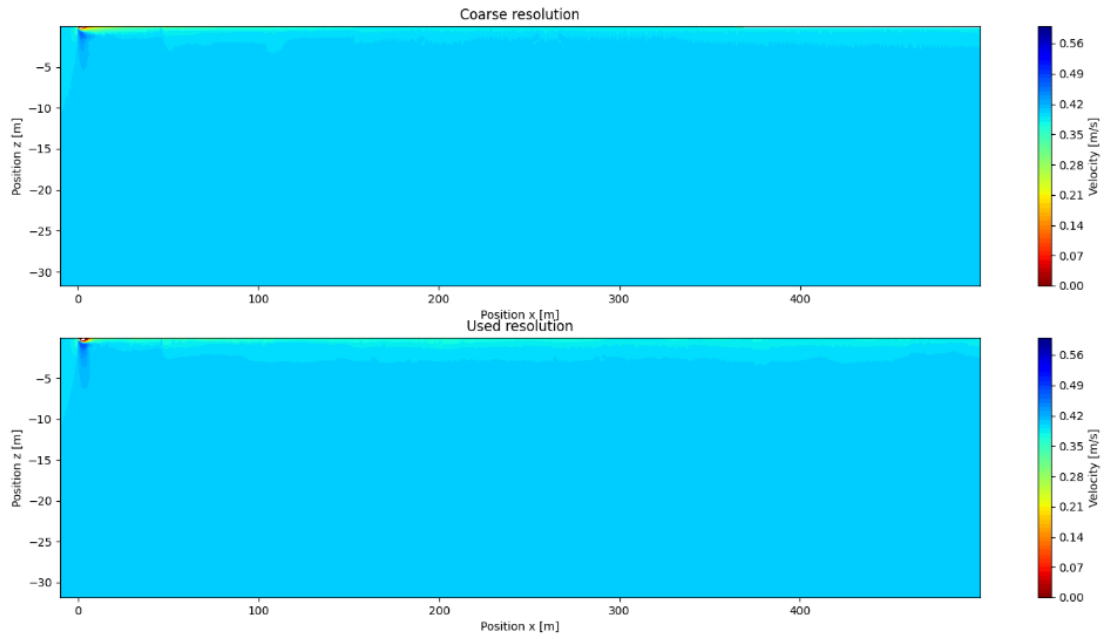


Figure 4.4: XZ-plane of time-averaged 2D LES simulation over the last 100 s for a coarse and middle grid resolution.

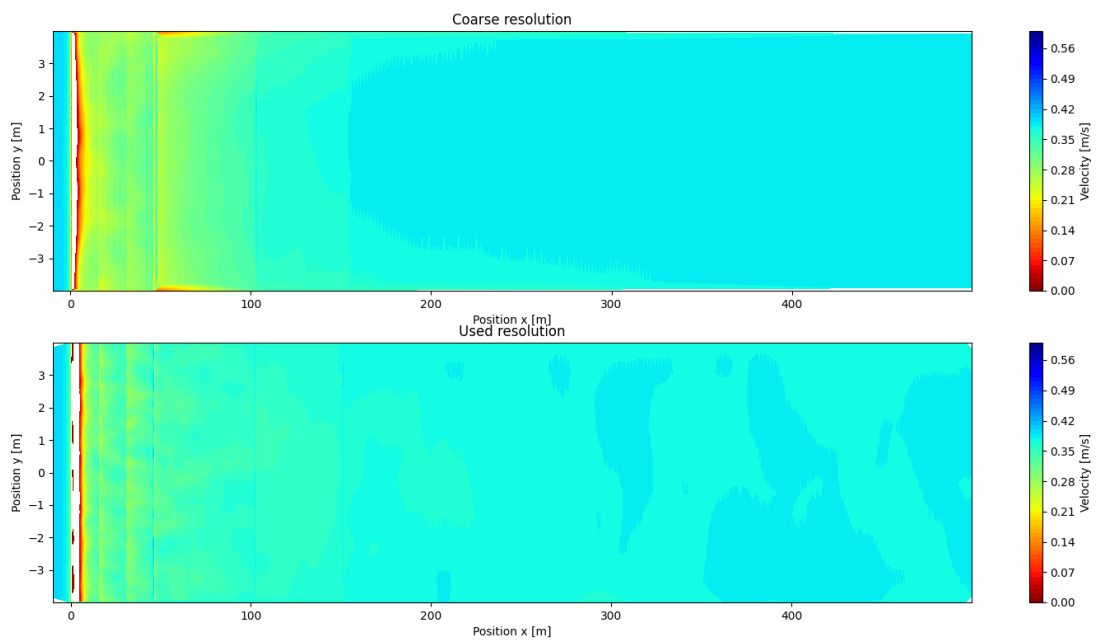


Figure 4.5: XY-plane at $z = -0.2$ m of time-averaged 2D LES simulation over the last 100 s for a coarse and middle grid resolution.

4.2 Wall function criteria & effect

To reduce the computational costs, a wall function is applied at the bottom of the solar platform array. A wall function can be applied when the turbulent scales are small enough such that they are not chaotic and predictable (isotropic behaviour). A commonly used wall function is the kqR wall function which provides a simple wrapper around the zero-gradient condition. The wall function can be used for the turbulent kinetic energy and the Reynolds stress tensor fields.

A wall function is suitable to apply when the y^+ value is in the log-layer between 20-30 and 200-300. For a case like this, it is difficult to manage this for all grid cells. A wall function is suitable when the pressure gradient hardly changes, an aspect that by flow separation is not the case and where the wall function can make an error. The choice is made to go for low Reynolds modelling which y^+ is lower than 5 for the area of interest. This is because for LES, in this case, there are no suitable wall functions available in the log-layer (high-Reynolds).

For the 3D case, the average y^+ is just below 5. At the front where flow separation occurs, it is slightly higher, meaning that the flow separation might be not correctly determined. The area of interest where boundary layer development occurs, however, does match the criteria. The results are illustrated in Figure 4.6 (buffer layer) for one time instance with LES, knowing that RANS gives in average y^+ of more than 3 times higher than LES and the main focus is on the LES results.

The presence of y^+ values in the buffer layer (Figure 4.6) and logarithmic layer (log-law layer) are minimal, making the choice of using low Reynolds modelling ($y^+ < 5$) suitable for the used grid resolution.

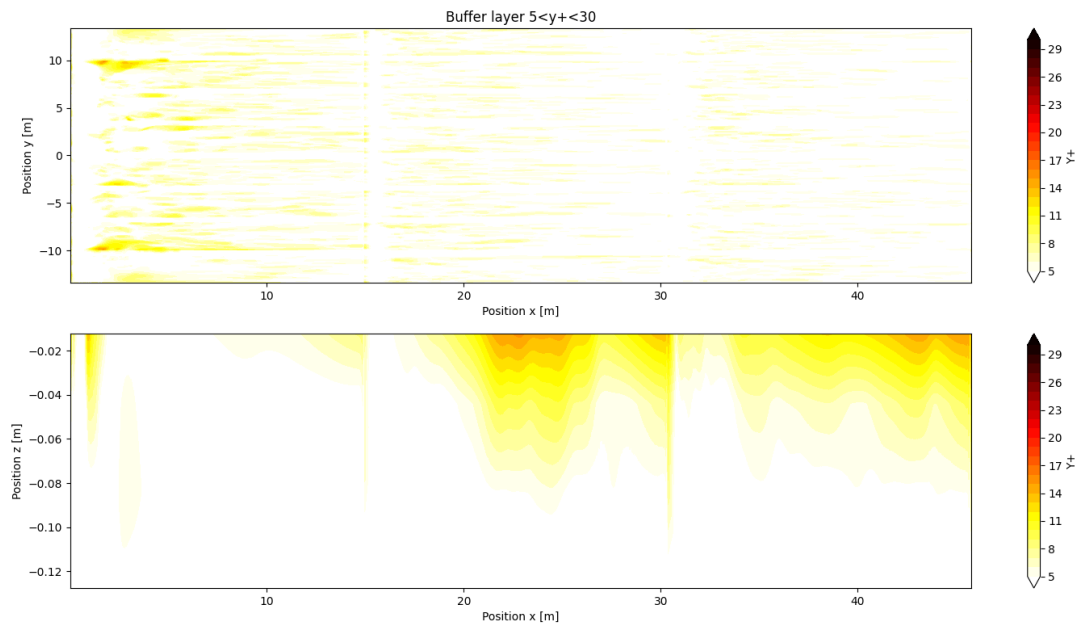


Figure 4.6: The y^+ value for the bottom view and side view of the solar platform array in the buffer layer. The XZ-plane is in the gaps of the array. The LES results are not averaged over time.

For a low y^+ value in the viscous sublayer, the wall-function effect should be rather small. However, the orientation could affect the y^+ value due to flow amplification. The y^+ criterion based on the LES results are given in Table 4.1. The values are a range because LES is time dependent; average remains similar.

Table 4.1: Wall criteria based on 3D LES results for different orientations.

Orientation [degree]	y^+ min	y^+ max	y^+ avg
0.0	0.2	24-39	4.7
22.5	0.3-0.4	22-26	5.0
45.0	0.2-0.3	22-25	5.5
67.5	0.2-0.3	25-30	4.8
90.0	0.2	24-34	4.2

The difference between applying the high Reynolds wall function or the low Reynolds wall functions on the velocity probes beneath the array and the wake is shown in Figure 4.7 and Figure 4.9 (low-Reynolds wall functions), Figure 4.8 and Figure 4.10 (high-Reynolds wall functions) for the 3D LES case with 67.5° orientation for one time instance.

The effect of the wall functions is only visible near the plate between $z = -0.5$ and 0.0 m. Applying the high Reynolds wall functions resulted in a thicker boundary layer at $x = 44.3$ m. This could be interpreted as over predictive, resulting in a longer wake. The outcome of the report is not influenced because the global shape of the wake remains the same.

A test was carried out to compare the rough high-Reynolds wall functions, which account for marine growth of 50 mm, with the low-Reynolds wall functions. The test was performed for the 2D case. The difference in grid resolution is that the prism layers are not used for the rough high-Reynolds wall function, as explained in Section 3.3.1, to comply with a cell size in a similar order as the roughness. However, note that this resulted in a y^+ value up to 1200 which is outside the log-layer ($y^+ < 300$) where the high-Reynolds wall function is applicable. The comparison is made for the 2D case.

During the wake length assessment described in Section 6.4, it was found that the rough high-Reynolds wall function resulted in a wake length of 18-22L (results in Appendix A.1.5), while the low-Reynolds wall function resulted in a wake length of around 24L. The boundary layer thickness, measurement for the wake depth, is larger beneath the array using rough high-Reynolds wall function, but reaches a similar wake depth in the extent. Despite the uncertainties that may arise from using different grid resolutions and the application of wall functions that can affect flow separation, the low-Reynolds wall function with a grid using prism layers is used in the remainder to be conservative in the wake size.

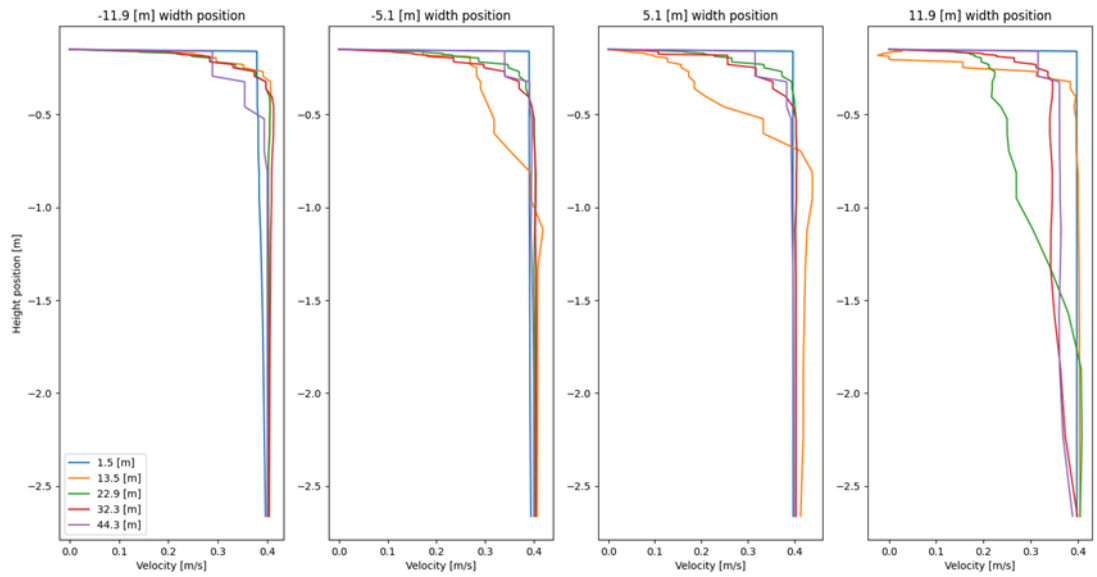


Figure 4.7: Low-Reynolds wall functions – probe locations beneath the array showing the velocity profile over depth.

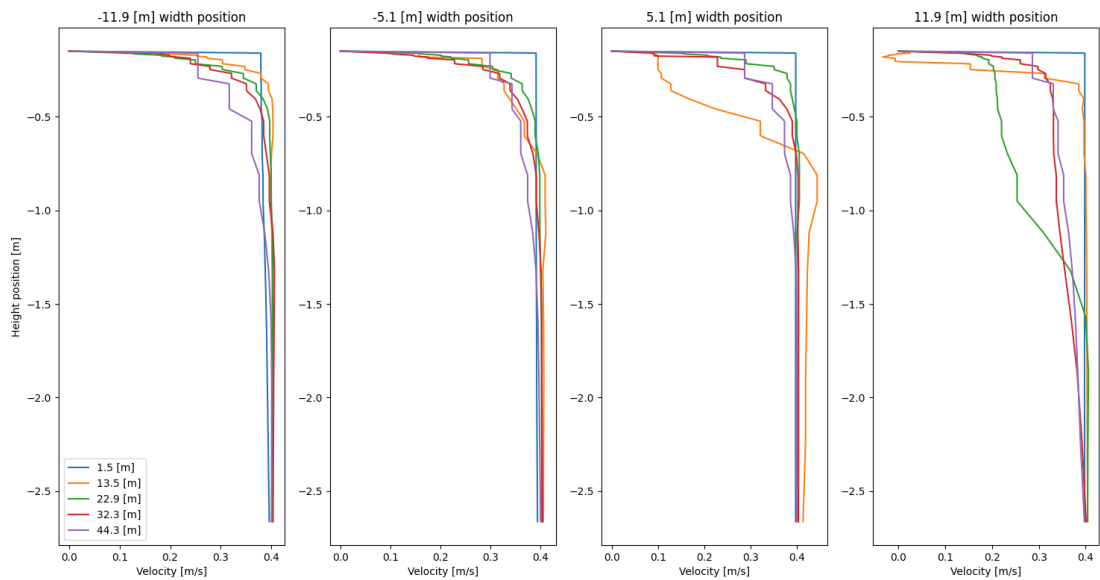


Figure 4.8: High-Reynolds wall functions – probe locations beneath the array showing the velocity profile over depth.

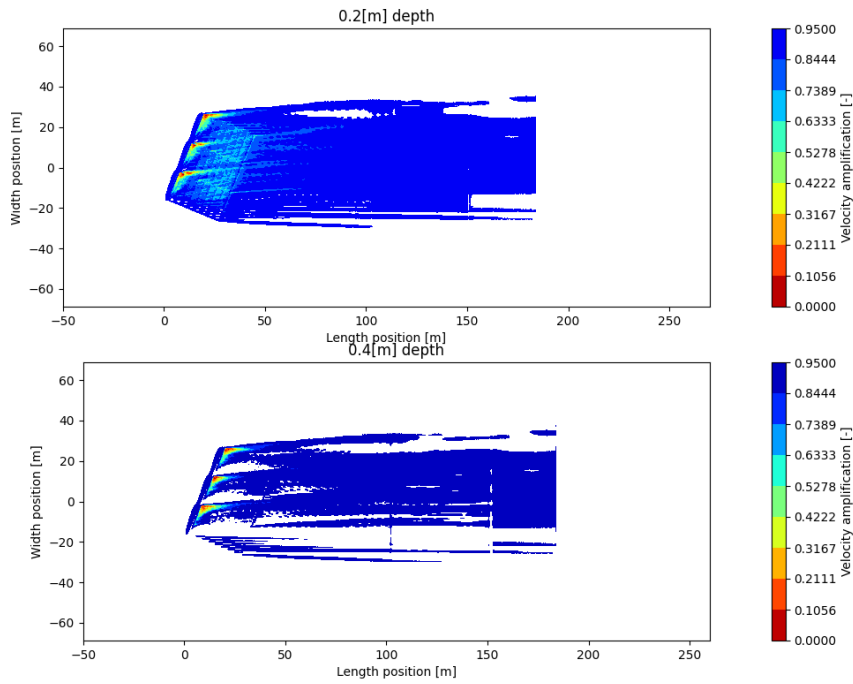


Figure 4.9: Low-Reynolds wall functions – XY-contour planes at -0.2 m and -0.4 m showing the wake shape with exponential fit (black) after averaging over the last 100 s.

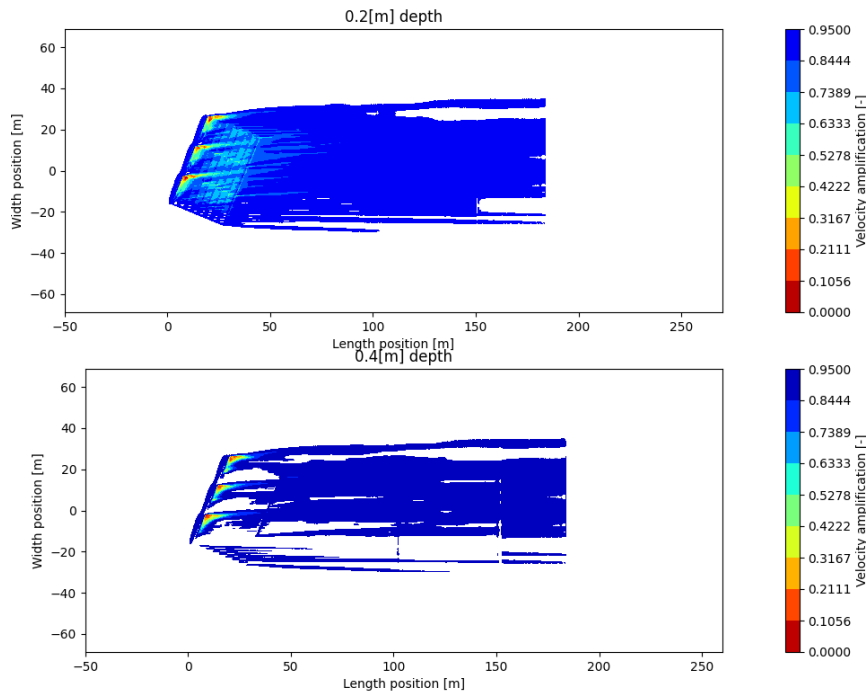


Figure 4.10: High-Reynolds wall functions – XY-contour planes at -0.2 m and -0.4 m showing the wake shape with exponential fit (black) after averaging over the last 100 s.

4.3 Coverage turbulent kinetic energy

A rule of thumb is that LES needs to cover at least 80% of the (large) turbulent eddies, because the small-scale eddies have an isotropic behaviour and, therefore, are easier to be modelled. Before performing any LES simulations, to reduce computational costs, RANS simulations already can give a good indication whether the applied grid is sufficiently fine enough for LES. The RANS simulation in this section is performed for an array with orientation 67.5° after 750 s. The following formula is applied for the RANS simulation:

$$f = \frac{l_0}{\Delta^{\frac{1}{3}}} = \frac{\nu_t}{C_\mu \sqrt{k}} > 5,$$

Where C_μ is a constant with a value of 0.09, k and ν_t the turbulent kinetic energy and eddy viscosity, and Δ the grid volume. This equation indicates whether a LES simulations would be able to solve at least 80% of the turbulent eddies.

The result for f is shown in the top plots of in Figure 4.11, Figure 4.12, and Figure 4.13 for different cross sections. The value for f is above 5 almost everywhere. However, at the front of the array it is lower which could indicate that flow separation is not correctly modelled. Based on the top plots we concluded that the grid was sufficient to test for LES and look if 80% is resolved.

After performing the LES simulation of this case, the lower subplots in Figure 4.11, Figure 4.12, and Figure 4.13 are made. The ratio of resolved turbulent kinetic energy over the total turbulent kinetic energy (resolved plus modelled) is illustrated. Especially for $x < 100$ m, the eddies seem to be resolved for 80%. However, for $x > 150$ m the resolved turbulence becomes in average lower than 80% and is less trustworthy.

We conclude that the grid is sufficient, weighing against computational costs, for modelling the boundary layer development, the area of interest, but not for detecting the flow separation. Grid refinement is not suitable (requires at least 40 million cells) because of the high computational costs. Wall functions cannot cover this as these are not suitable for flow separation. The less-resolved turbulence for $x > 150$ m needs to be accounted for in further analyses because at this distance mixture can be underestimated.

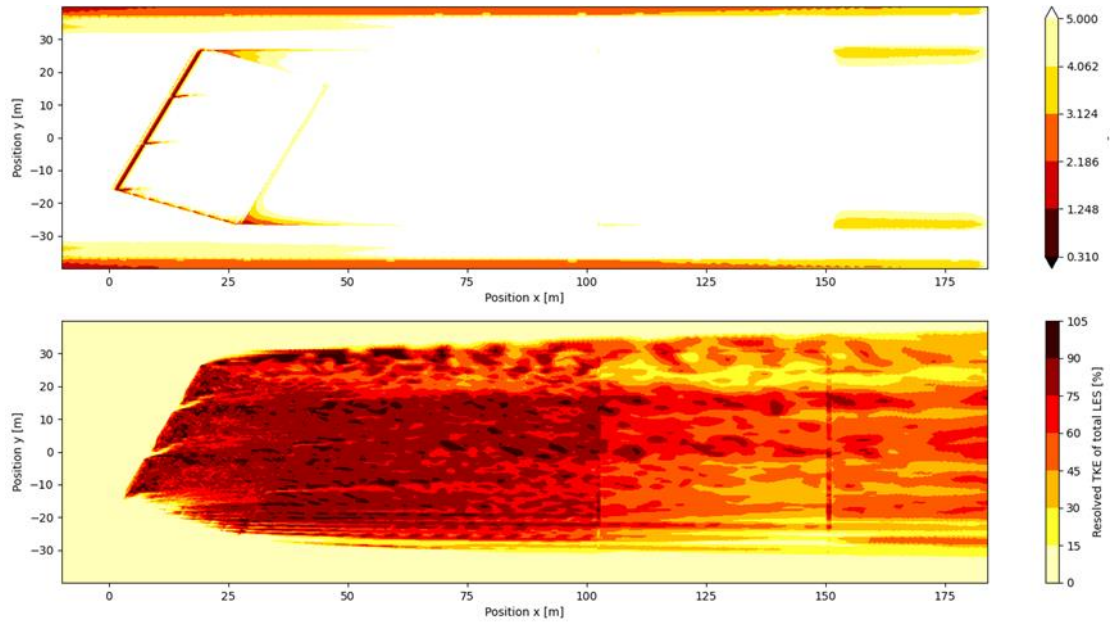


Figure 4.11: XY-contour planes at -0.2 m showing the criteria for 'f' (top figure) and the percentage of resolved turbulent eddy scales (bottom figure).

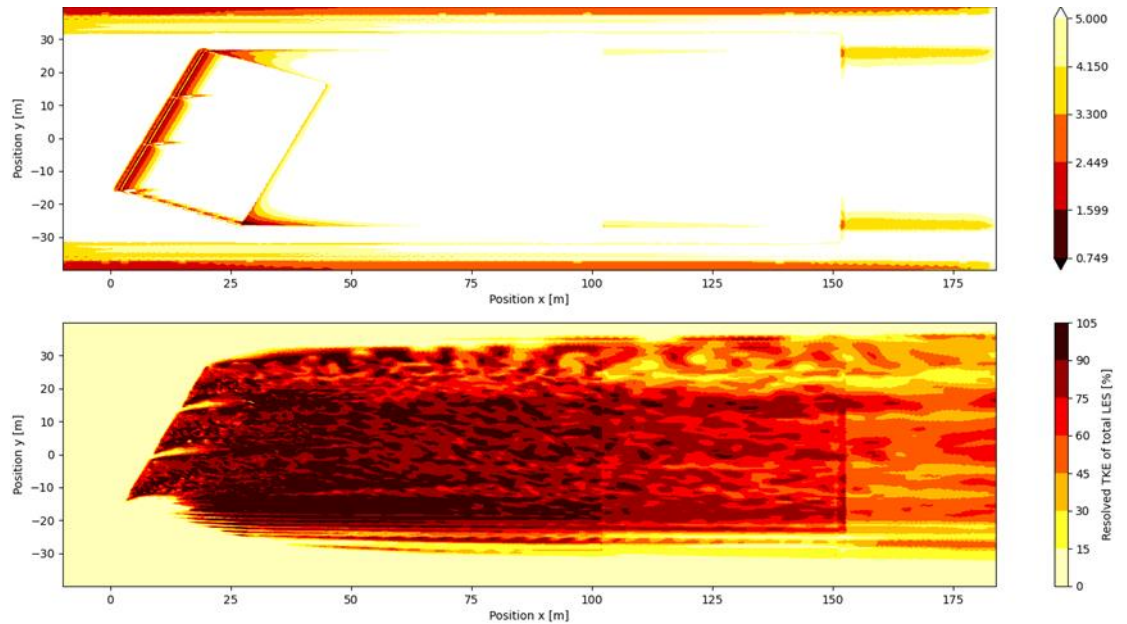


Figure 4.12: XY-contour planes at -0.4 m showing the criteria for 'f' (top figure) and the percentage of resolved turbulent eddy scales (bottom figure).

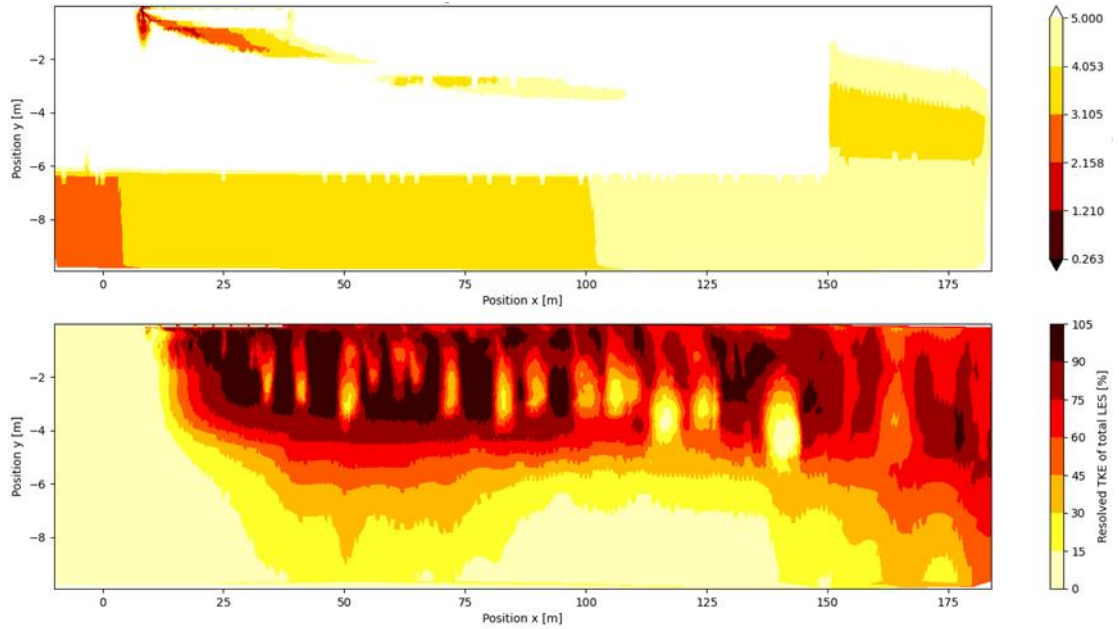


Figure 4.13: XZ-contour planes showing the criteria for ‘ f ’ (top figure) and the percentage of resolved turbulent eddy scales (bottom figure).

4.4 Time coverage 3D-LES

Another assessment that needs to be performed is the “convergence” of the LES in time. The LES-simulations are performed for another 750 s, using the RANS results as initial condition. However, flow features modelled using LES need time to develop. The initialization with RANS results in a transition to LES that needs to be propagated out of the domain. A time range needs to be defined where the LES results are consistent. The time development of the velocity probes over 50 s increments is shown in Figure 4.14. The criteria is that the maximum change is below 1%. This is the case for the last 100 s (1400 to 1500 s). With a current of 0.4 m/s, the transition from LES to RANS getting out of the domain takes up to 500 s (up to simulation time 1250 s).

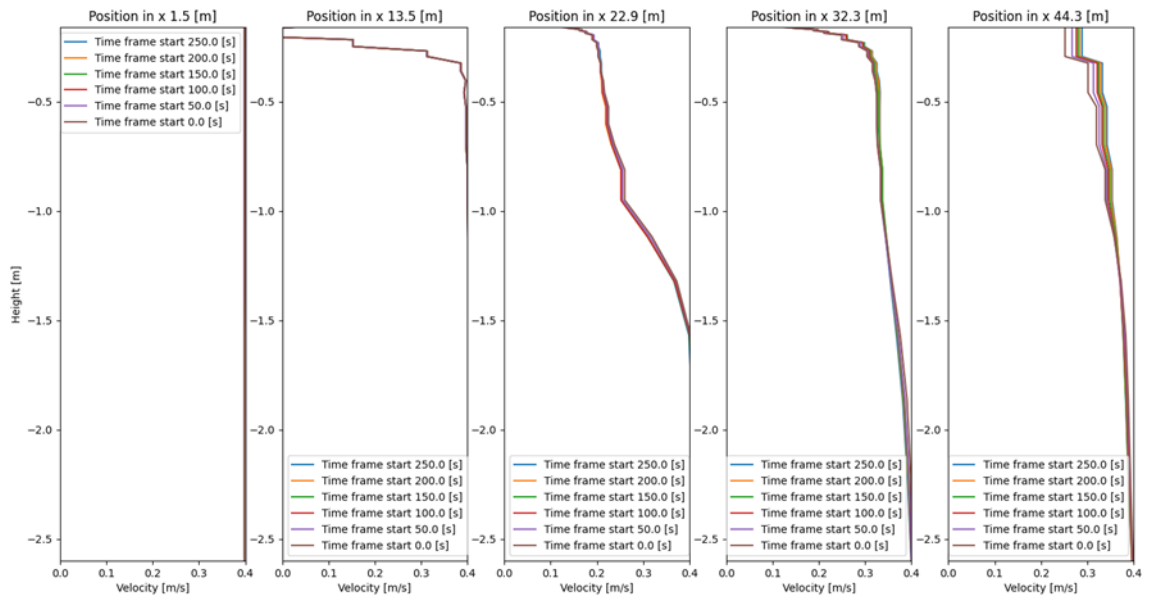


Figure 4.14: Example velocity probes with LES signal averaged per 50 s. The example is for location at 11.9 m width of the array for 67.5° orientation.

5 Analysis of 3D simulations

The 3D simulations are discussed in this section. When analysing the results, we focus on the following aspects, noting that all results depend on array orientation (Section 3.2):

- The effects of gaps between the individual platforms on the vertical velocity profile beneath the array for one orientation of the solar platform array
- Forces and moments acting upon the array
- Wake spreading, for which we derive a simple relation between distance downstream of the array and wake width
- Wake depth
- Effect of different tidal current amplitudes on forces acting on the array and wake dimensions

5.1 The effect of gaps between the individual platforms

The effect of gaps on the vertical profile beneath the array is studied in two steps:

1. The difference between a mesh with and without gaps between the platforms is studied using RANS simulations. Even though RANS might not result in the correct wake, it can indicate if the gaps between the solar platforms are influencing the results.
2. The RANS simulations with gaps are then compared to LES simulations. If these are coherent, we assume that the LES simulations behave in a similar way as the RANS simulations.

5.1.1 RANS results

The RANS simulations run for a period of 750 s. We compare simulations with and without gaps for an array orientation of 0° . Velocity profiles at the longitudinal end of the array ($x = 44.3$ m) are shown in Figure 5.1. At all width positions we observe a very similar velocity profile, with a boundary layer of up to 2 m high. The simulations with and without gaps show a negligible difference. However, the RANS results turn out to be quite different from the LES results. . This is explained in the following subsection.

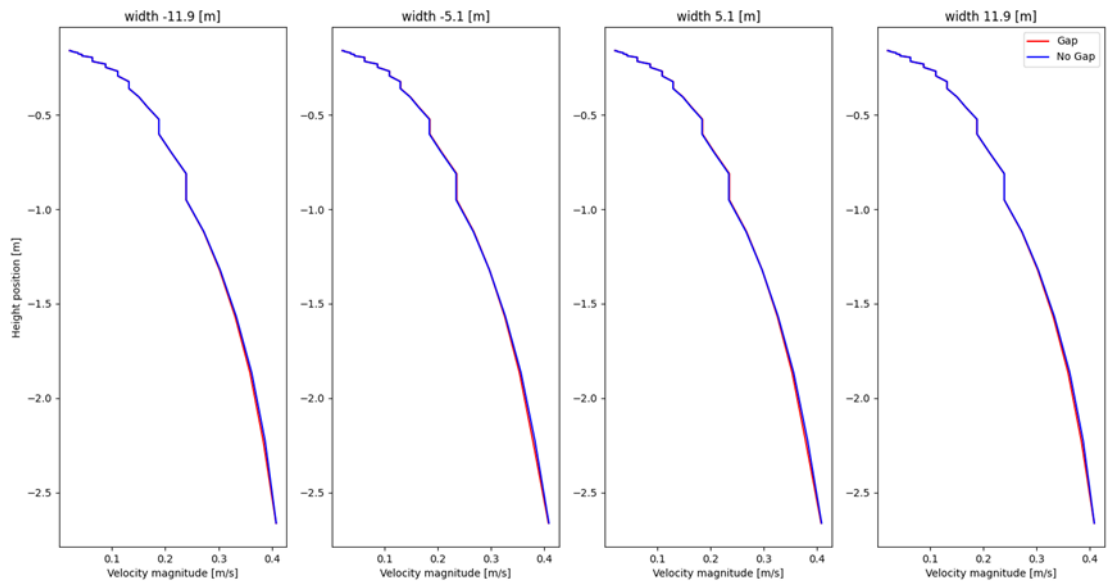


Figure 5.1: Velocity profile in the upper part of the water column beneath array, comparing between gaps (red) and without gaps (blue) using RANS at length position $x = 44.3$ m.

5.1.2 LES results

The next step is to compare the RANS simulations with gaps to the LES simulations with gaps. For the LES results, we average the velocity profiles over the last 100 simulated seconds. These averaged profiles are compared to the RANS results in Figure 5.2, both for a 0° array orientation. The difference with Figure 5.1 is that we now compare velocity profiles for different longitudinal positions at a width position of $y = 5.1$ m.

A large difference is visible between the two methods. RANS seems to significantly overestimate the boundary layer thickness and the wake depth. Near the gaps, flow velocity is substantially lower for the RANS simulations. Additionally, the RANS equations do not fully capture the time-dependent flow features such as shedding, which could impact the flow near gaps. The velocity profile of LES changes from position 22.9 m to 32.3 m, where a gap is present (refer to Figure 3.6), indicating that the turbulent flow is affected by the gap.

In the following sections, both 3D and 2D results demonstrate that time-dependent flow features appear at the gaps. The gaps will be considered in the remaining parts of the analysis.

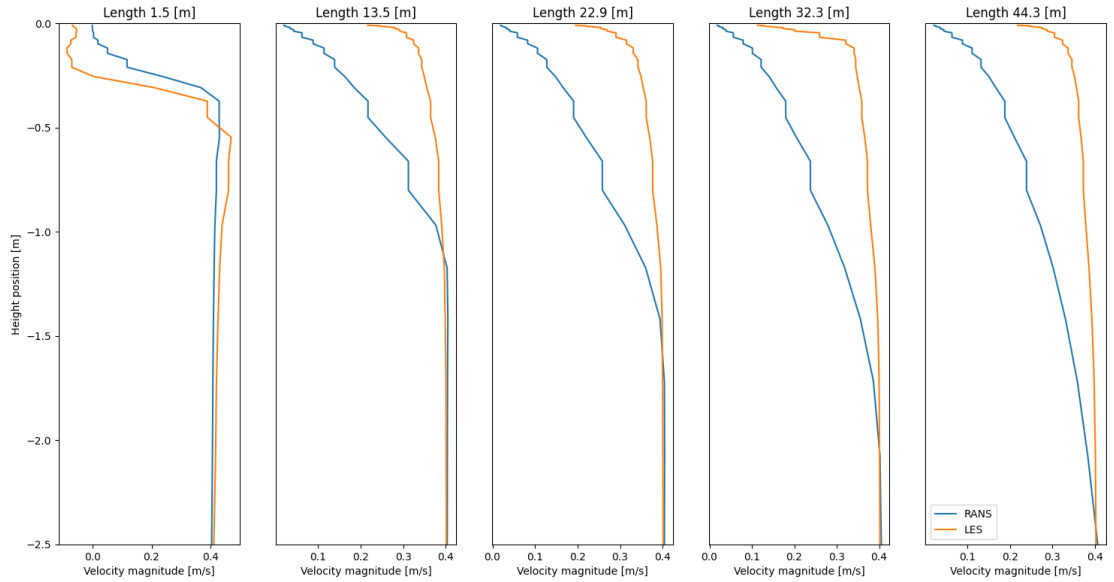


Figure 5.2: Comparison velocity probes beneath array for LES and RANS with 0° orientation at width position -5.1 m and length position as given in the title of the plot.

5.2 Forces & moments

We consider three types of forcing exerted on the array by the flow, i.e., the normal (pressure) force (F_p), the tangential (viscous) force (F_v) and the rotational moment (M). The pressure force is found by integrating the simulated pressure over the total array. The viscous force is found by multiplying the (deviatoric) stress tensor with the dynamic viscosity and the face area vector integrated over the total array. The rotational moment is found by multiplying every force contribution (pressure and viscous) per neighbouring grid cell with the distance to the centre of gravity of the array and sum over these cells. The centre of gravity is located at coordinate $(0.5L, 0, 0)$.

The forces are averaged over the last 100 s of the LES simulations and calculate for each direction of the global x, y, and z direction (see Figure 5.3). From these forces and rotational moment we define force and moment coefficients, by applying the following formulas:

$$C_p = \frac{F_p}{\frac{1}{2}\rho U^2 A_{front}} \quad (\text{pressure coefficient}),$$

$$C_v = \frac{F_v}{\frac{1}{2}\rho U^2 A_{tang}} \quad (\text{viscous coefficient}),$$

$$C_m = \frac{M}{\frac{1}{2}\rho U^2 A_{cord} l} \quad (\text{moment coefficient}).$$

Note the difference in definition of the reference area (A), which depends on the effective area where the force is acting on. The pressure force (F_p) is acting in any case perpendicular to the array while the viscous force (F_v) is acting in tangential direction. The ambient velocity U and water density ρ are needed to calculate the coefficients. The moment is defined by M . Note that each area depends on the array orientation and can be calculated using Table 5.1 and Figure 5.3:

- A_{front} is the frontal area where the pressure is acting on. As we neglect the frontal area of the intermediate gap, this is defined as: $A_{front} = W_y \cdot D$ where $W_y = W = 26.9$ m and $D = 0.15$ m for in x-direction with 0° orientation and $W_y = L = 45.8$ m for 90° orientation.
- A_{tang} is the area tangential to the acting force; for x-direction 0° , A_{tang} is the bottom $L_x \cdot W_y$.
- A_{cord} is the projected area on the defined axis. For 0° orientation and around the y-axis this is $L_x \cdot D$. The parameter l is the largest length size in the axis direction. For the x-direction, $l_x = L_x$.

The term W_y is the projected (perpendicular) width with respect to the coordinate axis and the term L_x the projected length. The terms are illustrated in Figure 5.3. The ratio of the projected sizes are given in Table 5.1.

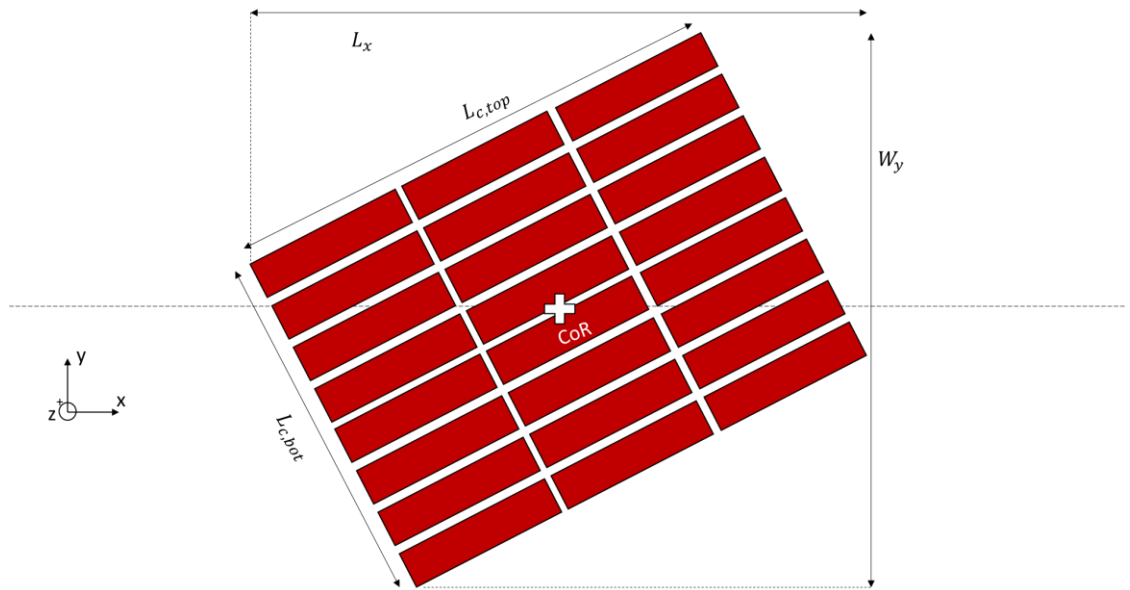


Figure 5.3: Explanation terms length and width used for formulations.

Table 5.1: Projected ratios in the axle system of the ambient current.

Orientation [degree]	L_x/W_y	W_y/D	L_x/D
0.0	1.71	178.67	305.33
22.5	1.24	281.91	350.46
45.0	1.00	342.24	342.34
67.5	0.80	350.46	281.91
90.0	0.59	305.33	178.67

For a current velocity of 0.4 m/s, the computed coefficients per orientation are given in Figure 5.4. The forces acting on then array are given in Figure 5.5. A negative value means that the force acts in the negative direction of the axis. The computed coefficients are given in Table 5.2.

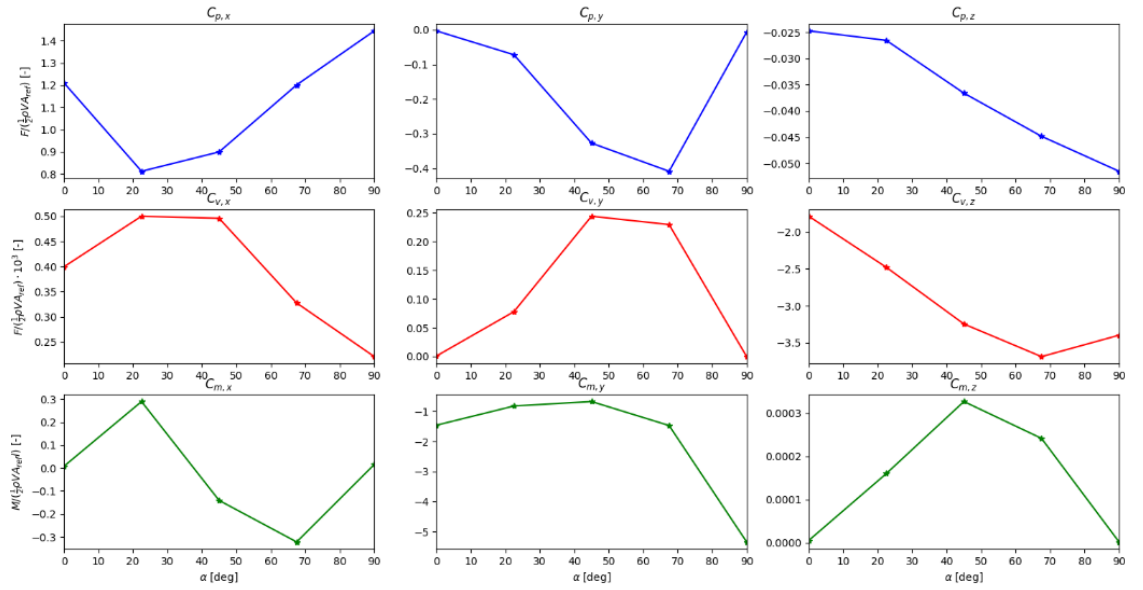


Figure 5.4: Force/moment coefficients per axis direction and orientation.

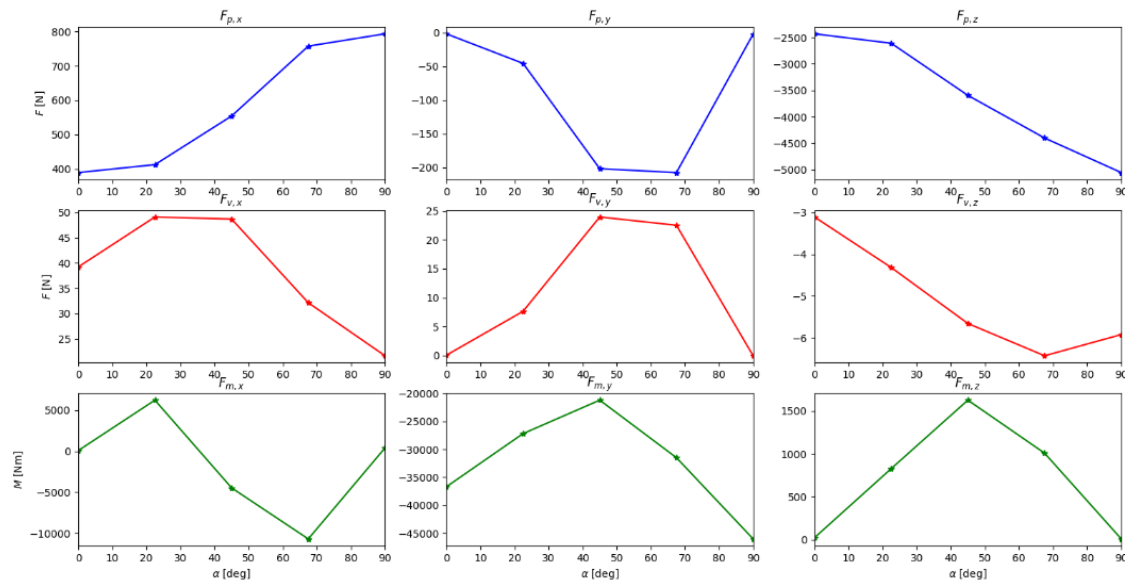


Figure 5.5: Force/moment in N per axis direction and orientation.

Table 5.2: Coefficients for force and moment per orientation with $U = 0.4$ m/s.

Orientation [degree]	x			y			z		
	C_p	$C_v \cdot 10^3$	C_m	C_p	$C_v \cdot 10^3$	C_m	C_p	$C_v \cdot 10^3$	C_m
0.0	1.21	0.40	0.00	0.00	0.00	-1.46	-0.02	-1.78	0.0
22.5	0.81	0.50	0.29	-0.07	0.08	-0.82	-0.03	-2.48	0.0
45.0	0.90	0.50	-0.14	-0.33	0.24	-0.67	-0.04	-3.25	0.0
67.5	1.20	0.33	-0.32	-0.41	0.23	-1.47	-0.04	-3.69	0.0
90.0	1.44	0.22	0.00	0.00	0.00	-5.34	-0.05	-3.40	0.0

Based on this analysis, we can conclude the following:

- The pressure forces are larger than the viscous effects.
- A lower value of L_x/W_y results in an increase of the pressure coefficient.
- The yawing moment according to the axis system is small compared to the pitching and rolling moment. The rolling moment becomes more important for smaller L_x/W_y .
- The forces on the array depend on the aspect ratio and orientation (asymmetry) of the array. For instance, the 67.5 degrees orientation has larger coefficients for the given dimensions in this case, while 90 degrees experiences the largest forces.
- An oriented array results in a reduction of the pressure coefficient, but the frontal area increases, resulting in a total force that increases.
- An oriented array generates a non-negligible sideward force. The total force is also large due to the relatively large array size. The pressure drop beneath the array causes a negative heave motion of the solar platform array.
- The presence of marine growth may be a factor due to the relatively large pressure coefficients.
- The marine growth characteristics have influence on the viscous forces. In case there is more marine growth as assumed in the CFD model the viscous forces will be higher than simulated and the opposite holds for less marine growth as simulated.

5.3 Wake spreading

To determine how wide the wake behind the array is, we need to define the wake relative to the environment. We consider that in the wake, the total turbulent kinetic energy (TKE) increases while the flow velocity decreases.

We define the wake area for both parameters and quantify them separately. When the TKE the flow velocity deviates more than 5 percent from the initial condition (when there is no array), the corresponding position is considered to be part of the wake. After defining this area, wake spreading is determined by fitting an exponential function to the outer contour of the wake area. This function depends on the projected width W_y :

$$y = a \cdot \exp(-b \cdot x) + c \cdot \frac{1}{2} W_y(\alpha)$$

An example of a fit is given in Figure 5.6. A fit is made for the “top” side ($y > 0$) and the “bottom” side ($y < 0$). Snapshots of the wake spreading for different orientations are available in Section A.2.

The values for a , b , and c need to be determined for the XY-planes and the XZ-plane. The values for $\frac{1}{2} W_y$, depending on the orientation α , are given in Table 5.3, while coefficients a , b , and c are given in in Table 5.4, Table 5.5, and Table 5.6. Each table corresponds to a different depth, of -0.2 m, -0.4 m and -0.6 m, respectively.

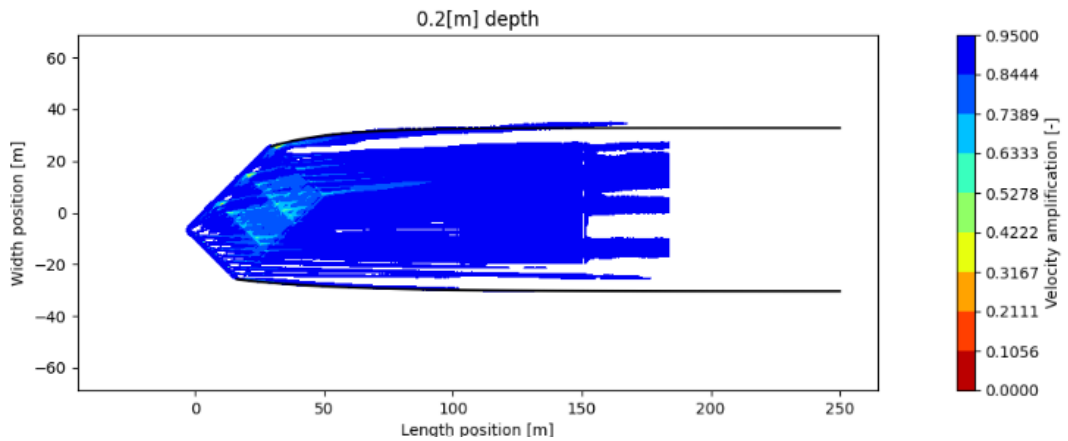


Figure 5.6: Example fit (black) wake at $z = -0.2$ m depth for orientation 45.0° .

Table 5.3: Definition of $W_y(\alpha)$ which is for both sides the same.

Orientation [degree]	$\frac{1}{2}W_y(\alpha)$
0.0	13.40
22.5	21.14
45.0	25.67
67.5	26.28
90.0	22.90

The results in the tables provide new insights. The main conclusions based on these insights follows: the wake spreading is getting marginable smaller when increasing in depth. In further analysis it is assumed that the wake spreading is constant over depth. Furthermore, the wake spreading based on the TKE contours are comparable the ones found from the velocity contours. The exponential fit tells us how the wake develops downstream of the array. A change in the orientation results in a more dominant effect of the exponential term and the offset (c) increases.

Regarding the coefficients in the fit, a and b describe the wake width directly downstream of the array (small values for x) and determine the flow separation angle. They reach their highest values when α is around 45° and approach zero when α is near 0 or 90. The value a is generally larger for the top side while b is smaller. We are not analysing these coefficients further as we are mainly interested in the offset (coefficient c).

The offset (c) describes the wake width for larger values of x , which is what we are primarily interested in. The approximation of the spreading is based on the output of the velocity and TKE amplification. This coefficient depends on whether there is an orientation and the length from the front of the array to the point of separation (L_c), see Figure 5.3: for top this is 45.8 m, and for bottom this is 26.8 m. The reason why this seems to be is that for every orientation between 0 and 90 degrees, the value for c is approaching similar values.

The offset is described using a linear fit. A boundary condition is applied for the value of c such that when the array has no length, the value of c goes to 1:

$$c = 0.0079 \cdot L_c + 1.$$

The total wake width is:

$$W_{wake,tot} = \begin{cases} (0.0079 \cdot (L_{c,top} + L_{c,bot}) + 2) \cdot \frac{1}{2} W_y(\alpha), & \text{if } 0 < \alpha < 90 \\ 1.06 \cdot W_y(\alpha), & \text{if } \alpha = 0 \text{ or } \alpha = 90 \end{cases},$$

Note that we did not analyse small orientations meaning that this equation might not be applicable for that region.

In our analysis, we do not account for possible effects of single solar platforms or gap distance. This requires further investigation, especially for different orientations using LES.

Table 5.4: XY-plane on -0.2 m – fit of wake spreading using exponential function.

Orientation [degree]	Side	a		b · 1e – 3		C	
		TKE	U	TKE	U	TKE	U
0.0	Top	-0.89	-2.84	24.37	7.16	1.08	1.18
22.5	Top	-19.32	-16.70	20.77	14.37	1.40	1.46
	Bottom	5.43	5.03	40.92	39.01	-1.21	-1.19
45.0	Top	-22.72	-18.57	33.39	24.53	1.38	1.36
	Bottom	8.11	8.37	29.48	45.13	-1.19	-1.16
67.5	Top	-9.39	-10.28	14.56	9.00	1.35	1.39
	Bottom	8.49	7.12	20.65	20.14	-1.19	-1.16
90.0	Top	-1.84	-	16.81	-	1.07	-

Table 5.5: XY-plane on -0.4 m – fit of wake spreading using exponential function.

Orientation [degree]	Side	a		b · 1e – 3		c	
		TKE	U	TKE	U	TKE	U
0.0	Top	-1.13	-	32.81	-	1.07	-
22.5	Top	-18.18	-16.60	17.58	15.04	1.42	1.44
	Bottom	5.11	5.11	39.42	46.32	-1.19	-1.17
45.0	Top	-22.59	-18.08	28.43	22.45	1.39	1.37
	Bottom	8.65	7.29	45.74	30.69	-1.16	-1.17
67.5	Top	-11.49	-12.14	17.97	6.20	1.35	1.47
	Bottom	8.29	7.06	10.06	13.22	-1.24	-1.19
90.0	Top	-2.39	-1.36	63.52	9.90	1.04	1.05

Table 5.6: XY-plane on -0.6 m – fit of wake spreading using exponential function.

Orientation [degree]	Side	a		b · 1e – 3		c	
		TKE	U	TKE	U	TKE	U
0.0	Top	-0.84	-1.18	80.46	8.61	1.03	1.09
22.5	Top	-18.47	-16.89	20.26	18.41	1.39	1.39
	Bottom	-	4.68	-	22.04	-	-1.19
45.0	Top	-18.98	-17.36	23.52	21.87	1.38	1.36
	Bottom	10.72	6.46	83.90	23.57	-1.11	-1.17

67.5	Top	-10.20	-13.54	14.34	20.75	1.35	1.31
	Bottom	6.52	6.55	25.56	14.39	-1.14	-1.17
90.0	Top	-1.30	-1.21	22.10	37.21	1.05	1.03

5.4 Wake depth

Three main flow features define the flow field around and downstream of the solar array, and their occurrence is indicated in Figure 5.7 using the red numbers. Firstly, flow separation occurs on the top and bottom sides of the array (1). Secondly, flow separation happens locally between individual solar platforms (2). And thirdly, a wake is generated due to boundary layer development beneath the array (3).

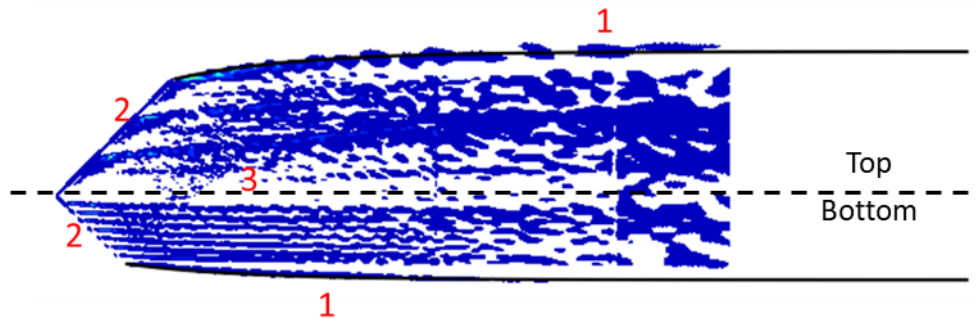


Figure 5.7: Different flow features for orientation of 45° at -0.4 m in height position.

Flow separation is a three-dimensional phenomenon and hence also leads to a vertical extension of the wake. This effect cannot be studied in 2D (Chapter 6) and thus is analysed here. These results are based on the flow field over the last 30 s of the LES simulation and then considering the deviation from the original flow field (without an array). Note that without averaging the wake can reach deeper.

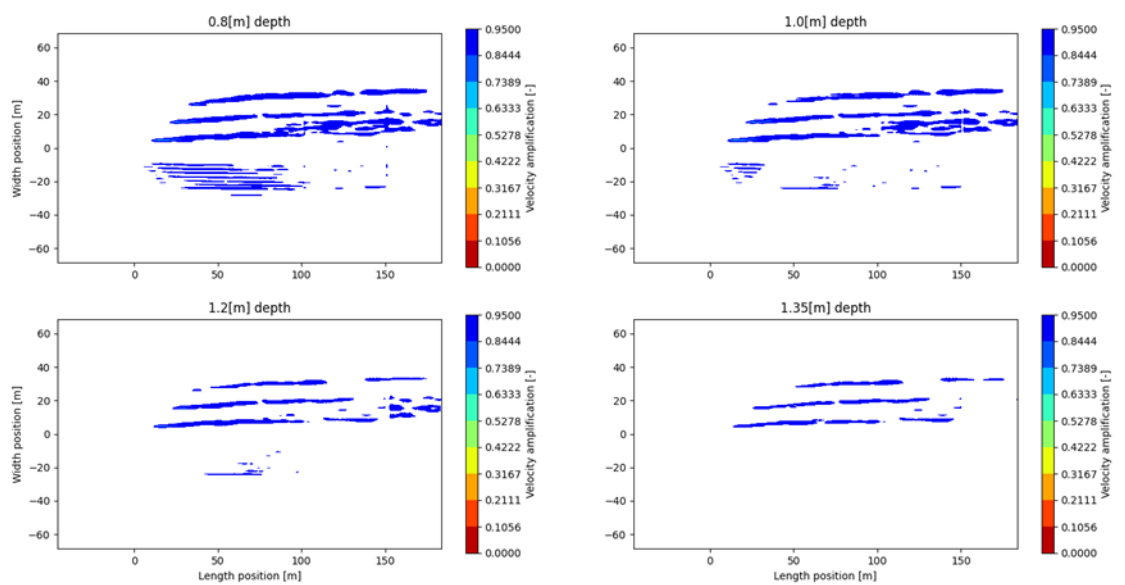
The depth to which flow separation extends is analysed using XY-planes lower than -0.6 m. An example of the contour planes at these depth levels are shown in Figure 5.8 for an orientation of 45°. The penetration depth is then determined by assessing whether there are substantial effects on the flow velocity field, which leads to the depths shown in Table 5.7. The penetration depth is defined separately both for the top and bottom sides of the array, for each rotation.

The results indicate that not only the total array affects the penetration depth, but also the solar platforms on an individual level. When the array is oriented (mostly) parallel to the flow, penetration depth varies from 1.2 to 2.5 m. When the array orientation increases, this results in a larger penetration depth, which may be larger than 3.0 m, for an orientation of 67.5°. For this orientation, we notice a large difference between the top and bottom of the array. This is related to the alignment of the corresponding side of the array with the current direction. The aspect ratio of the array and its orientation influence the (global) wake depth.

The gaps between the individual platforms seem to locally affect the wake depth. Although the analysis of flow separation for the single platforms is not sufficient based on grid requirements (see Section 4), the gaps and their orientation with respect to the flow direction do show to have an influence on the depth penetration.

Table 5.7: Minimum depth penetration flow separation effects. The (x) indicates until where substantial effects are found for 95% percentile on the velocity field.

Depth m	0.0 degree		22.5 degree		45.0 degree		67.5 degree		90.0 degree	
	Top	Bottom	Top	Bottom	Top	Bottom	Top	Bottom	Top	Bottom
0.80- 1.00								X		
1.20- 1.35			X			X				
2.00- 2.50	X	X		X						
2.50- 3.00					X				X	X
3.00>							X			



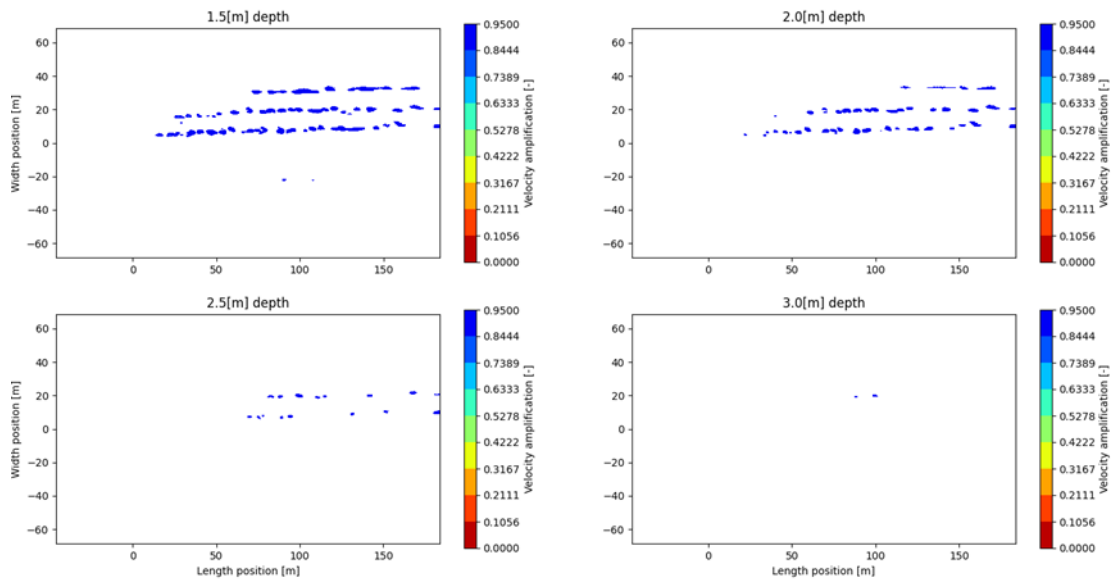


Figure 5.8: XY planes for different depth levels showing the created wake illustrated using velocity changes (95% percentile). The array is rotated 45 degrees and the results are averaged over 30 s.

5.5 The effect of current amplitude

Previous simulations were conducted with an ambient current of 0.4 m/s, but in this subsection, we will analyse the impact of increasing the ambient current is increased to 0.8 m/s using the same grid resolution as for the 0.4 m/s case.

We do need to consider that increasing the current while using the same grid resolution may affect the modelled results. Unfortunately, adapting the mesh requires time and this was not possible. This may have two possible negative impacts. First, it may result in less turbulent scales that are resolved, potentially leading to more dissipative results. Second, it may lead to errors in solving the boundary layer. The LES results for a current of 0.8 m/s showed that the average y^+ becomes around 12 at the bottom of the array which is in the buffer layer. In this area, applying wall functions may lead to erroneous predictions. Hence, the results for this current need to be analysed with care and are less trustworthy than the more extensively validated 0.4 m/s case. A more extensive analysis would be needed to understand further effects but this is out of scope for this report.

We use the same procedure for analysing the results as in the previous cases, and the analysis is limited to an orientation of 67.5° due to the high computational costs.

The increased current amplitude has little impact on the pressure and moment coefficients (Table 5.8). However, the viscous coefficients are notably different. This difference may be due to the variation in the y^+ criteria, which is crucial for the shear forces. It is possible that this difference is also dependent on the Reynolds number. The y^+ for the 0.8 m/s case is, on average, in the buffer layer, which typically leads to an error in the coefficient estimation. Correctly estimating the viscous coefficient requires a y^+ smaller than one (Eça L., 2018), leading to high computational costs. The results do indicate the order of magnitude.

Table 5.8: Effect of current amplitude on force and moment coefficients.

Orientation [degree]	x			y			z		
	C_p	$C_v \cdot 10^3$	C_m	C_p	$C_v \cdot 10^3$	C_m	C_p	$C_v \cdot 10^3$	C_m
67.5 (0.4 m/s)	1.20	0.33	-0.32	-0.41	0.23	-1.47	-0.04	-3.69	0.0
67.5 (0.8 m/s)	1.21	0.21	-0.32	-0.41	0.16	-1.46	-0.04	-2.75	0.0

Table 5.9 and Table 5.10 suggest that the change in tidal current amplitude affects wake spreading. In both cases, it was observed that the wake spreading decreased with depth. The curve of the wake, which decreases exponentially, was found to be similar on the bottom side for both currents. However, an increase in current resulted in an increase in the exponential decay of the fit on the top side, as observed using the TKE contours. On the other hand, the top side fit using the velocity contours was less affected.

The average total wake spreading in horizontal direction seems to decrease when the current increases, but requires additional research. The terms a and b , less relevant for the total wake extent, are even more affected. Especially for the top side the values can change significantly.

Table 5.9: Current of 0.4 m/s – fit of wake spreading using exponential function for an orientation of 67.5 deg.

Height [m]	Side	a		b · 1e – 3		c	
		TKE	U	TKE	U	TKE	U
-0.2	Top	-9.39	-10.28	14.56	9.00	1.35	1.39
	Bottom	8.49	7.12	20.65	20.14	-1.19	-1.16
-0.4	Top	-11.49	-12.14	17.97	6.20	1.35	1.47
	Bottom	8.29	7.06	10.06	13.22	-1.24	-1.19
-0.6	Top	-10.20	-13.54	14.34	20.75	1.35	1.31
	Bottom	6.52	6.55	25.56	14.39	-1.14	-1.17

Table 5.10: Current of 0.8 m/s – fit of wake spreading using exponential function for an orientation of 67.5 deg.

Height [m]	Side	a		b · 1e – 3		c	
		TKE	U	TKE	U	TKE	U
-0.2	Top	-19.01	-11.00	59.42	36.13	1.23	1.21
	Bottom	8.07	7.43	22.43	24.93	-1.17	-1.15
-0.4	Top	-17.01	-9.12	53.30	22.37	1.23	1.24
	Bottom	8.14	7.51	28.28	21.17	-1.14	-1.16
-0.6	Top	-17.12	-10.07	54.61	29.17	1.22	1.22
	Bottom	6.28	7.25	27.99	12.94	-1.11	-1.19

The wake depth for 0.8 m/s is illustrated in Figure 5.9 and can be compared with Section A.1.1 and the results in Table 5.7. The current seems to have little effect on the depth of the wake produced by 3D effects.

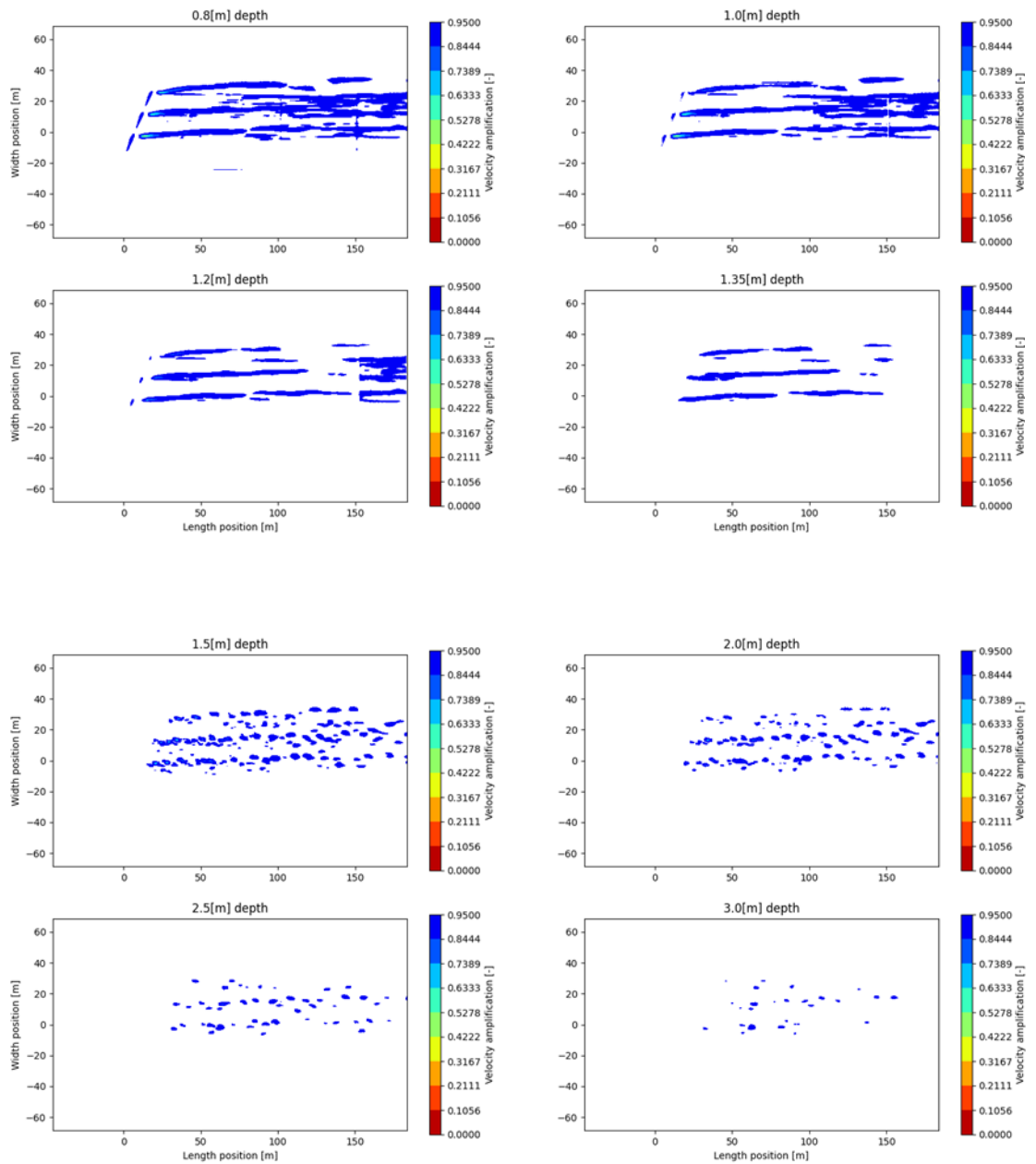


Figure 5.9: XY planes and 0.8 m/s for different depth levels showing the created wake illustrated using velocity changes (95% percentile). The array is rotated 67.5 degrees.

6 Analysis of 2D simulations

Several features, such as wake length, cannot be studied using 3D simulations due to computational restraints. Therefore, we developed a 2D LES model. The results of these 2D simulations are presented in this section.

The 2D simulations are compared with the 3D simulations for identifying three-dimensional flow effects and the ratio between 2D and 3D forces. Furthermore, the simulations are used to determine wake length and depth caused by the boundary layer generation. For this, we study both the impact of the array length and two tidal current amplitudes. Additionally, we determine the frequency of vortices shedding from the array.

It is important to note that the 2D simulations are not purely two-dimensional as LES requires a third dimension. This third dimension is 11 meters with equal spacing.

6.1 Comparison 2D vs 3D results

Before conducting any other analyses, we need to verify if the 2D simulations are accurate and consistent with the 3D simulations. Therefore, it is necessary that the 2D results are consistent with the cross-section of the 3D results. Furthermore, the 2D simulations must be reliable for the entire wake length. Similar to the 3D simulations, the 2D LES results are time-averaged over the last 100 seconds of the simulation.

We understand that 3D effects occur when the array is oriented, as explained in Chapter 5. This ultimately means that we can only compare the 2D results in this section to the 3D array with a 0° rotation.

The comparison of 2D and 3D is shown in Figure 6.1 (velocity) and Figure 6.2 (turbulent kinetic energy). The results show similar behaviour for 2D and 3D when looking to the penetration of the wake depth over the length. The bottom plot shows the actual difference between 2D and 3D, remaining at least below 8% in the wake extent for the velocity amplification.

Any small differences can be caused by e.g. the limited size in the third dimension of the 2D results and the flow separation that can occur in 3D at the corners of the individual solar platforms and the total array. Figure 6.1 and Figure 6.2 show a good match in the end of the domain despite the 3D effects, indicating that these effects may diffuse earlier.

The local differences between 2D and 3D are also visible in Figure 6.3 where we see that 3D has a larger boundary layer thickness, meaning that in 2D the turbulence is underestimated (in the order of 10%). In 3D the velocity profile changes slightly over the width, having a smaller boundary layer thickness at the sides. This difference is several percents. The difference between 3D and 2D can lead to the slightly larger extent of the 3D wake in Figure 6.1 at the end of the domain.

The presented results show that the 2D results are capable to say something about the wake length and depth magnitude but we do expect a smaller wake in 2D due to less mixing.

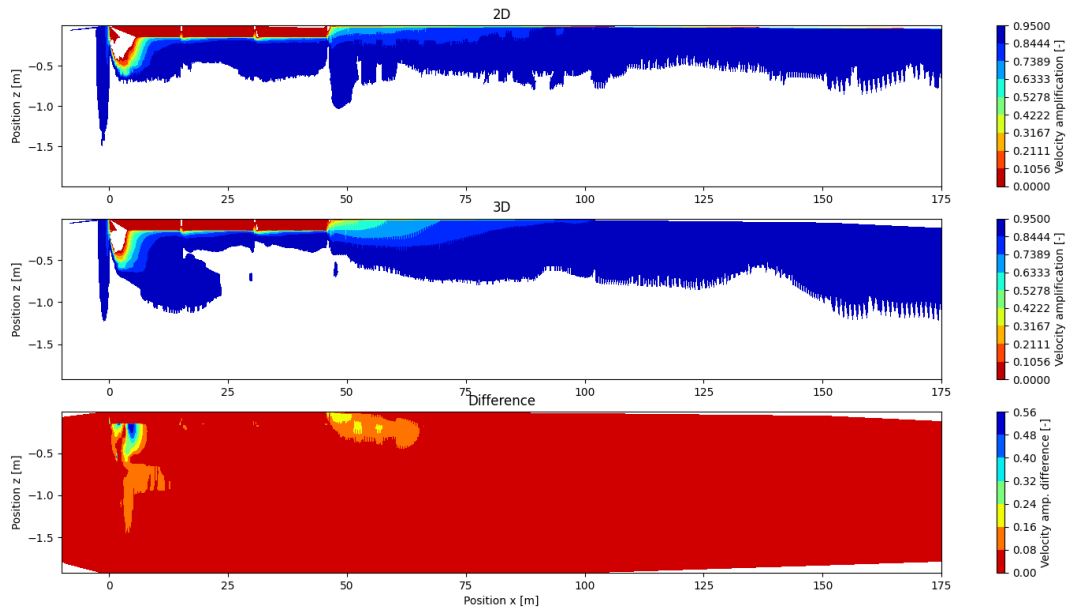


Figure 6.1: Velocity amplification in ambient flow direction difference of at least 5% between 2D (at the middle) and 3D (at $y=5.1$ m).

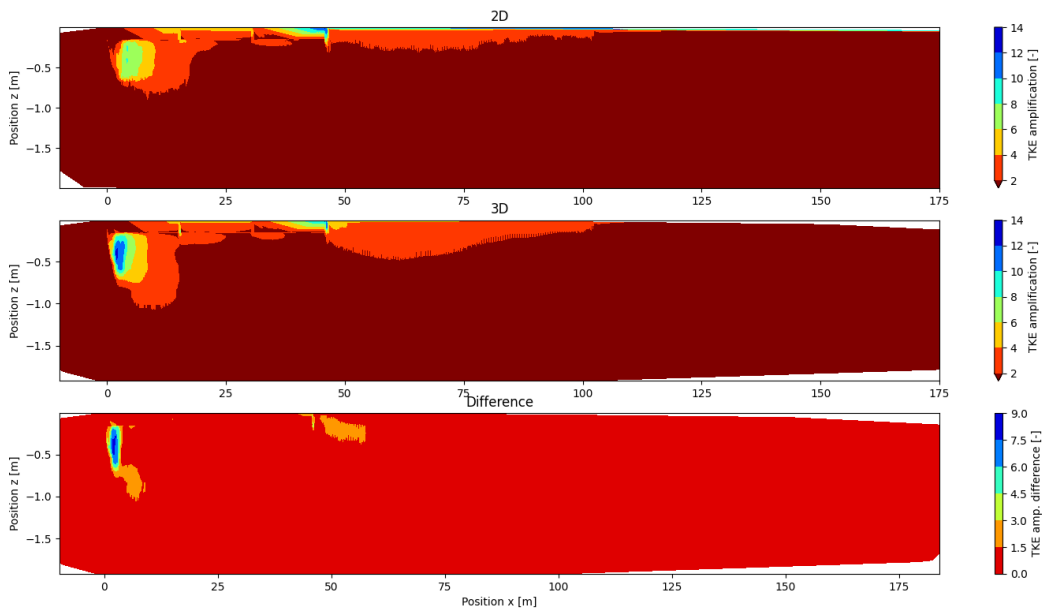


Figure 6.2: Turbulent kinetic energy difference between 2D (at the middle) and 3D (at $y=5.1$ m).

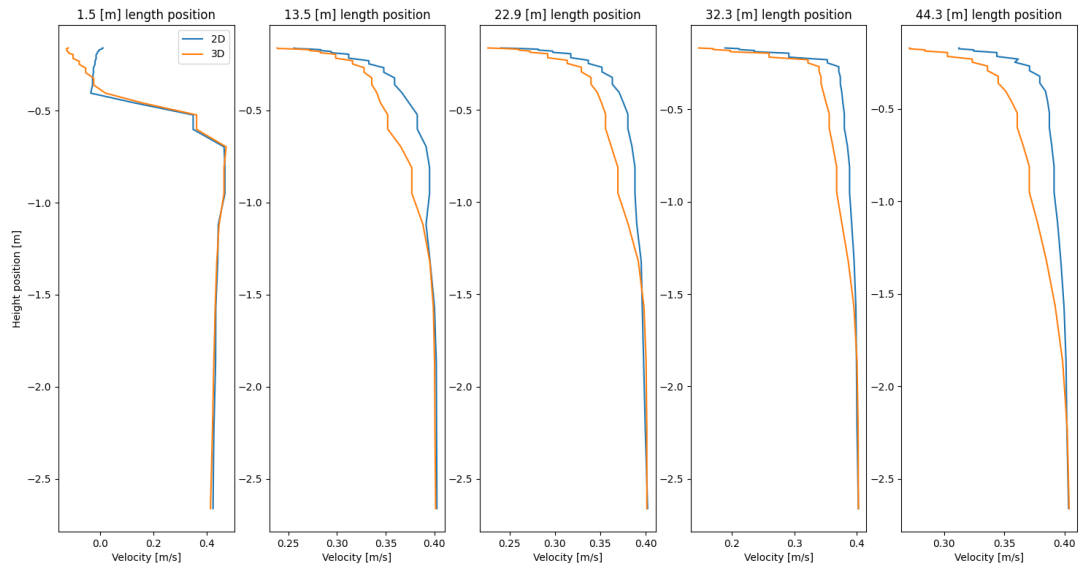


Figure 6.3: 2D LES velocity probes compared with 3D at $y=-5.1$ m and $y=-11.9$ m beneath array with 0° orientation.

6.2 Frequency of vortex shedding

Verification that 2D simulations are suitable for analysis can be done by examining vortex shedding frequency and determining if the resulting Strouhal number complies with literature.

The frequency of vortices shedding from the array may provide additional insight in how the numerical model performs. In 3D, these frequencies are not easy to distinguish due to the three-dimensional flow phenomena.

Theoretically, the frequency of vortex shedding is determined by the Strouhal number. For flat plates, this is defined as:

$$St = \frac{2fD}{U},$$

Where D is the submerged depth. Knisely (1990) shows that for large aspect ratios (depth is small compared to length), the Strouhal number has a value smaller than 0.10.

The frequency of vortex shedding is obtained through a Fourier analysis of the velocity probes beneath the array. Figure 6.4 and Figure 6.5 show the frequency of vortex shedding for a current amplitude of 0.4 m/s and 0.8 m/s, respectively, obtained with 2D simulations.

For the 0.4 m/s case, a peak is found especially for location 13.5 m at around 0.08 Hz for all different lengths of array. This could correspond with the vortex shedding. For the 0.8 m/s case, the shedding frequency should increase to around 0.16 Hz (see Figure 6.5). This is the case, but the peak is less pronounced.

For both current amplitudes, we obtain an estimate for the Strouhal number of approximately 0.06. This is consistent with literature and provides additional confidence for a well-defined numerical grid capturing the relevant flow phenomena in 2D.

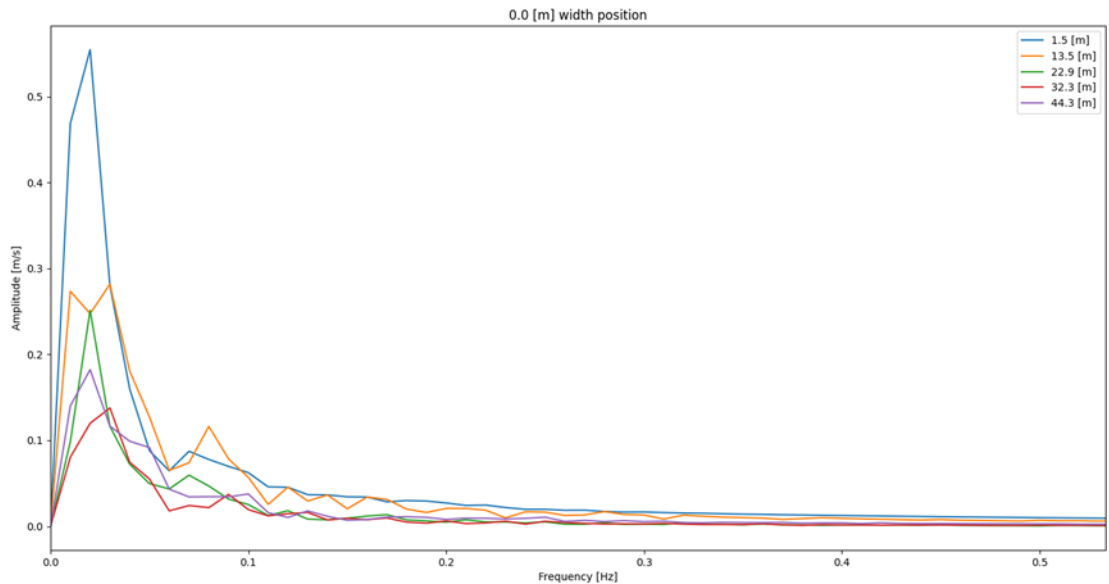


Figure 6.4: Fourier analysis LES results for 0.4 m/s at a distance from the front of the array. Length position 13.5 m shows to find a second frequency influence.

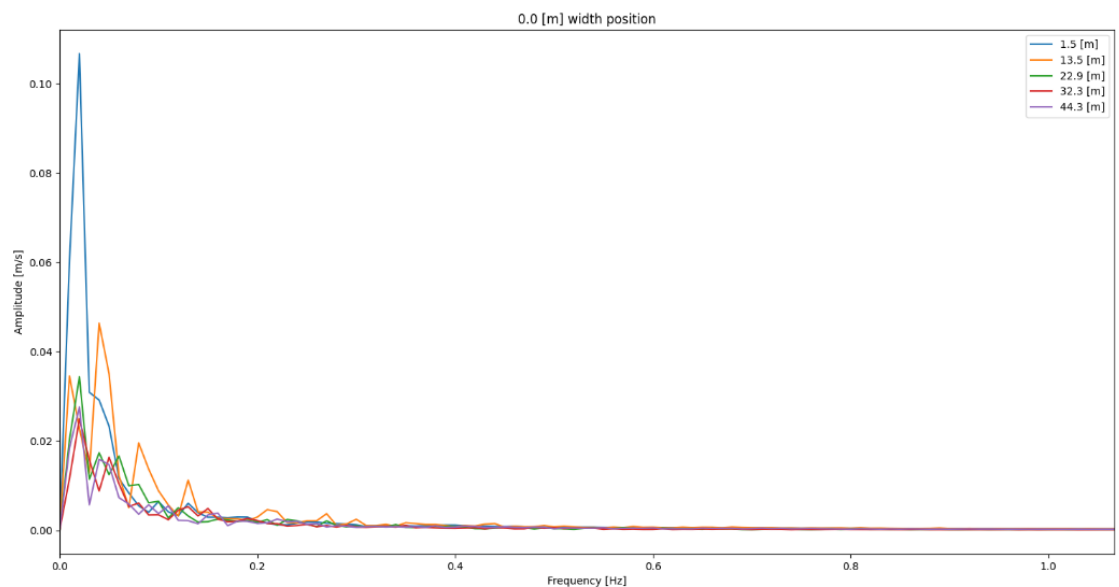


Figure 6.5: Fourier analysis LES results for 0.8 m/s at a distance from the front of the array. Length position 13.5 m and 22.9 m shown to find a second frequency influence.

6.3 Correction force & moment coefficients

To say something about the difference in forces and moments in 2D, as compared to 3D, a correction factor f is defined. This factor can give insights what the effect of the 3D flow features are on the forces.

The correction factor (f) of the force coefficient in 2D is defined as follows:

$$C_{3D} = f \cdot C_{2D}.$$

This formulation will be used for every coefficient by comparing with the 3D results in Table 5.2 for the orientation of 0°.

Not including the 3D effects results in the reduction of the coefficients, given in Table 6.1. The pressure coefficient in x-direction is hardly changed between the two cases. The large difference for the viscous coefficient in z-direction is explained by the difference in reference area due to the additional dimension.

Table 6.1: Correction factor for 2D force/moment coefficients.

Coefficient		3D	2D	f
x	1.21	$C_{p,x}$	1.01	1.20
	0.40	$C_{v,x} \cdot 10^3$	1.33	0.30

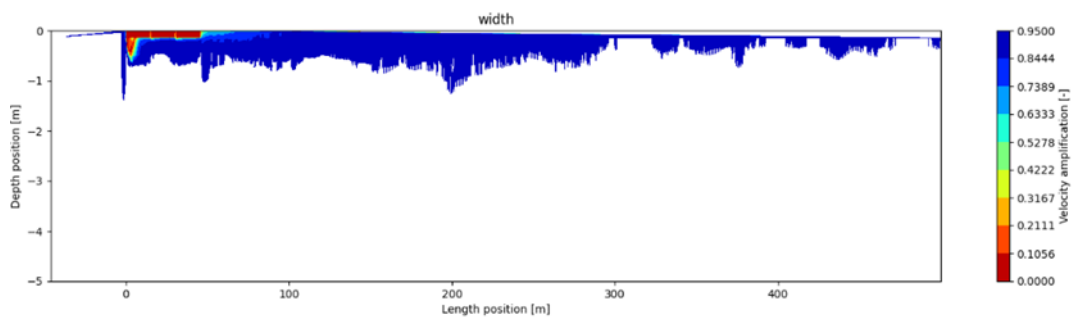
6.4 Wake length and depth

After verifying that the 2D simulation produce similar results as the 3D simulation, we now want to determine the wake length and depth. We take a similar approach as in Chapter 5. Thus, the flow velocity and TKE are time-averaged over the last 100 s. Then, they are separately used to determine the wake area. This area is defined by a 5% decrease in flow velocity or 5% increase in TKE relative to the benchmark (without an array).

The wake contour plots are shown in Figure 6.6. They both show different results when looking to the wake size and show that the wake depth due to the effect of a generated boundary layer is at least 0.5-1.0 m.

In Figure 6.6, we observe a sudden jump in TKE around $x = 200$ m. This jump cannot be explained by the coarsening of the grid, as this is located at $x = 150$ m. This is verified in Section 6.5, where the addition of array length is analyzed. In this section, the grid density change at location 150 m are moved, but the sudden jump for the 5% increase in TKE at 200 m remains the same.

Determining the wake length and depth based on the velocity decrease seems to be more reliable, as this shows a gradual return to the ambient conditions (Figure 6.6).



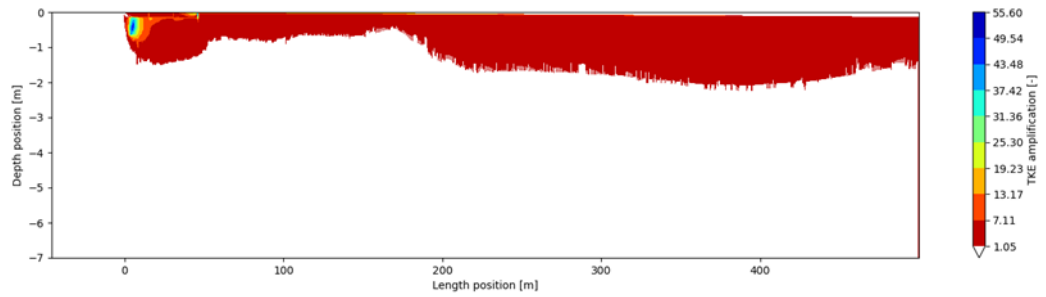


Figure 6.6: Contourplots of wake 2D domain for LES simulations averaged of 100 s. A vertical contour is shown with in the x-direction the length position and the y-direction the depth position. Top plot is for the velocity amplification and the bottom plot for the TKE amplification.

The 2D results show that at the far end of the domain (at $x = 500$ m), the wake has not entirely diffused. So, the wake extends even further than 10 times the array length.

Hence, to estimate the wake length, we need to extrapolate the wake diffusion. This is done using a linear fit from the flow velocity amplification. The fit is made on the averaged flow amplification over the top 2 meters and 20 meters length.

A linear fit is made in Figure 6.7 from 100 m onwards for the flow velocity amplification. The coefficients for the linear equation ($y = a \cdot x + b$) are given in

Table 6.2. The same was done for TKE from 300 m onwards, seeming to be less trustworthy, see Figure 6.7. The wake length for this configuration could be up to 20 times the array length.

It is difficult to accurately quantify the fit's accuracy because the wake depth is of a similar order as the grid size of 1.0 m at the end of the numerical domain. Additionally, adding a data point to the fit could significantly affect the length in the order of L , as even a slight change in parameter a can significantly impact the wake length.

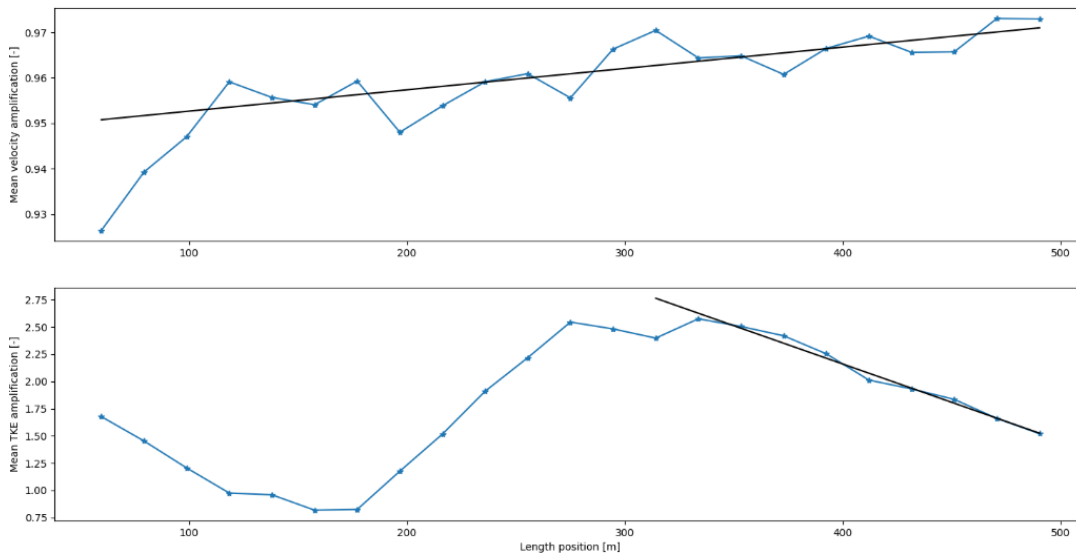
We have noted that the grid resolution at the end of the domain is likely to be insufficient as described in Section 0. Typically, multiple cells are needed over the wake depth for LES simulation to break down the eddies in smaller scales. Therefore, RANS results are also used to determine the wake length. Additionally, a verification simulation with LES CFD code TUDflow3D (De Wit, 2023) is done with a finer grid in the wake region. It uses a uniform grid of $dx=0.15\text{m}$, $dy=0.15\text{m}$, $dz=0.05\text{m}$. This can be considered as a mid-field LES simulation which has a sufficiently fine resolution in the wake region, but a coarser grid in the solar array region compared to the OpenFOAM LES simulations described in this report. The wake length of this mid-field LES is comparable to the wake length found from the OpenFOAM LES simulations. Furthermore, TUDflow3D showed hardly any difference between the application of rough wall functions or not for the wake length.

Furthermore, it is important to note that the LES results presented are averaged over time, which means that local eddies may reach a greater depth than what was found in the results.

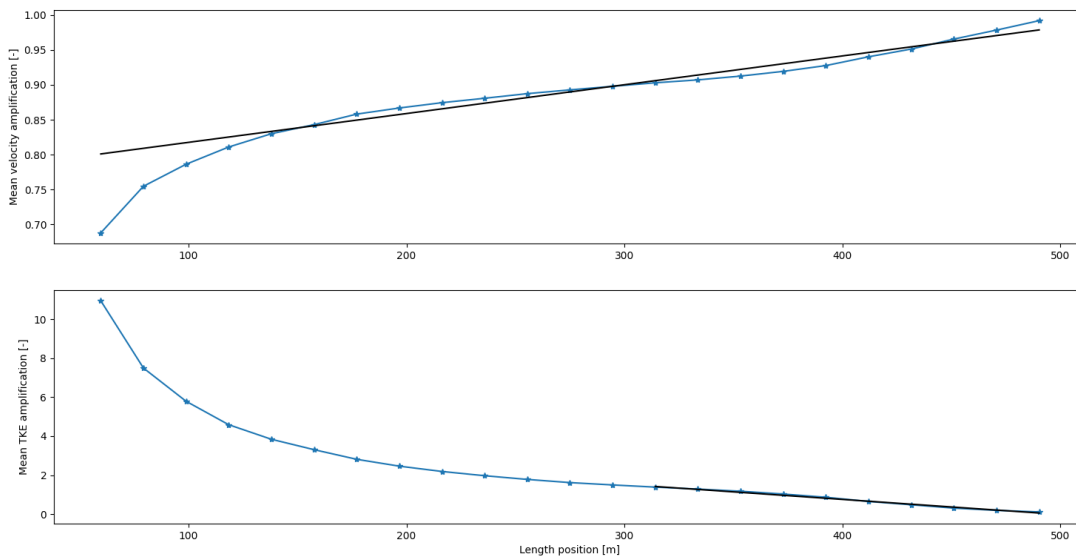
Other factors such as the movement of the array and waves may contribute to diffusing the wake. If the numerical grid is adequately designed and displays minimal diffusion, the computed wake will typically be a conservative estimate.

Table 6.2: Linear fit coefficients and estimation wake length.

Amplification	End wake in L	LES	End wake in L RANS	End wake in L mid-field TUDflow3D LES
Velocity U	24.2		11.8	22
TKE	12.3		8.0	14



(a) LES averaged over 100 s



(b) RANS

Figure 6.7: Fit of wake length for 2D domain for velocity and TKE for LES (a) and RANS (b).

6.5 Effect of array length on forces and wake characteristics

We started our analysis with a schematized array with a limited length. In the offshore application, array lengths may be longer. We perform 2D LES simulations for three different array lengths (see Table 3.1) to study how this affects:

1. the forces acting on the array; and
2. the generated wake.

The force and moment coefficients for the three array lengths are given in Table 6.3. When the array length increases, the viscous and pressure coefficient slightly decreases in x-direction and z-direction, respectively. This decrease takes place as the additional length experiences less forces due to the disturbed flow in x-direction.

On the other hand, the pressure coefficient in x-direction and the viscous coefficient in z-direction slightly increase with increase array length. The pressure coefficient is slightly increasing because of the frontal area of the individual solar platforms in the gaps which is not accounted for. Do remind yourself that the coefficients do not say anything about the force magnitude. The force magnitudes can differ quite a lot like is seen for Figure 5.5.

For an increase in array length, the moment coefficients decreases. The reason for this is that the point of application of the total acting force and the centre of rotation of the array are closer together.

Table 6.3: The effect of adding length to the array on the force/moment coefficients in 2D.

Coefficient		1L	2L	3L
x	$C_{p,x}$	1.20	1.33	1.46
	$C_{v,x} \cdot 10^3$	0.30	0.30	0.29

Snapshots of the wake averaged over the last 100 s of the LES simulations for different array lengths are shown in Section A.1.2-A.1.3 and can be compared with the original array length in Figure 6.6.

Wake depth becomes significantly larger with increasing array length, both based on flow velocity and TKE estimates. For both, wake depth appears to be proportional to wake length (L). For the wake area estimated using TKE, an array of $1L$ resulted in a wake depth of around 2 m, an array of $2L$ a wake depth of around 4 m, and an array of $3L$ around 6 m. We observe similar dependency for the flow velocity amplification.

The next step is to investigate how the array length affects the wake length. We study this following the approach from Section 6.4. While it may seem that the length of the array does not affect the wake (Appendix A.1), the linear fit is quite sensitive to the selected observation points.

It is expected that a deeper wake would lead to a longer wake length. However, this is not the case in Table 6.4 after extrapolation. A next step could be to extend the domain to prevent extrapolation.

Table 6.4: Wake length for different array lengths.

Length array	End wake in L LES		
	L	$2L$	$3L$
Velocity U	24.2	26.3	21.7
TKE	12.3	12.9	11.8
Length array	End wake in L RANS		
	L	$2L$	$3L$
Velocity U	11.8	12.2	11.2
TKE	8.0	8.2	8.2

6.6 The effect of current amplitude

To study the effect of tidal current amplitude, we perform an additional simulation using the standard array length and a current of 0.8 m/s. The force coefficients are given in Table 6.5. Similar trends appear as for the 3D case in Section 5.5. The viscous coefficients are lower when the current increases, which indicates an effect scaling with the Reynolds number.

Table 6.5: Force and moment coefficients in 2D for different current amplitudes.

Coefficient		0.4 m/s	0.8 m/s
x	$C_{p,x}$	1.20	1.22
	$C_v \cdot 10^3$	0.30	0.20

The results for estimated wake lengths show that the current amplitude only has a minor effect on wake length (Table 6.6). The linear fit for estimating wake length is shown in Annex A.1.4.

Table 6.6: Wake length for different current amplitudes with LES.

Amplification	Wake in L 0.8 m/s LES	Wake in L 0.4 m/s
Velocity U	25.7	24.2

Increasing the current has a similar effect on wake depth as increasing array length. The contour plane of the velocity magnitude and the velocity profile beneath the array are shown in A.1.4 (0.8 m/s) and A.1.1 (0.4 m/s). This is a similar conclusion as made in Section 5.5. The wake width gets smaller but the wake depth seems to increase (Knisely, 1990).

An increase of current using the same grid resolution results in less turbulent scales that are resolved (larger y^+ values). This may result in more dissipative results and requires additional attention in further research. Results for this current needs to be analysed with care.

7 Discussion

7.1 Comparison with other offshore structures

In this section, we compare our findings with earlier work on other marine structures, such as monopiles and jackets. Though floating solar platforms are fundamentally different than those structures, there are some interesting analogies.

The wake size for monopiles scales with the monopile diameter. Wake width is around 10 times the diameter, while wake length is up to 50 to 60 times the diameter (e.g. Schultze et al., 2020; Hendriks et al., *in prep*). Monopiles used for offshore wind turbines are currently in the order of 10 m in diameter. This means that the wake length can reach up to 500 m. This is similar to the size of the solar platform array investigated in the report. The wake width for the solar platform array is not more than 1.45 times the characteristic width of the array when rotated, which is smaller than that of a monopile in ratio to the characteristic dimension. One major difference is that the wake induced by monopiles covers the entire water depth, while the wake depth for the solar platform array is limited to a few meters below the water surface.

Flow shedding effects depend on the shape of the structure, which is different for floating solar platforms than for cylindrical shapes. The dimensionless Strouhal number increases with the bluntness of an object. Additionally, the shedding around a monopile, from both side in a horizontal plane, can interact, which is less likely for a solar platform array due to its large horizontal dimensions. Complex flow phenomena such as horse-shoe vortices are a common flow feature around monopiles but are not expected for floating solar arrays.

It is unlikely for monopiles or jackets to develop a boundary layer, which has been shown to be relevant for the wake size of floating solar systems. However, it is important to note that not all flow phenomena relevant for floating solar are applicable to offshore foundations like monopiles and jackets. Since the solar array is floating and has a relatively shallow depth, waves become more influential, possibly diffusing the wake. Additionally, the fluid-structure interaction may be affected as the array has some freedom to move.

7.2 Recommendations related to CFD

For a follow-up study some recommendations are given that can be performed to gain a better understanding of the wake size of a solar array:

- Verify the estimation of the wake length by performing LES simulations in 2D for an extended domain and refined downstream grid. Current LES results are not reliable enough for given grid resolution at the end of the domain. To gain more insight, further research with a larger domain is required. Further research is needed to investigate this for a longer domain
- To ensure accuracy, use a finer grid for the case with current 0.8 m/s. Apply these results to additional current velocities (and orientations) to form a trend and database.
- Determine the individual effects of a solar platform and gap distance on the global wake.
- Conduct simulations with a general grid refinement in 3D to observe the effect on the results, such as dissipation of wake, viscous forces, wake depth using TKE contours, resolved turbulence, and flow separation. The grid refinement should be applied in the wake as near the array the y^+ criteria is satisfied.
- Analyse the effect of marine growth in greater detail as it can be substantially larger than the grid size used, affecting both the wake and acting forces.

- To obtain the shedding frequency, perform simulations with a lower Courant number. More simulation results e.g. a lower Courant restriction are needed to verify the Strouhal number.
- Compare the obtained results with experimental results to quantify the accuracy of the numerical results.
- The uncertainty in applying rough wall functions requires additional research.

8 Conclusions and recommendations

The purpose of this investigation is to assess the impact of a solar platform array on the local and surrounding hydrodynamic conditions. The results of this assessment will be utilized to create input for larger-scale models to account for effects like e.g. the wake, and to provide a basis to analyse its potential environmental impacts resulting from changes in the hydrodynamic conditions.

The formation of a wake behind a solar platform array is caused by the resistance of the structure against the flow caused by drag and friction resistance. The presence of the solar platform array either leads to a local reduction or amplification of the flow velocity, due to formation of a boundary layer at the bottom surface of the platforms, redirection of the surface near flow and turbulent shedding effects. These flow characteristics are rather complex and require a high level of detail and advanced tools to be resolved. Thus, the investigation employs Computation Fluid Dynamics (CFD) and the software library OpenFOAM to model the flow characteristics and associated phenomena. Since CFD is a computational expensive numerical technique, the size of the computational domain and the refinement of the same is limited. To enable the investigation of certain effects, which require a specifically large domain, certain investigations in this study take place in a simplified 2D approach, while the majority of simulations is in 3D.

To get a better understanding of the interaction between the solar platform array and the local flow conditions as well as the developing wake, it is important to model the flow deflection, amplification and detachment around the array accurately. This requires also the modelling of turbulence. In this investigations two different approaches in turbulence modelling have been applied: RANS modelling with the two-equation solution of the k-omega-SST model and a LES approach based on the dynamic k-equation. The RANS simulations provide the opportunity of reduced computational costs, while modelling merely the effect of turbulence in form of a turbulent viscosity, while LES is significantly more expensive but also models the larger turbulent features more accurately, while the influence of only the smaller eddies are modelled via a sub grid model. In this investigation, both models were applied to save computational costs by using the RANS approach to generate an initial state, before starting the LES simulation.

General observations

Prior to the actual investigations a number of effects have been investigated in sensitivity analysis. Amongst other, the effect of the rather small gaps between the platform arrays has been tested. The simulation show, that the gaps do indeed affect the development of the wake and should be included in the simulations. Another aspect that is discussed is the applicability of 2D simulations over 3D for determining the wake length.

The first simulations results of the 3D simulations show a boundary layer development beneath the array resulting in a wake behind the array. The wake is defined as a 5% deviation of the initial conditions. Besides the boundary layer development, it is observed that local flow shedding at the corners of the total array, but also at the corners of the individual solar platform, contribute to the wake in depth but also in width. The results are most of the time averaged over 100 s. The observations are based on the mean flow while the wake can reach deeper on individual time instances.

The horizontal area of 5% deviation of the current speed, called the wake, is hardly changing over the vertical direction. It is observed in Section 6.4 that the wake length can be in the

order of 10-20 times the investigated solar array length for the investigated hydrodynamic conditions.

Related to the forces and moments acting on the solar platform array, the pressure forces are of a higher order than the viscous forces. Note that the pressure forces can substantially increase when marine growth is considered due to the increase in frontal area. A suction force on the array into the water can be experienced. The pitching moment, using the axle system of the current direction, is of a higher order than the sway and rolling moment. Shedding effects are experienced with a Strouhal number of around 0.06 in 2D LES simulations.

Three different parameters of either the hydrodynamic conditions or the array placement are varied in this investigation to gain a better understanding on the flow interaction with the array:

- 5 solar array orientations
- 2 free stream velocity magnitudes
- 3 different dimensions of the solar array

Below the main findings per topic, based on the variations made, are summed for the given setup described in this report. More in-depth observations are described in the relevant chapter.

Array orientation:

- Wake depth for the 3D simulations can increase by more than a factor 3 by rotating the array. This can be influenced by the aspect ratio of the array and individual solar platforms, and mainly caused due to shedding. The flow shedding seems to diffuse earlier than the wake due to drag, resulting in a boundary layer development.
- Rotating the array results in a larger spreading of the wake in the horizontal direction. This can be up to a 40% wider wake for a current of 0.4 m/s when oriented between 0 and 90 degrees. The spreading is relatively constant over water depth for the considered orientations.
- Forces vary up to several orders, depending on array orientation relative to the current direction.

Free stream velocity:

- An increase in current velocity results in a change in wake spreading. This can be up to 10% decrease in the horizontal width of the wake spreading for the given setup.
- The wake depth for 3D and 2D case remain of similar order by a current increase of 0.4 m/s to 0.8 m/s.
- A linear fit of the wake profile in vertical direction is used to determine the total wake length. The wake length is likely to be longer for a 0.8 m/s current over 0.4 m/s (within the order of 10%).

Size of array length:

- The wake depth generated by a developed boundary layer scales with the array length.
- The addition of array length affects the pitching moment. The point of application of the total force is likely to move towards the centre of gravity.
- The additional length experiences a less proportional increase of the frictional forces for the given configuration. The increase in area due to the addition in length resulted in a

less proportional (not linear) increase of the friction forces. The relevance of frictional forces was decreased with only one percent for an increase in length of 300 percent.

- The wake length does not scale with array length and requires additional research.

This report does not cover all parameter variations but does give first insights in the hydrodynamics effects of floating solar. This has not been published before.

This study gave first insights into the complex interaction between a large scale solar platform array and the surrounding hydrodynamic conditions. However, due to the even larger size of potential solar arrays by an increase in number of solar platforms that in reality will be applied, it should be further investigated, how some of the observations are affected by the choice in solar array size. Another point is the dynamic behaviour of the solar platform arrays. Since the individual platforms are flexible, it is expected, that they will react individually to the flow and adapt their position due to restoring forces. Modelling the solar platforms dynamically will probably affect the results of the flow interaction. However, a dynamic approach is even more numerically demanding and the results of this study are expected to give a good impression on the actual effect of the solar platform arrays in the field.

9 References

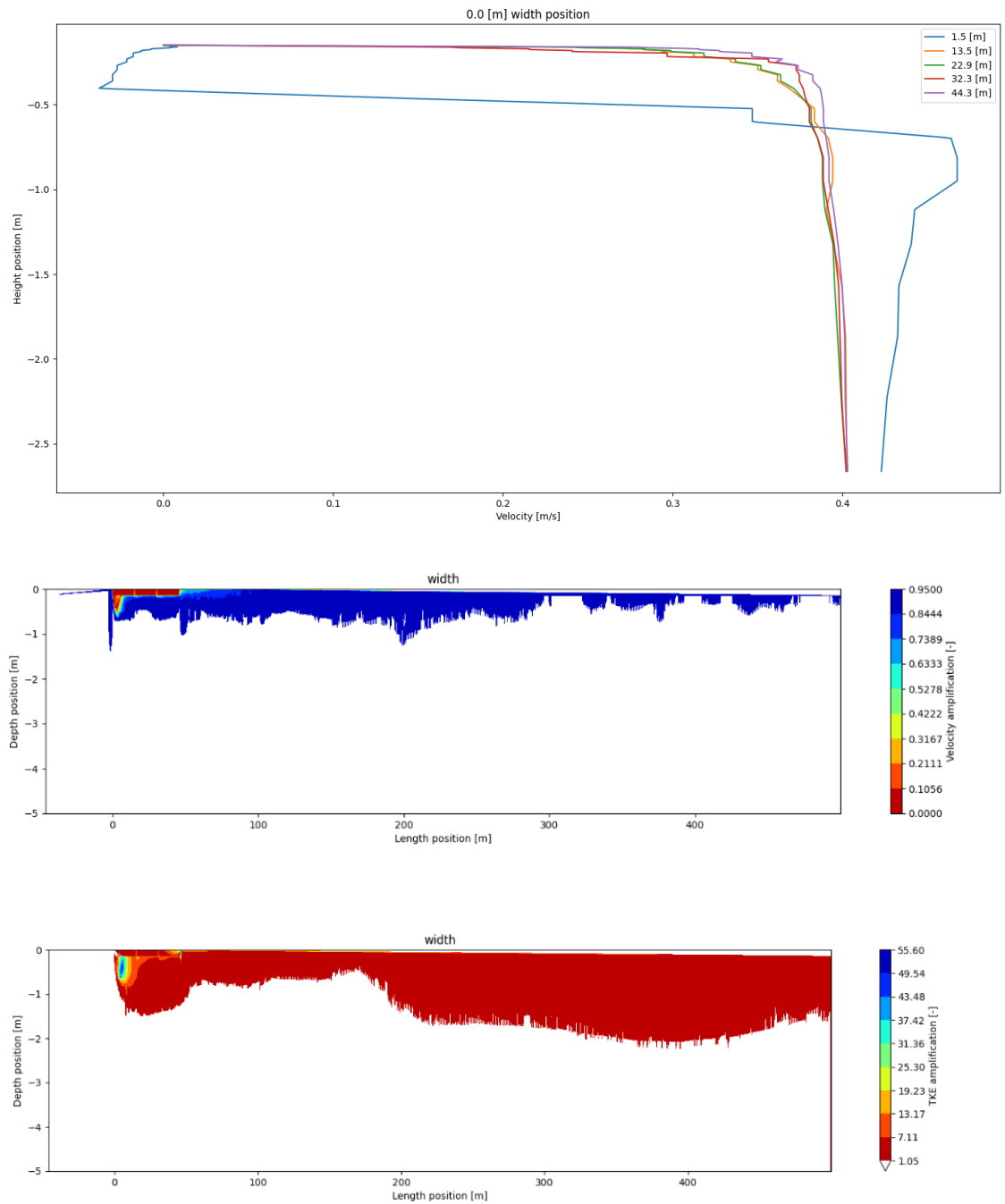
- Beehook, A. (2015). Beehook, Abhinivesh. *Unpublished MSC by Research Thesis*. Coventry University Coventry.
- Blasius, H. (1907). *Grenzschichten in Flussigkeiten mit kleiner Reibung*. Druck von BG Teubner.
- De Wit, L., D. Plenker, Y. Broekema. (2023). 3D CFD LES process-based scour simulations with morphological acceleration. *11th ICSE conference Copenhagen*.
- Eça L., P. F. (2018). Viscous flow simulations at high Reynolds numbers without wall functions: Is $y^+ \approx 1$ enough for the near-wall cells? *Computer & Fluids*, 157-175.
- Incropera, F. a. (1990). *Fundamentals of heat transfer*. New york: Wiley.
- Kim, J., Parviz, M., & Moser, R. (1987). Turbulence statistics in fully developed channel flow at low Reynolds number. *Journal of Fluid Mechanics*, 177, 133-166.
- Kim, M. a. (2019). Large-eddy simulation with parabolized stability equations for turbulent transition using OpenFOAM. *Computer & Fluids*, 108-117.
- Kim, W.-W. a. (1995). A new dynamic one-equation subgrid-scale model for large eddy simulations. *33rd aerospace sciences meeting and exhibit*, (p. 356).
- Knisely, C. W. (1990). Strouhal numbers of rectangular cylinders at incidence: a review and new data. *Journal of fluids and structures*.
- Oceans of Energy. (2023). Dimensions of offshore solar platform. Shared with Deltares by email on 12 June 2023.
- Patel, V., & Head, M. (1969). Some observations on skin friction and velocity profiles in fully developed pipe and channel flows. *Journal of Fluid Mechanics*, 38, 181-201.
- Pope, S. (2000). *Turbulent flows*. Cambridge; New York: Cambridge University Press.
- Rostami, A. B. (2019). Strouhal number of flat and flapped plates at moderate Reynolds number and different angles of attack: experimental data. *Acta Mechanica*, 333-349.
- Sanjay, S. a. (2019). Numerical simulation of flat plate boundary layer transition using OpenFOAM. *AIP Conference Proceedings* (p. 2112). AIP Publishing.
- Schlichting, H. a. (2000). Boundary layer theory. *Eighth Revised and Enlarged Edition*.
- Weller, H. T. (1998). A tensorial approach to computational. *Computers in Physics*, 620-631.

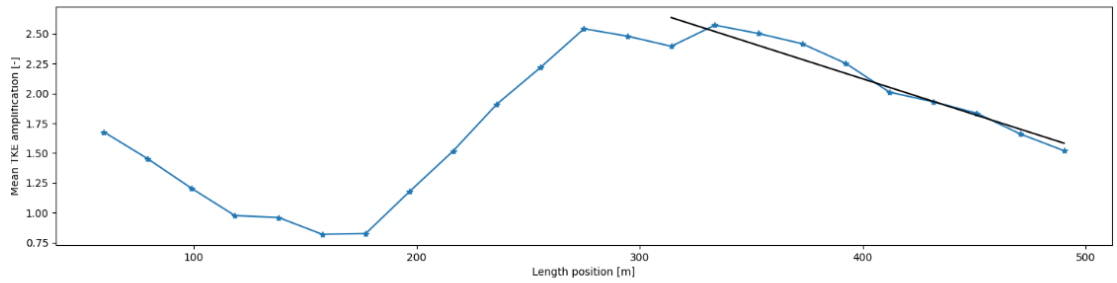
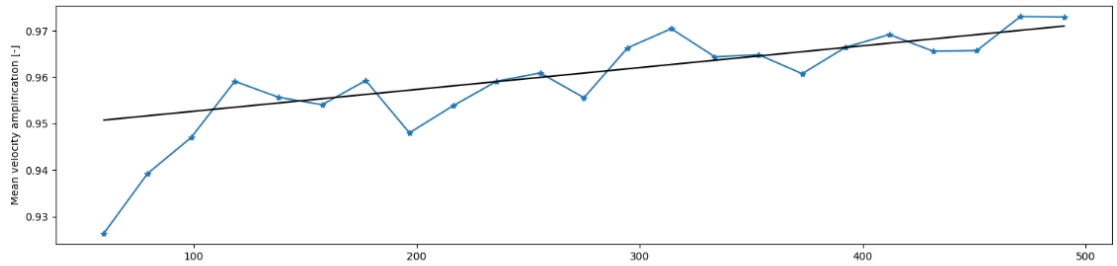
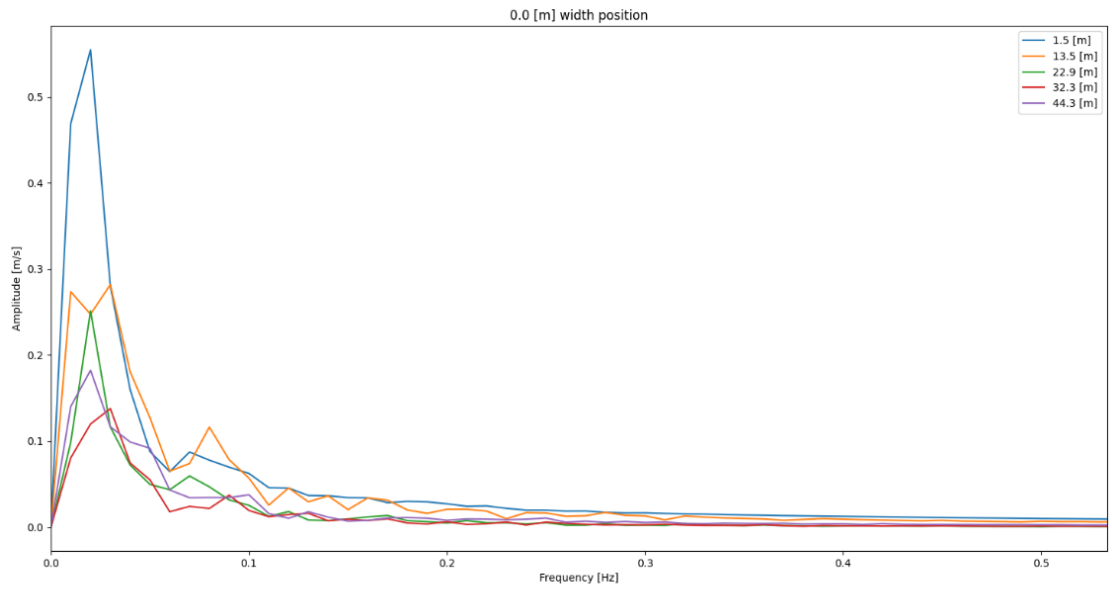
A Simulation results

Most figures and illustrations are self-explanatory and further details can be found in Chapters 5 and 6.

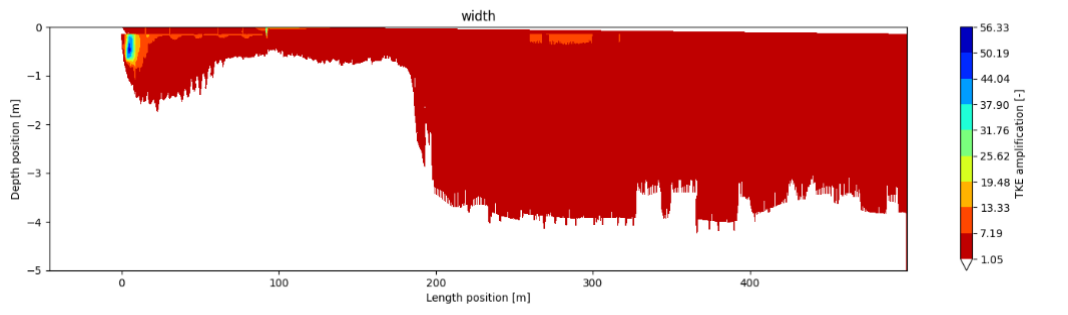
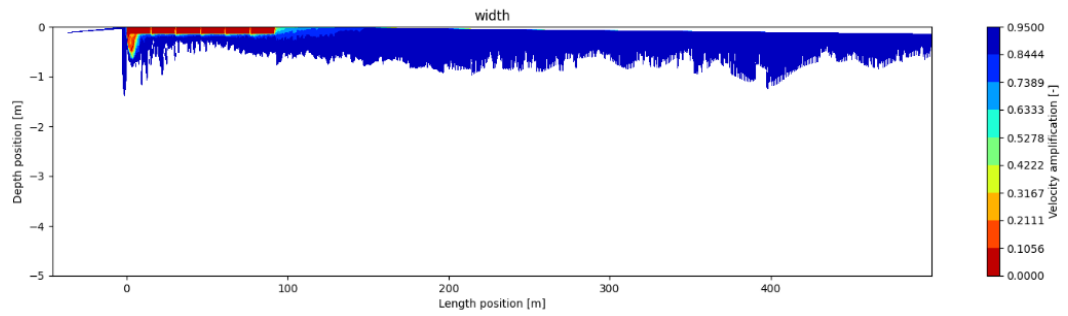
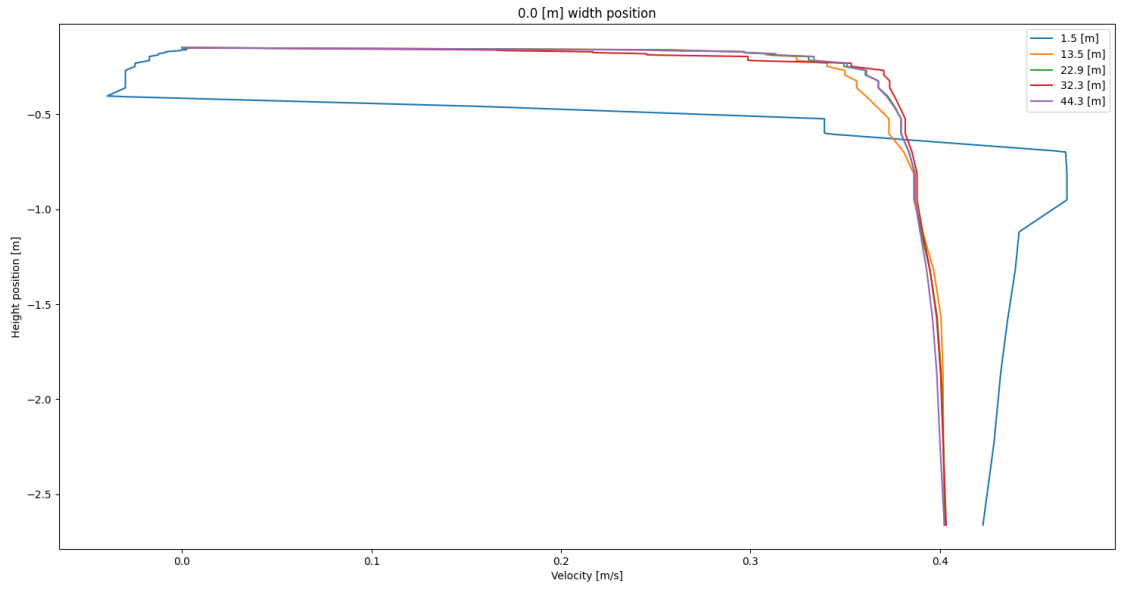
A.1 2D

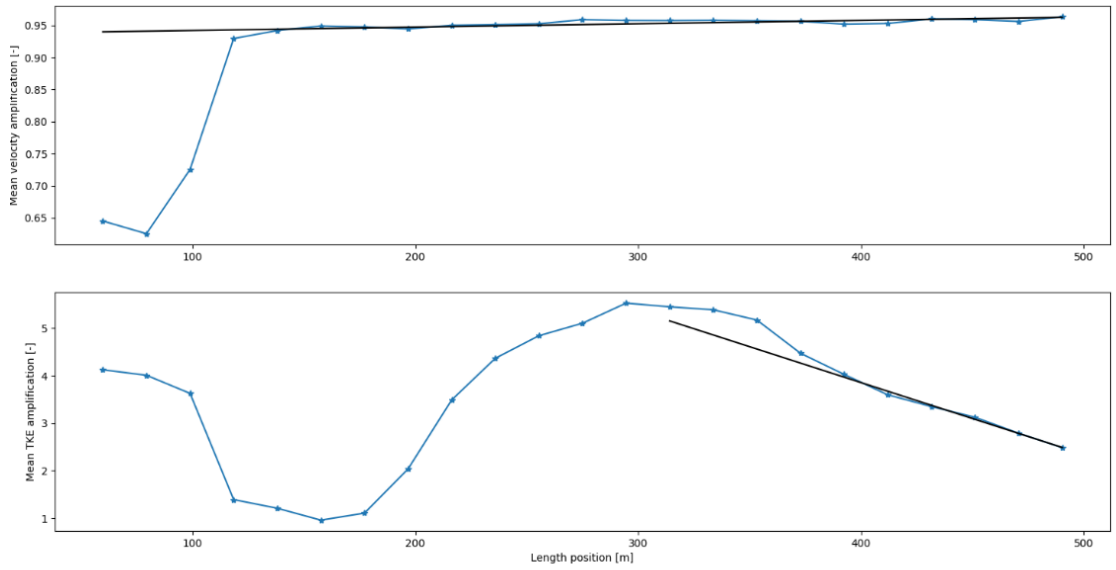
A.1.1 1L – 0.4 m/s



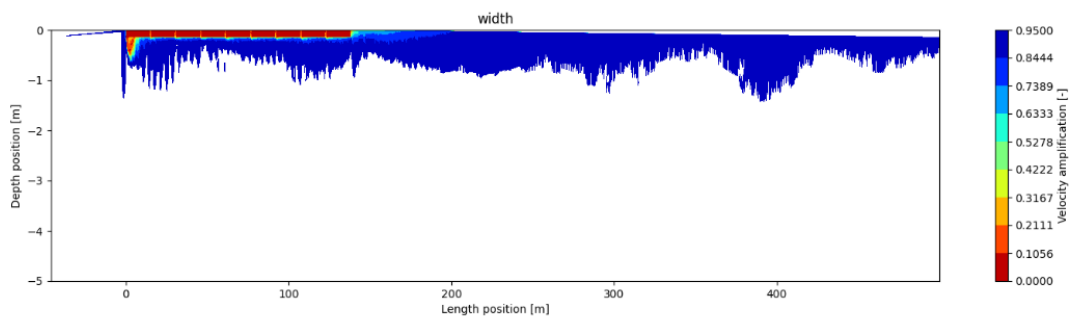
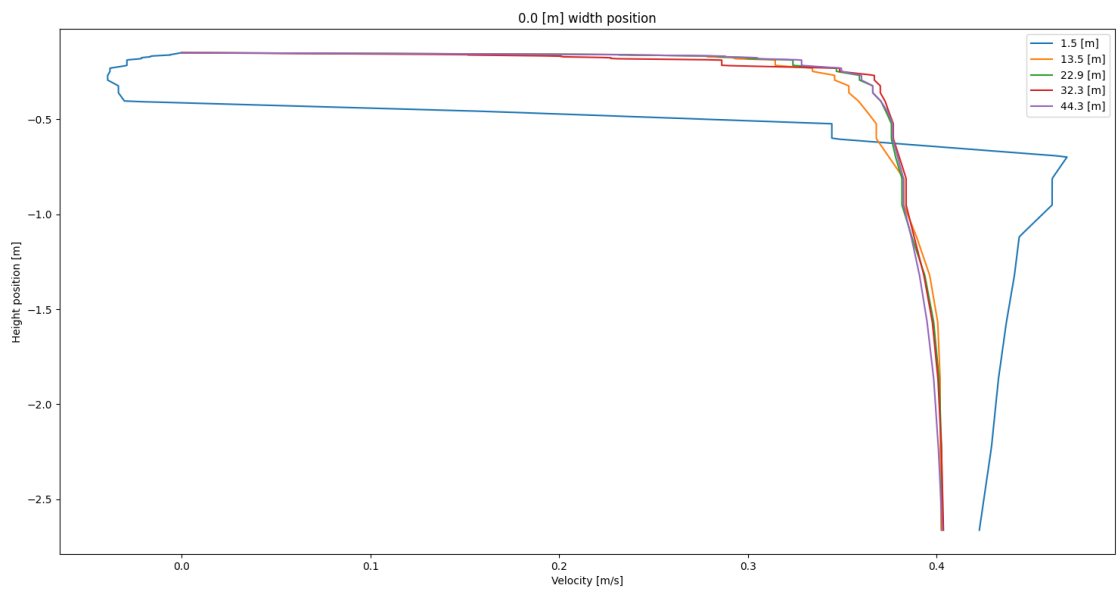


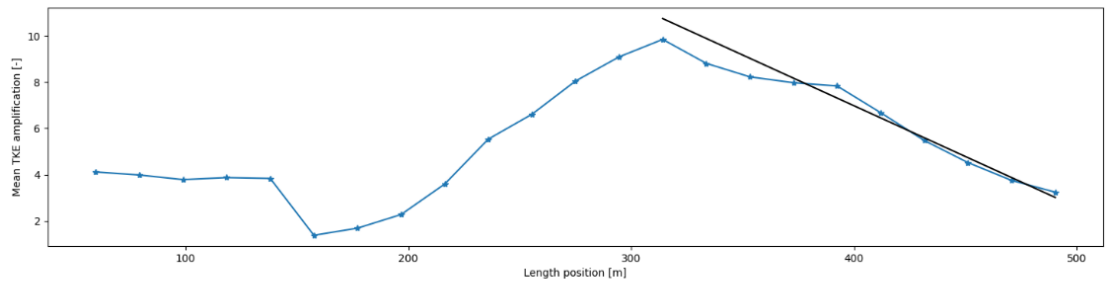
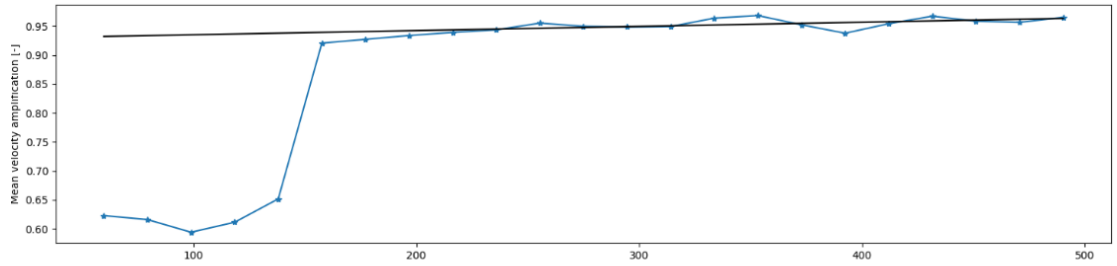
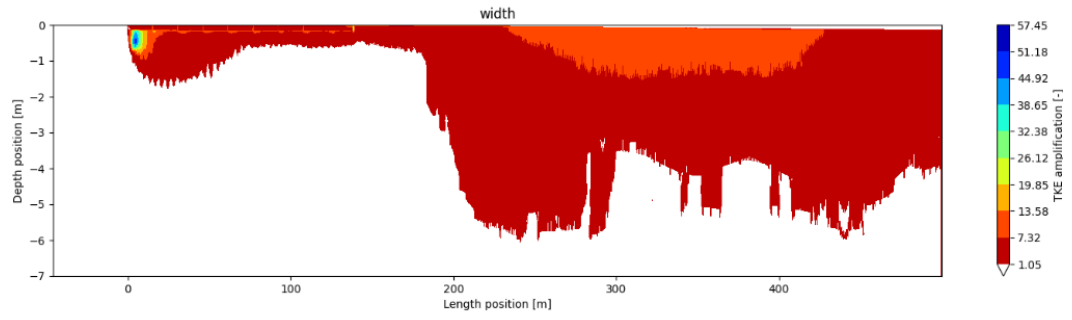
A.1.2 2L – 0.4 m/s



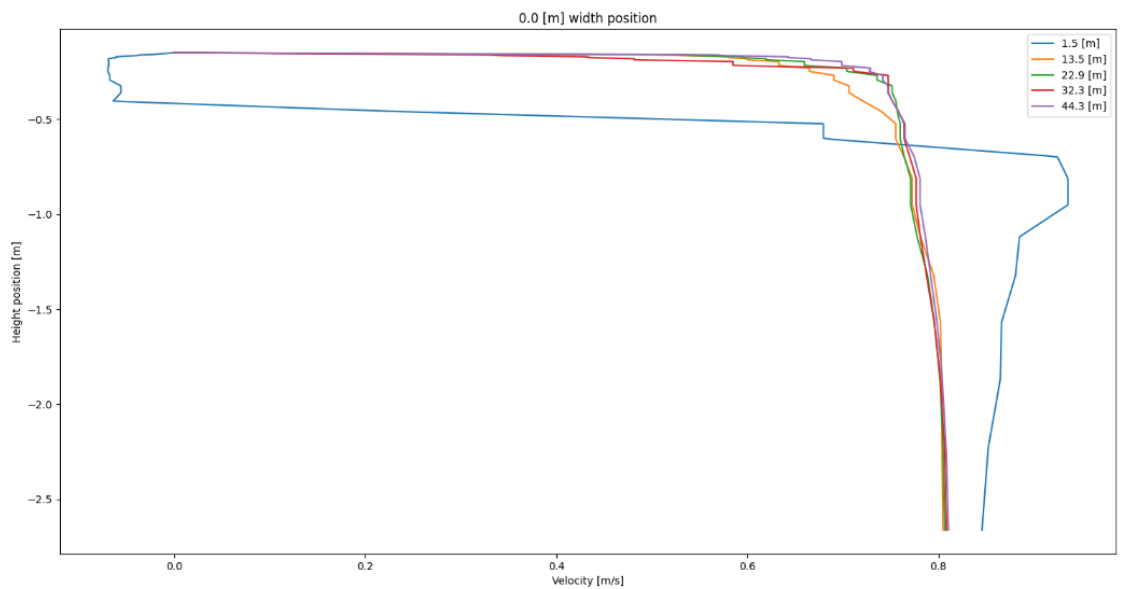


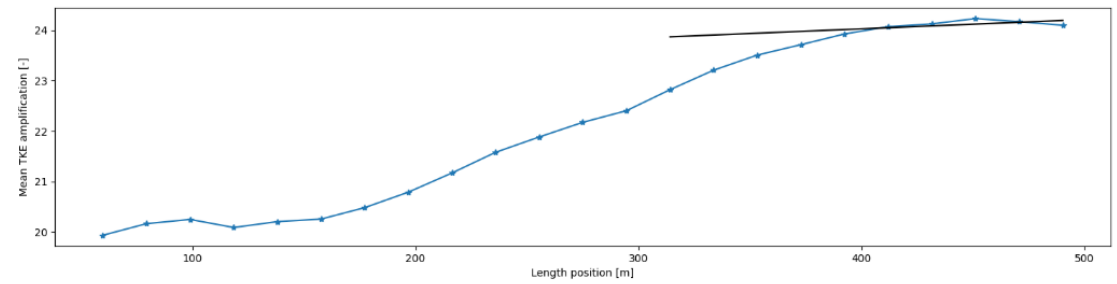
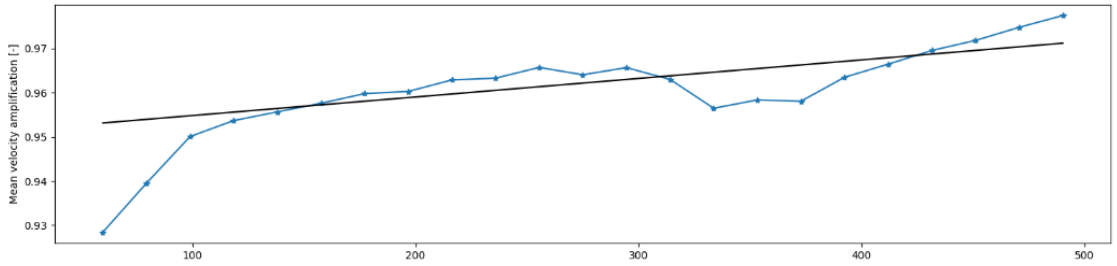
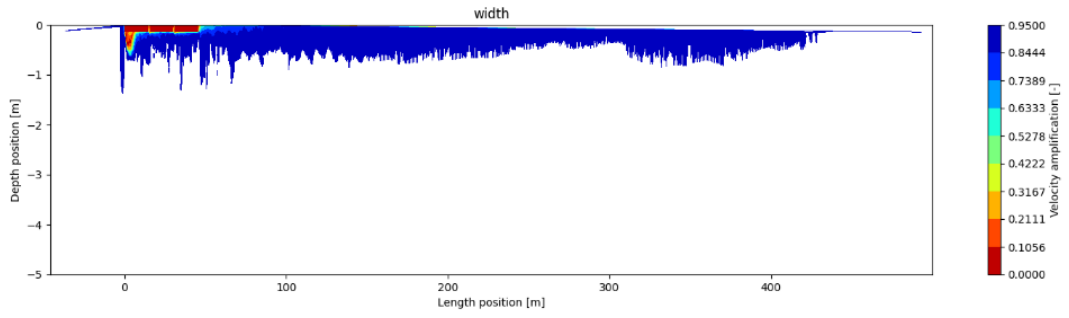
A.1.3 3L – 0.4 m/s



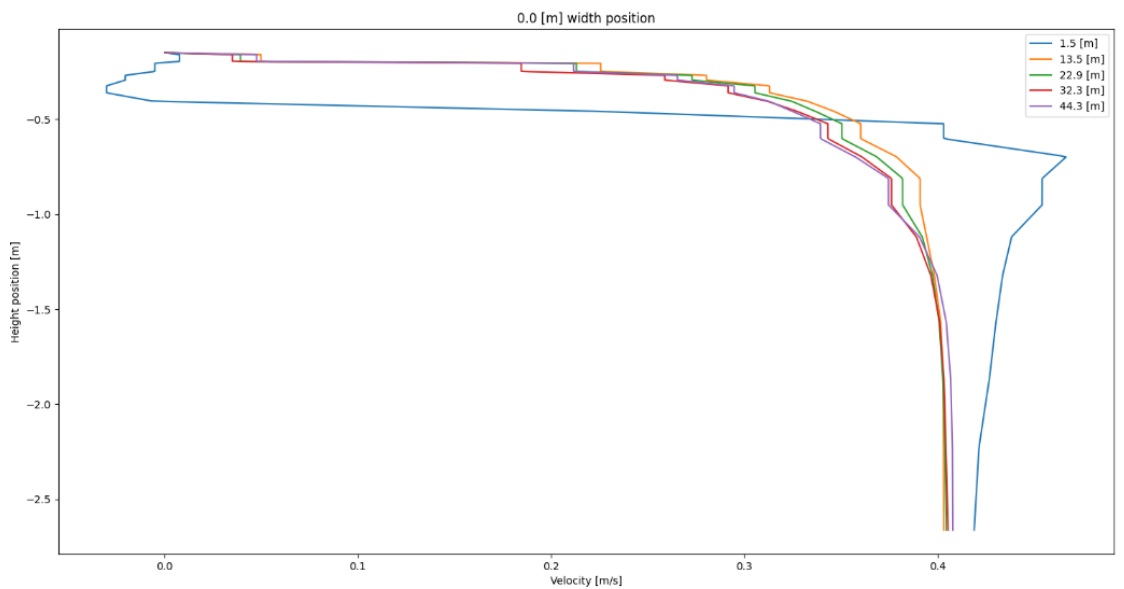


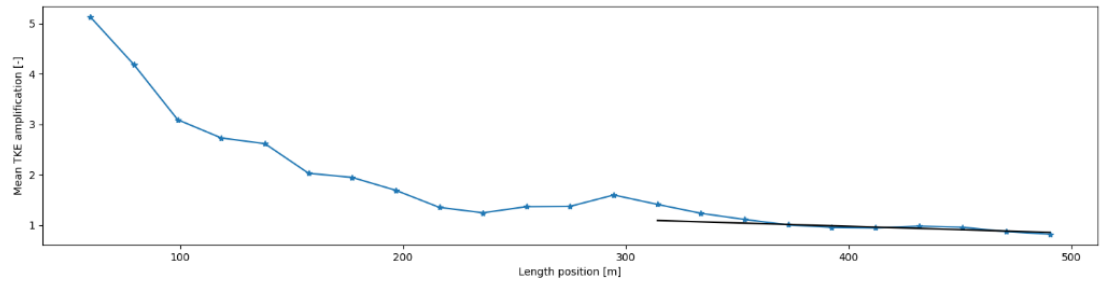
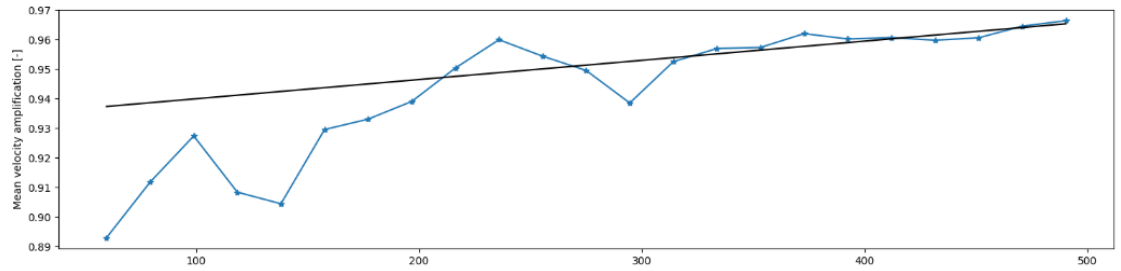
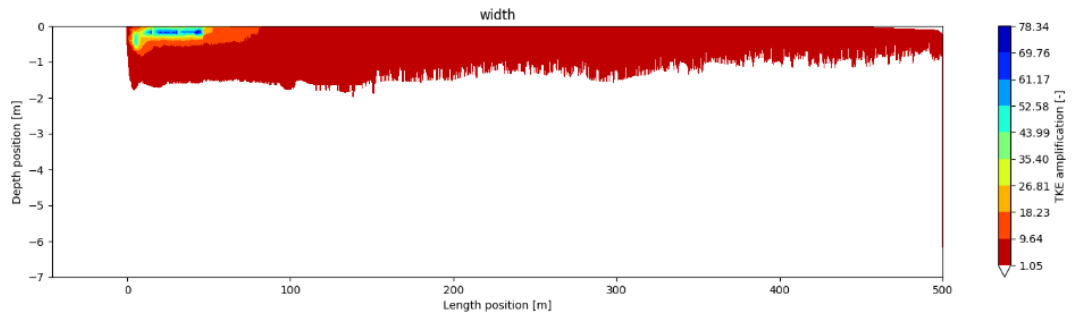
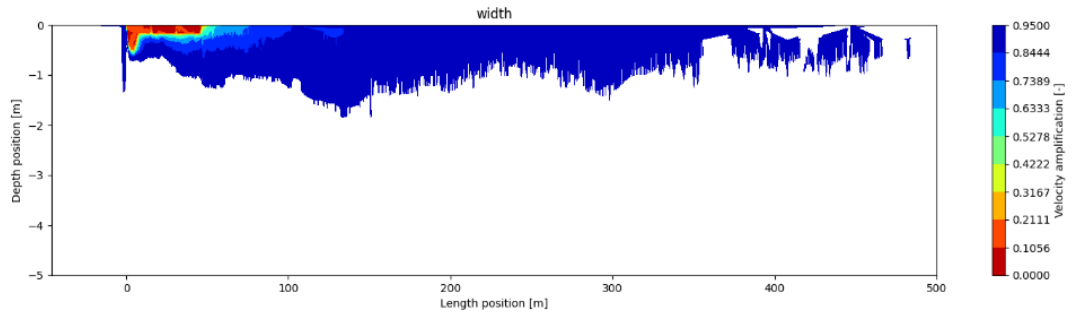
A.1.4 1L – 0.8 m/s





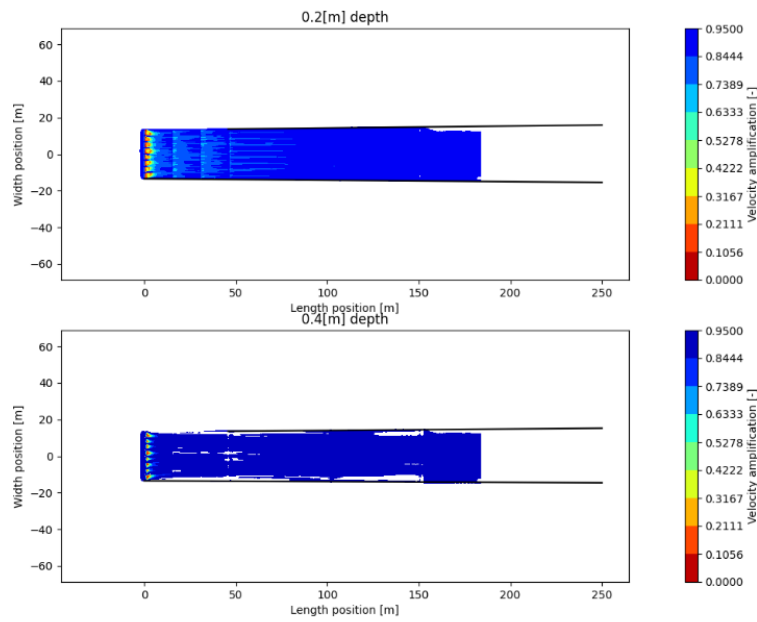
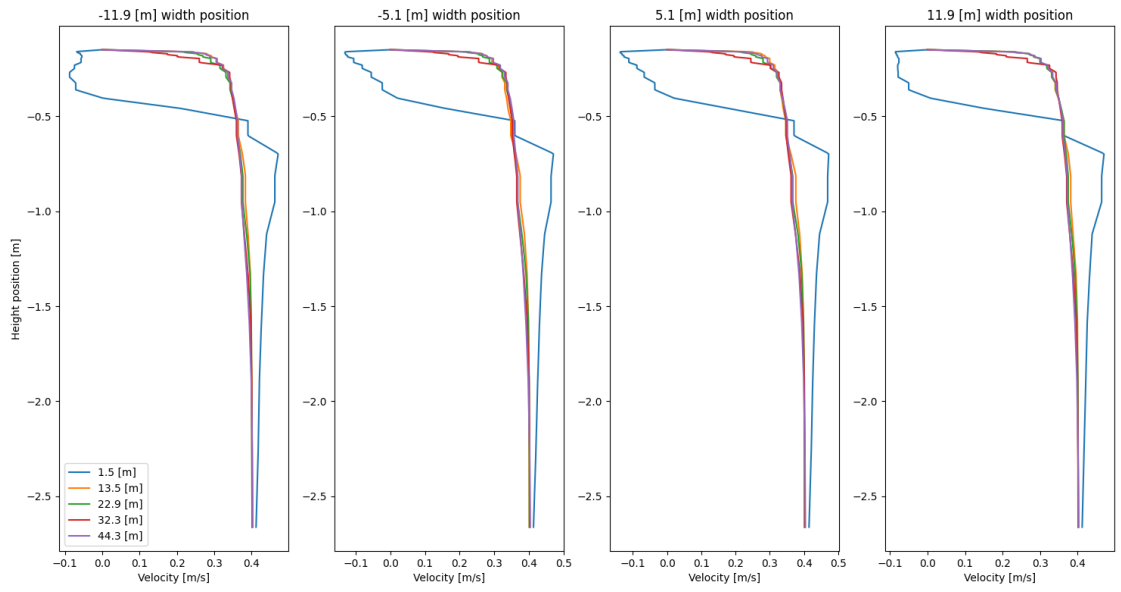
A.1.5 1L – 0.4 m/s – rough high-Reynolds wall function

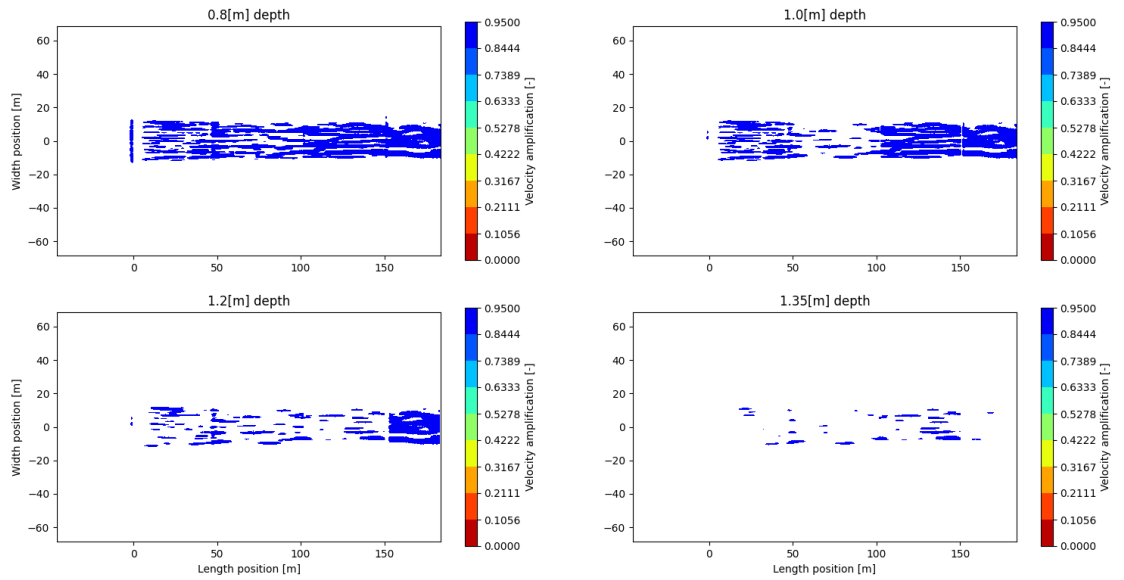
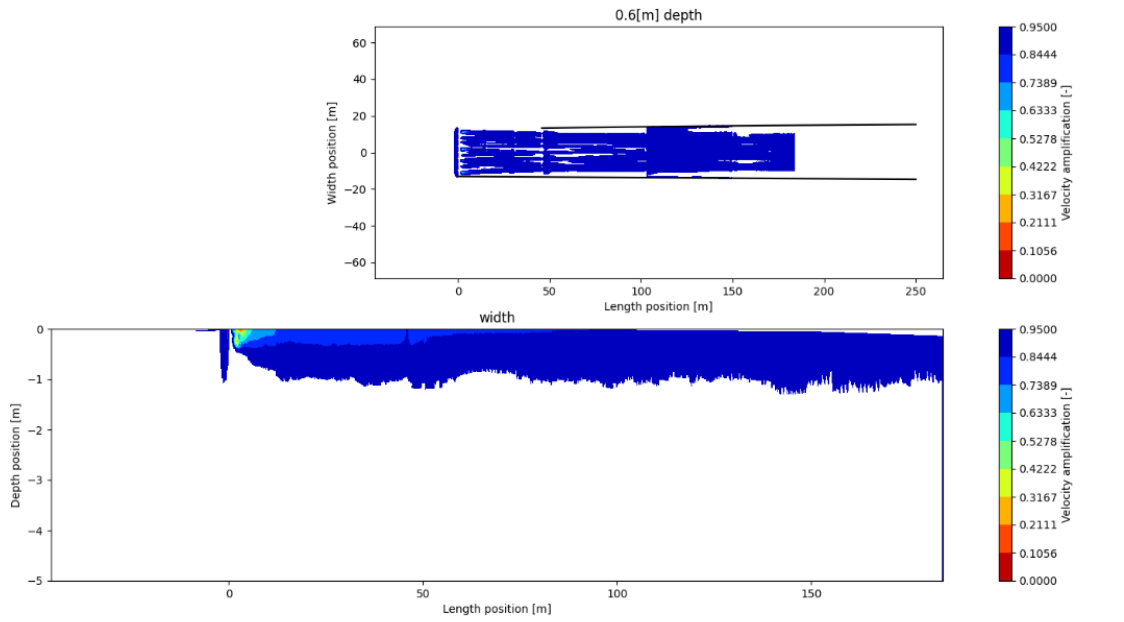


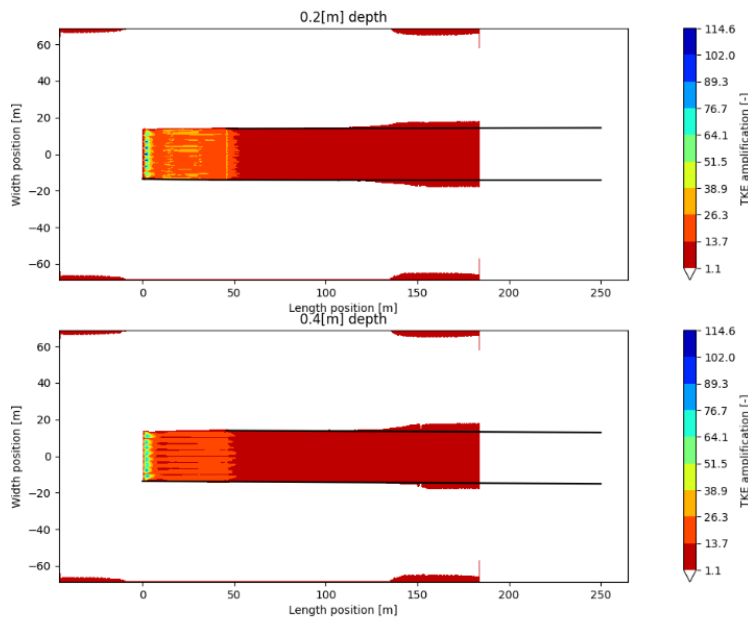
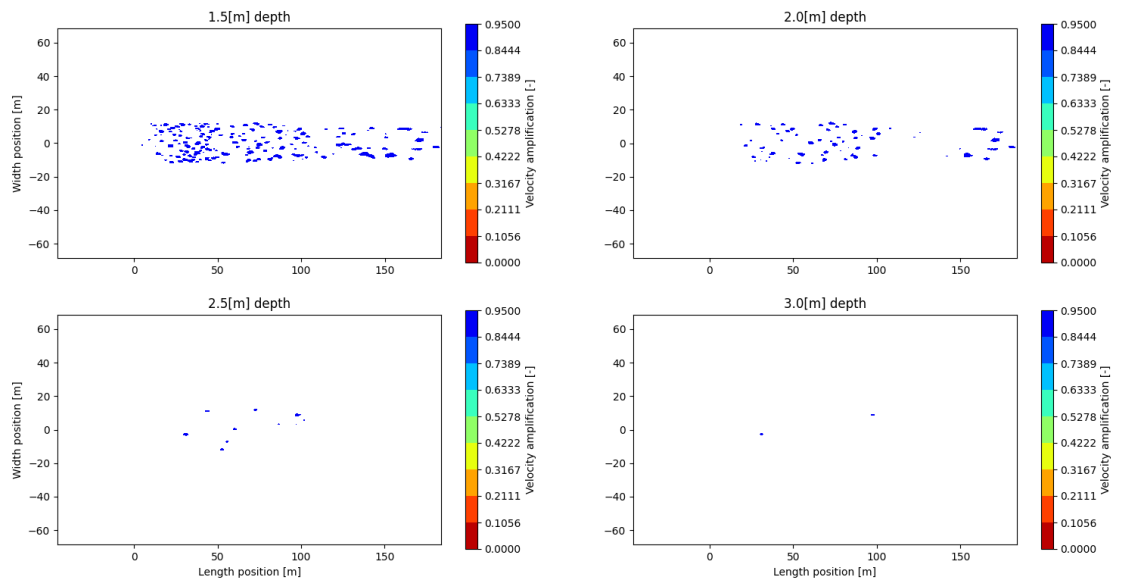


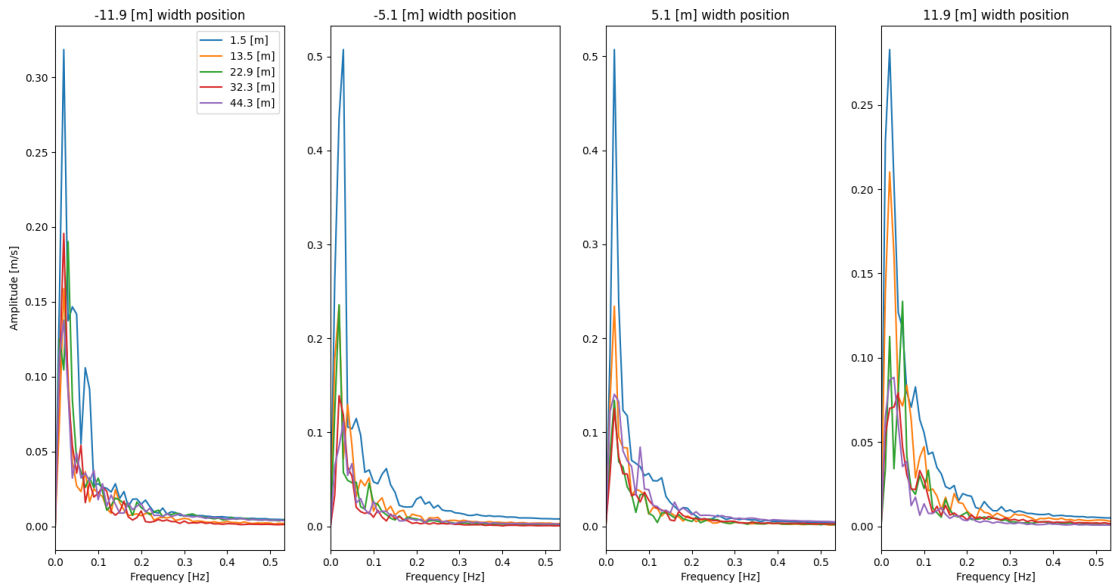
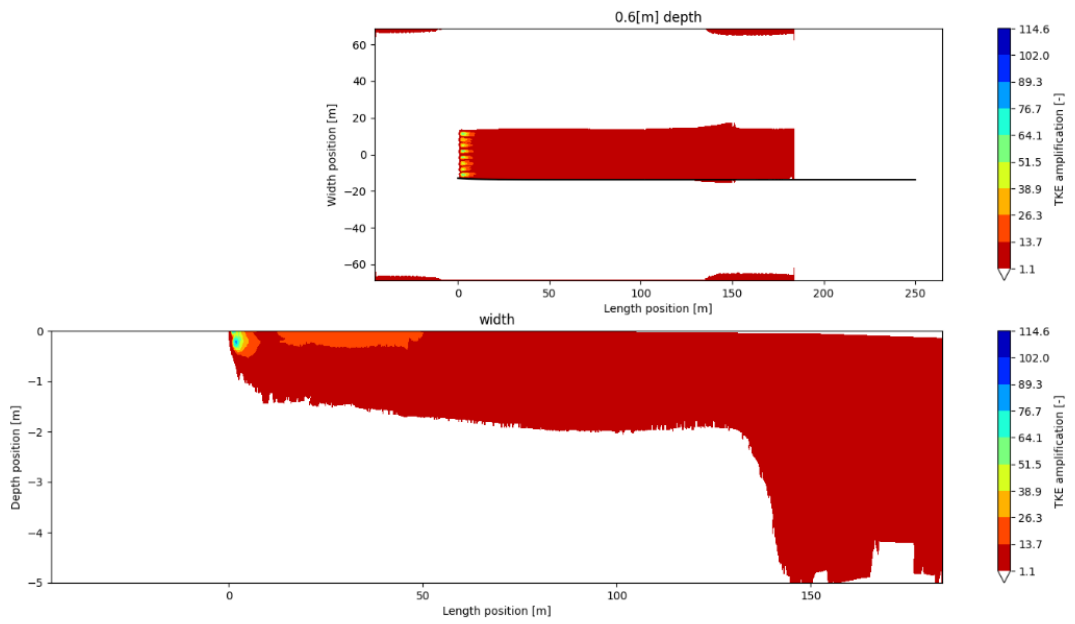
A.2 3D

A.2.1 0 degree – 0.4 m/s

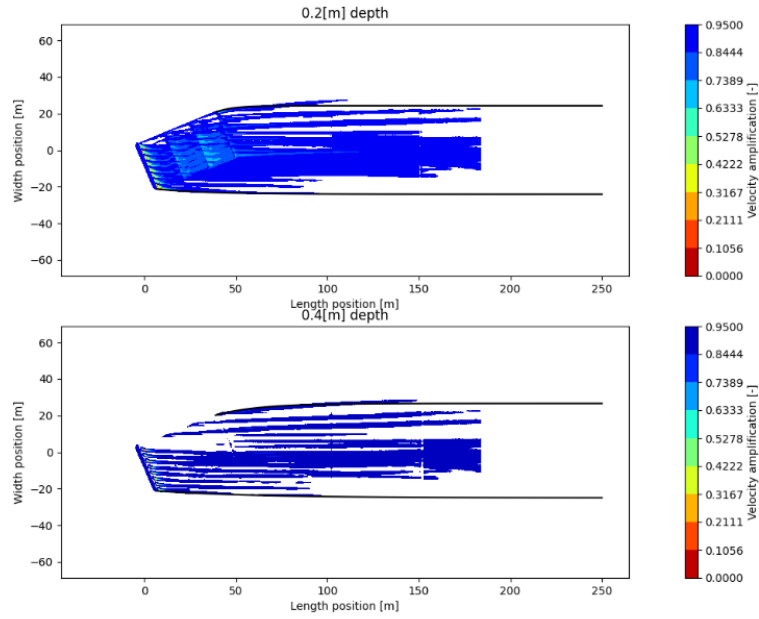
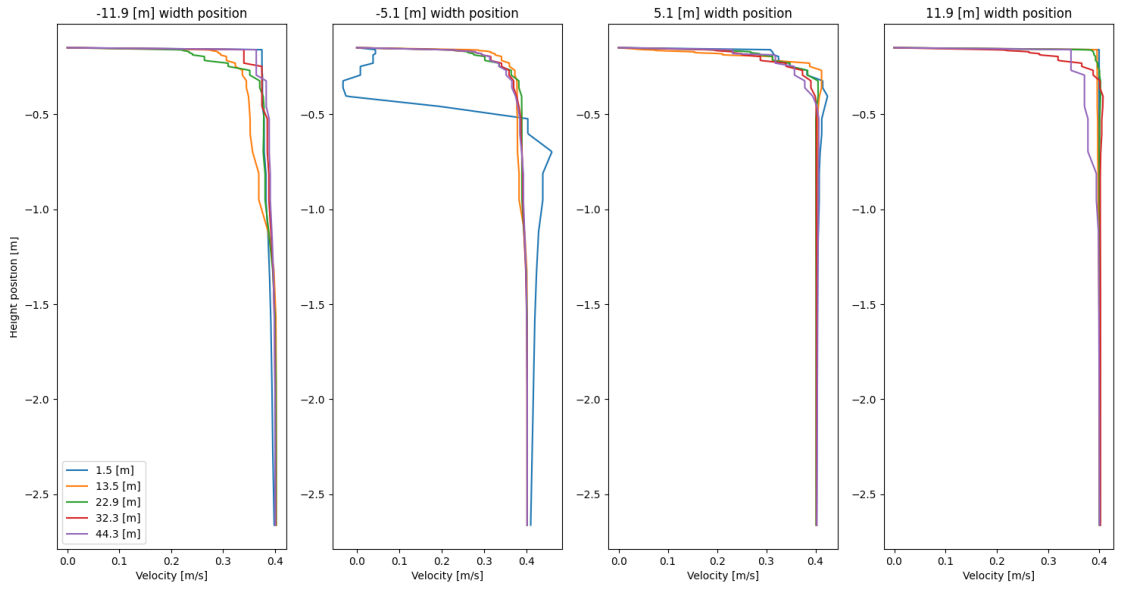


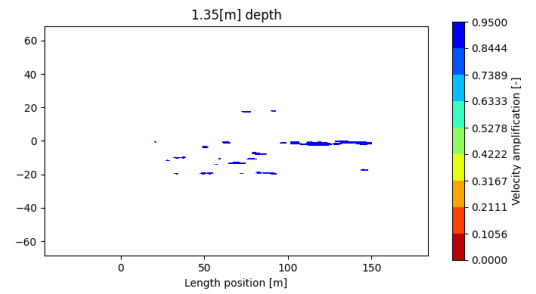
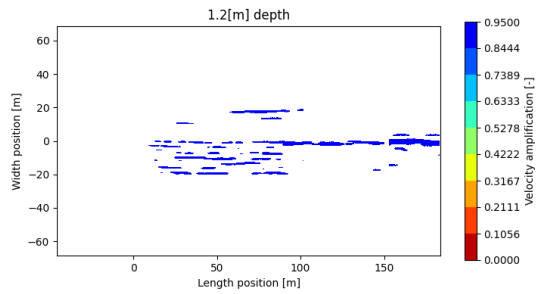
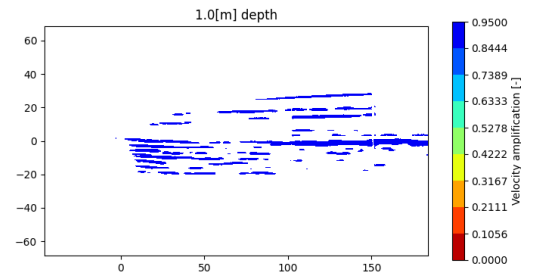
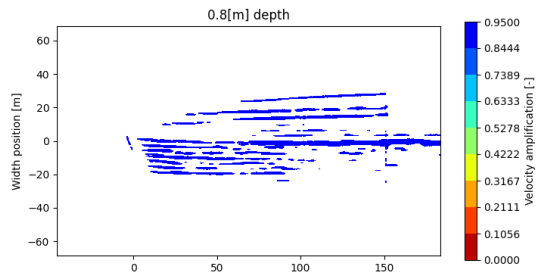
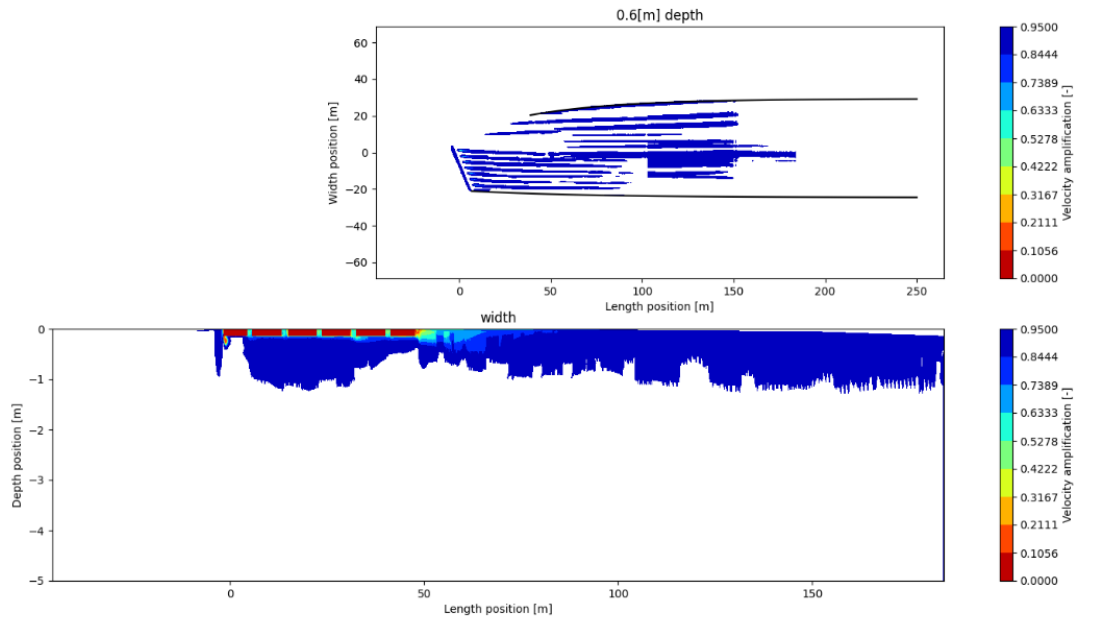


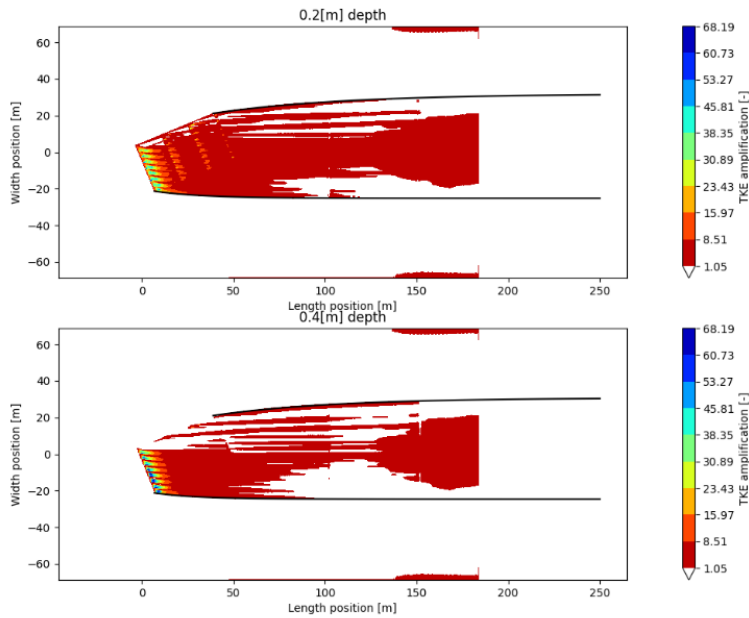
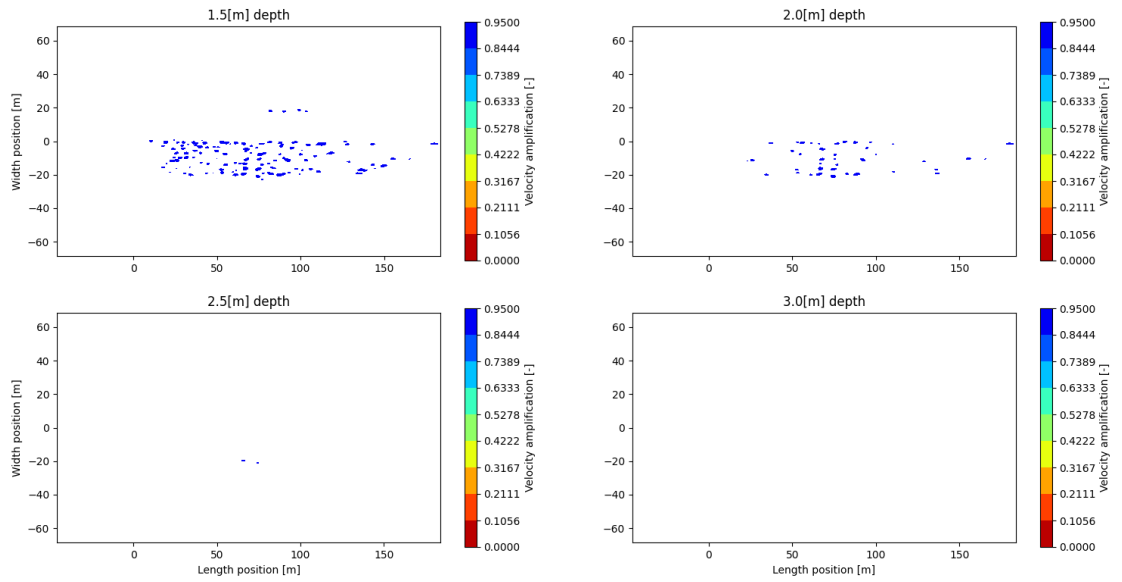


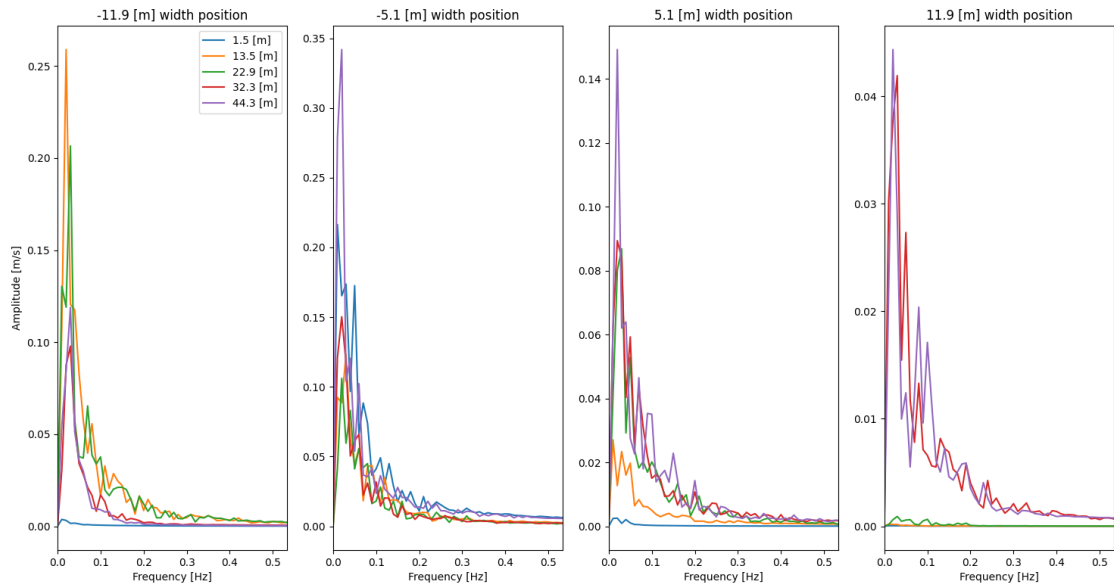
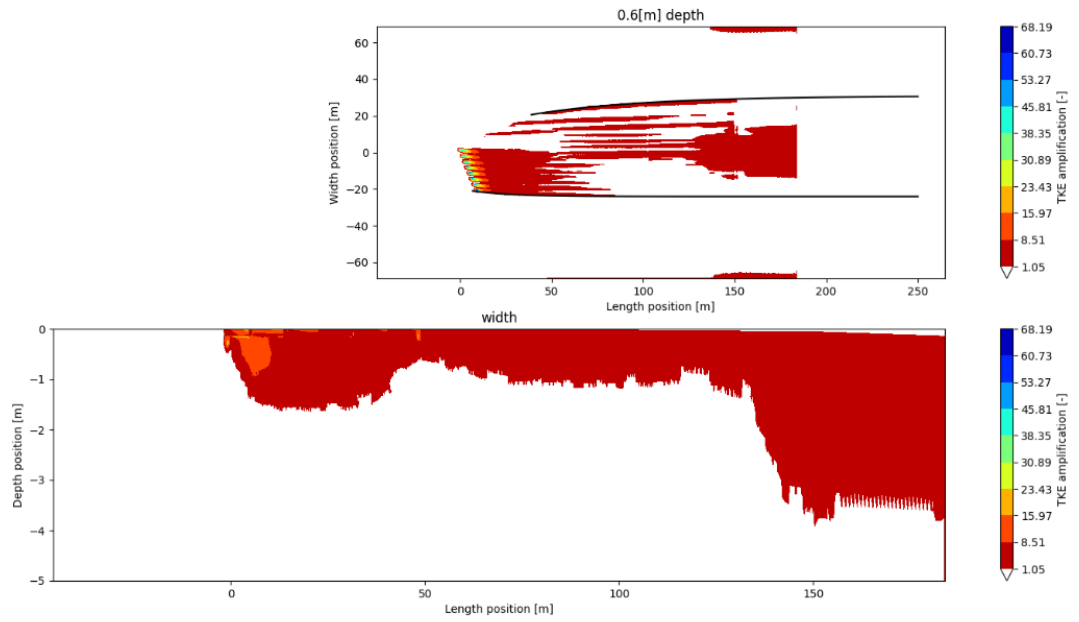


A.2.2 22.5 degree – 0.4 m/s

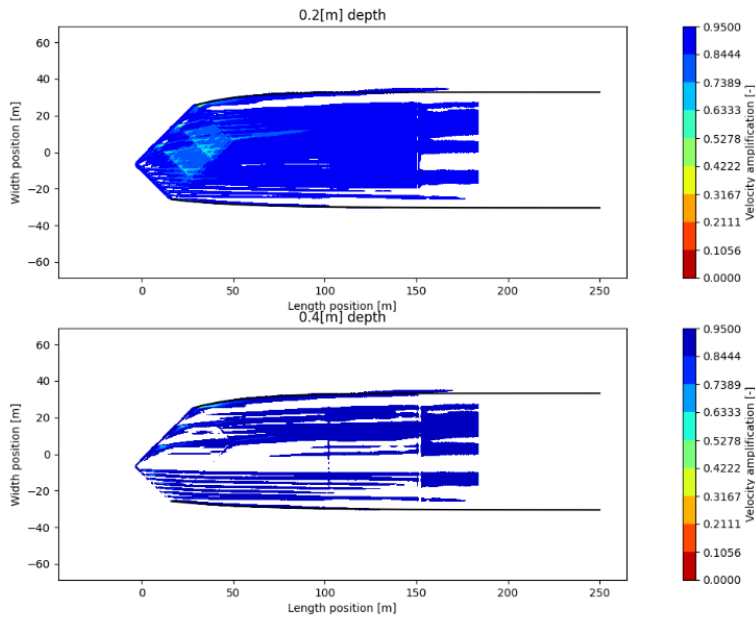
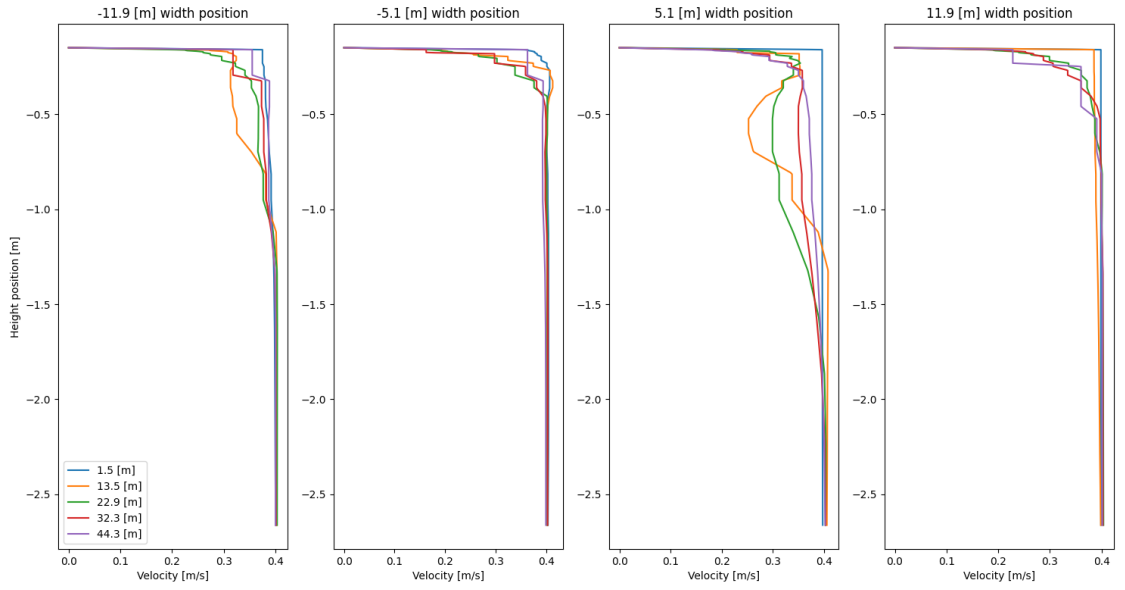


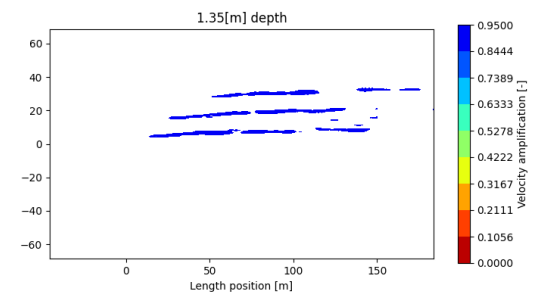
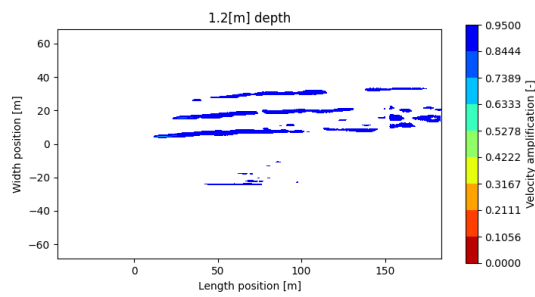
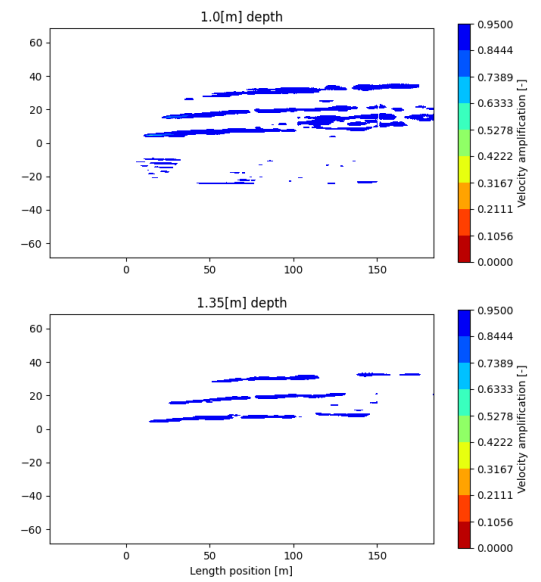
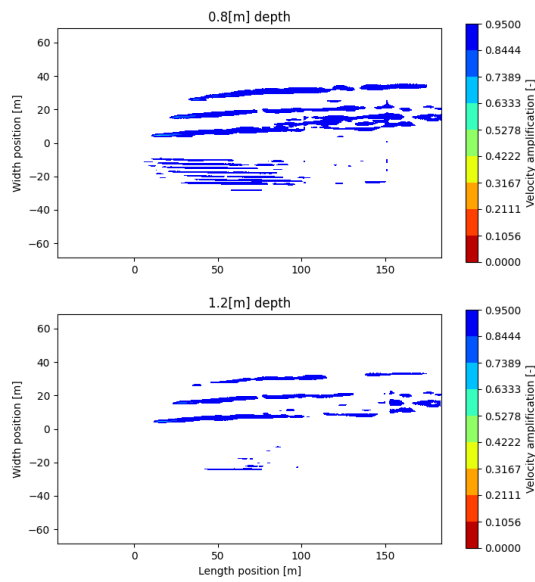
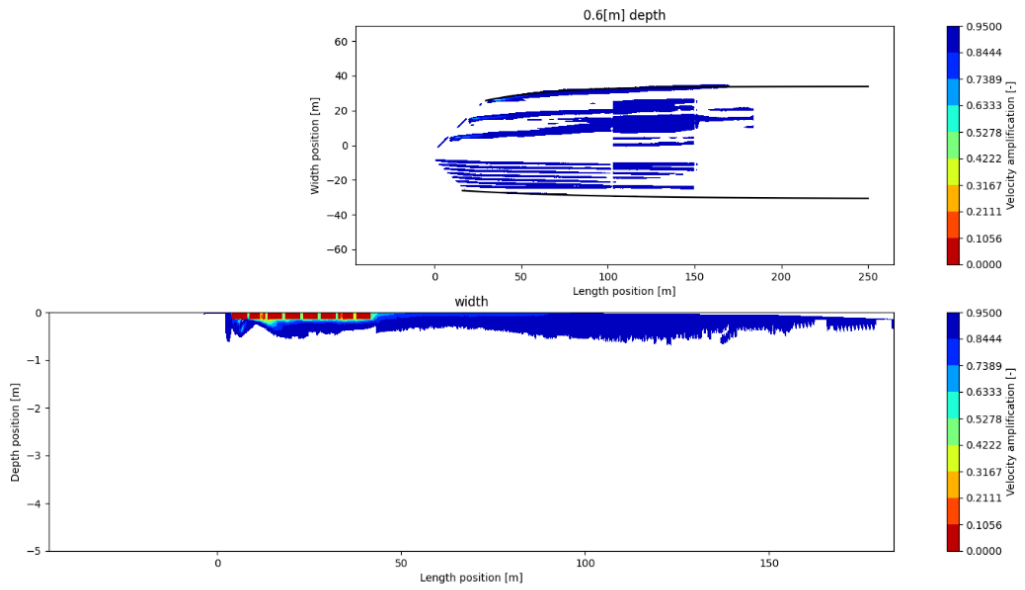


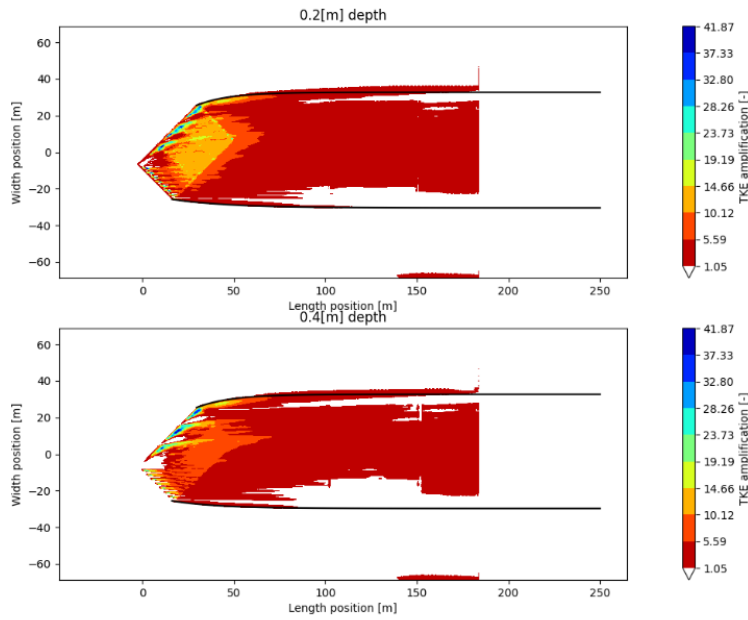
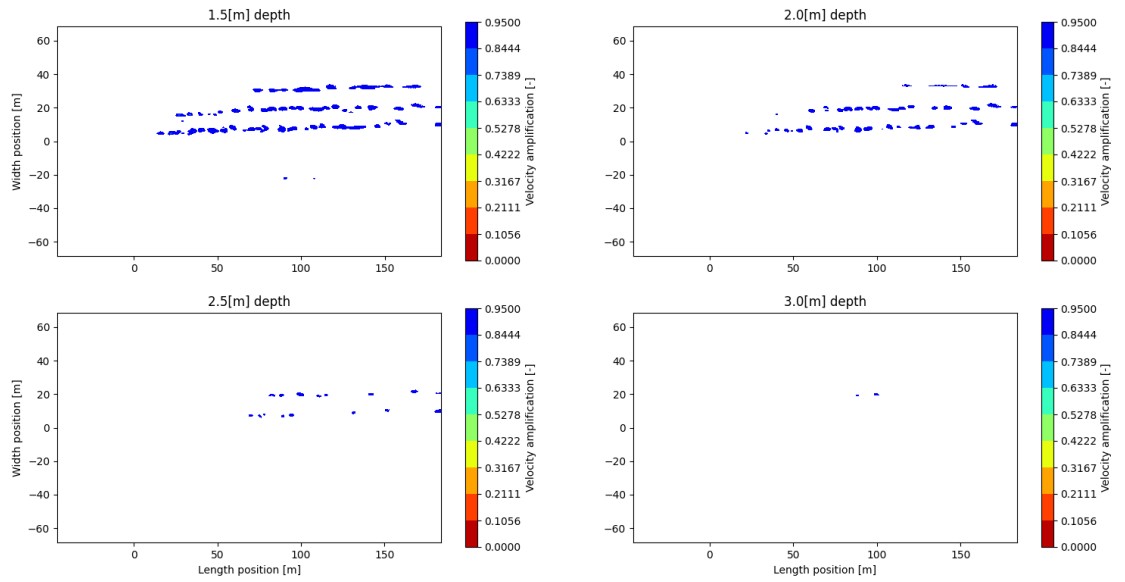


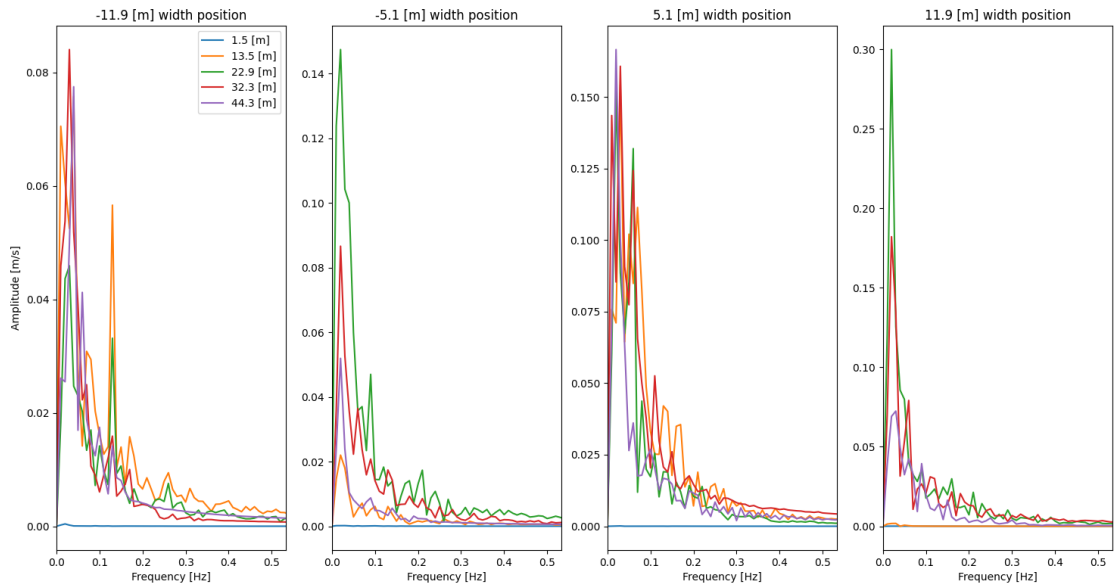
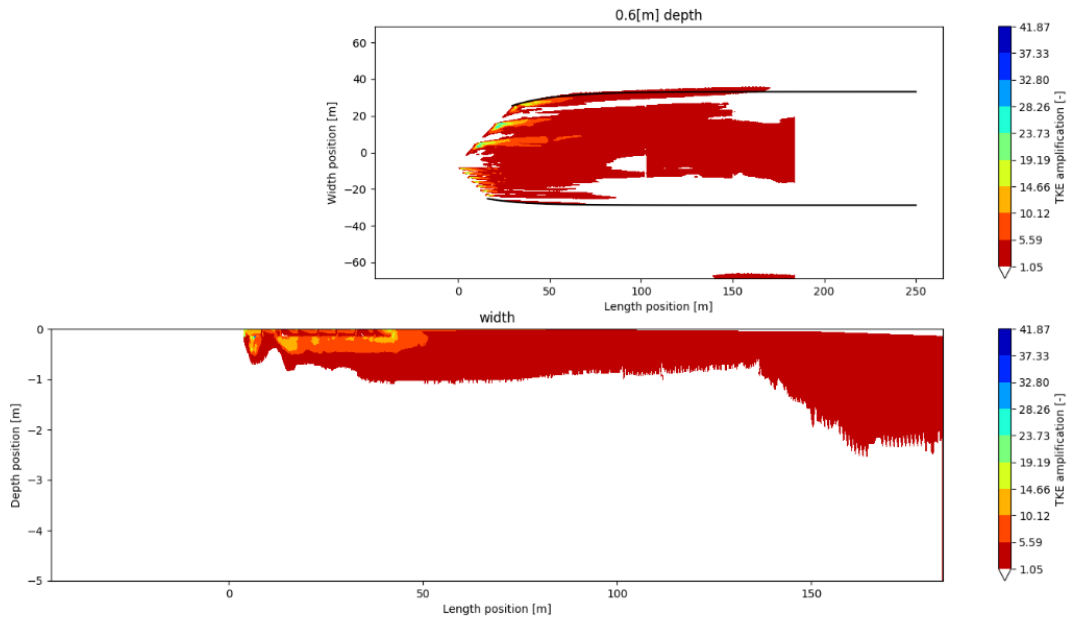


A.2.3 45.0 degree – 0.4 m/s

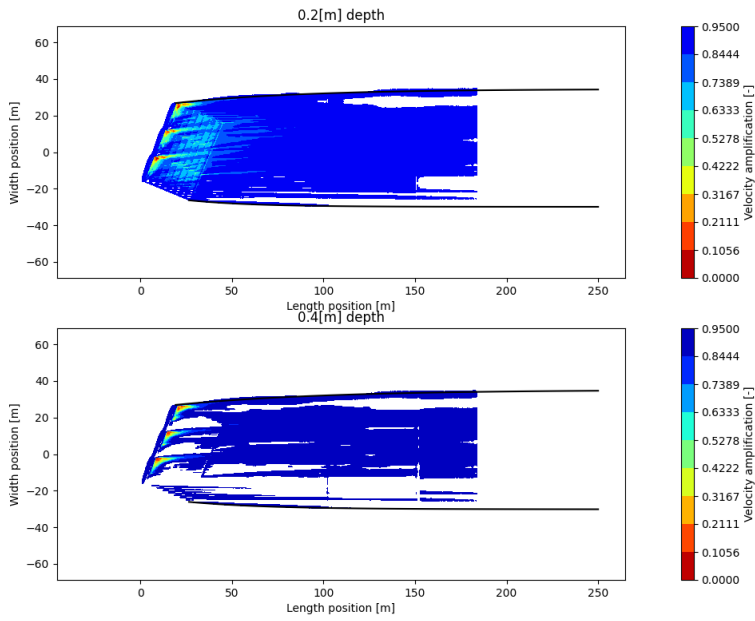
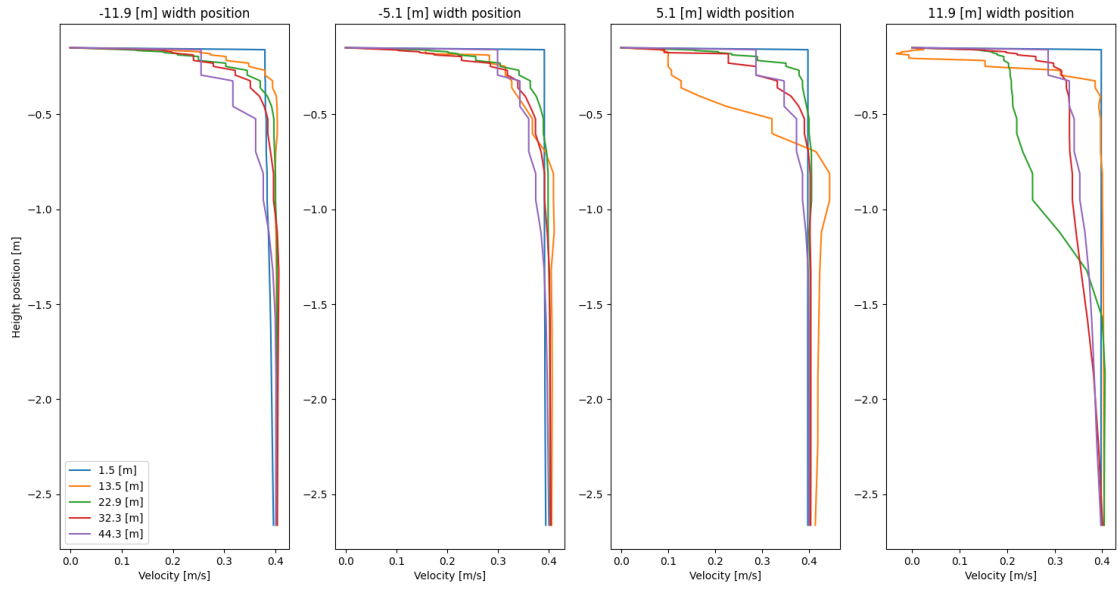


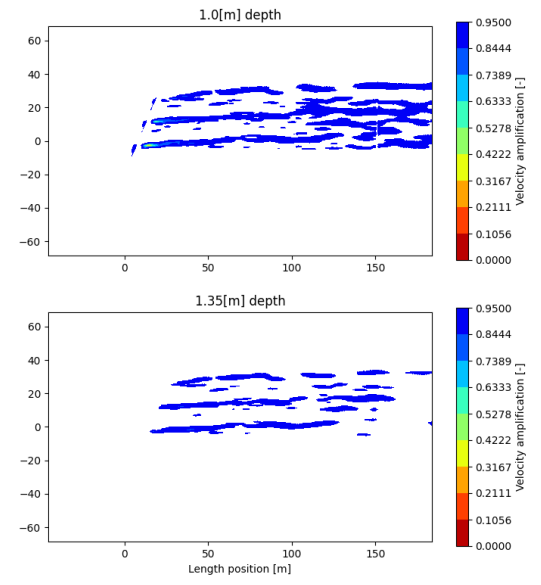
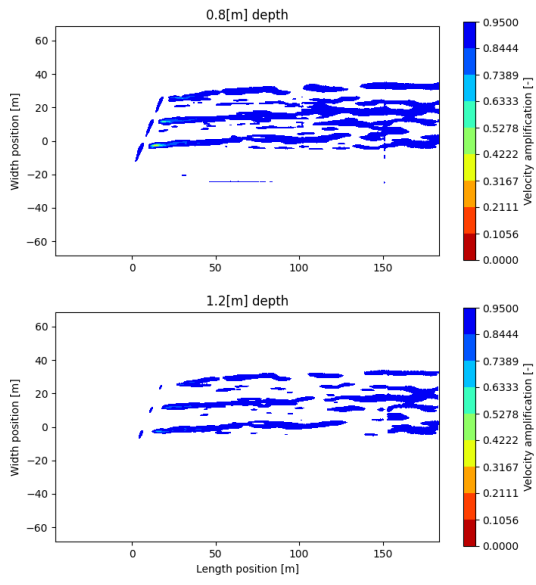
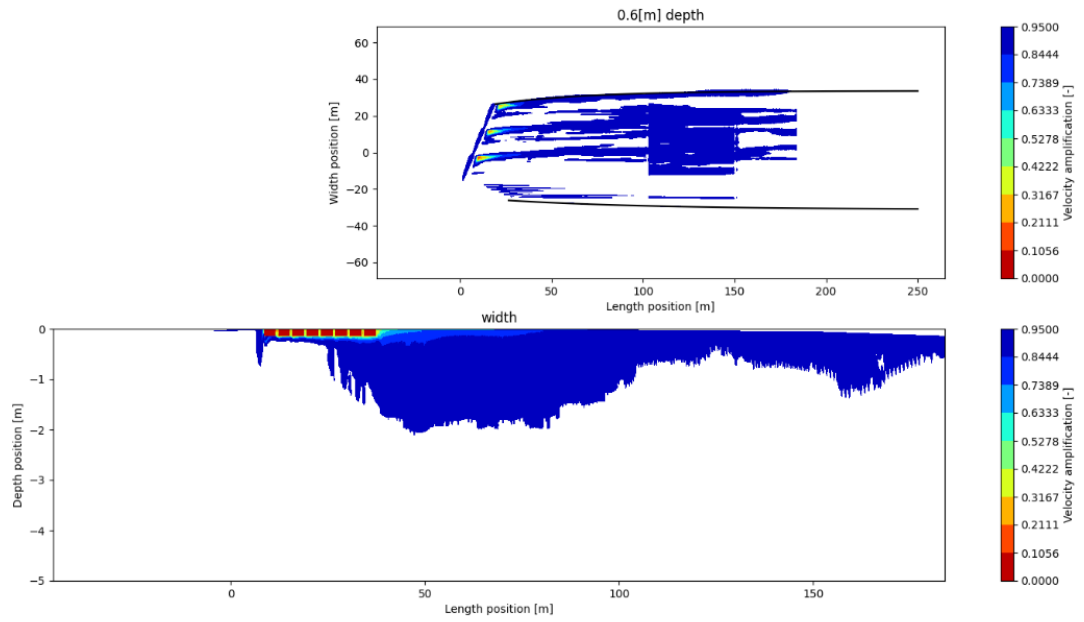


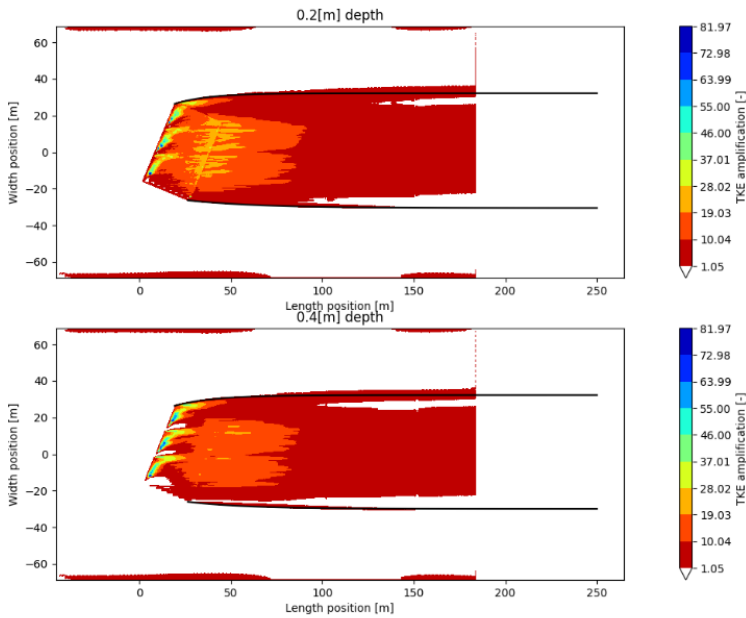
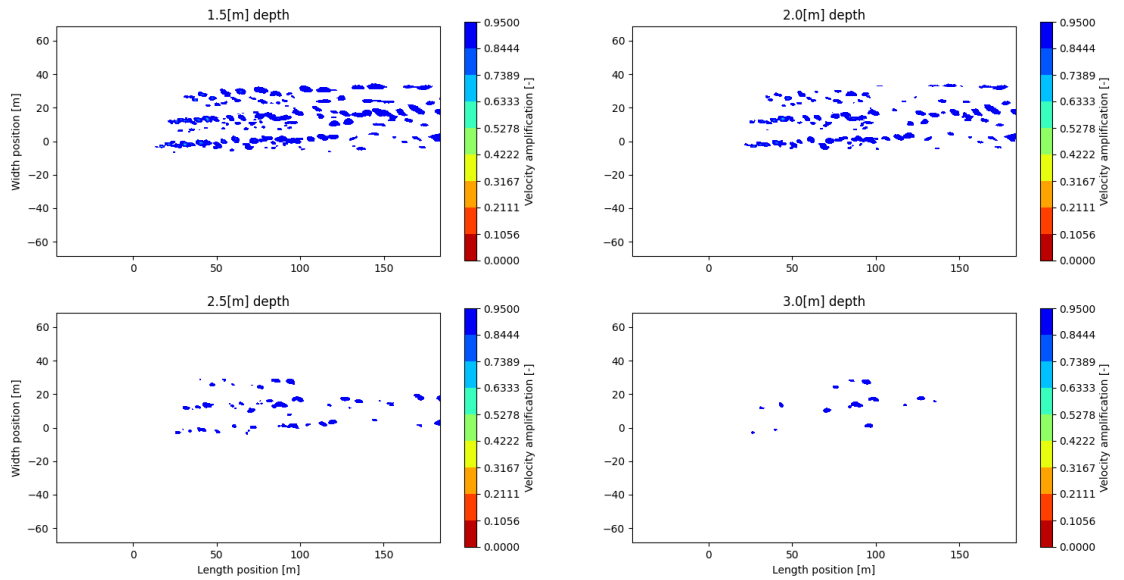


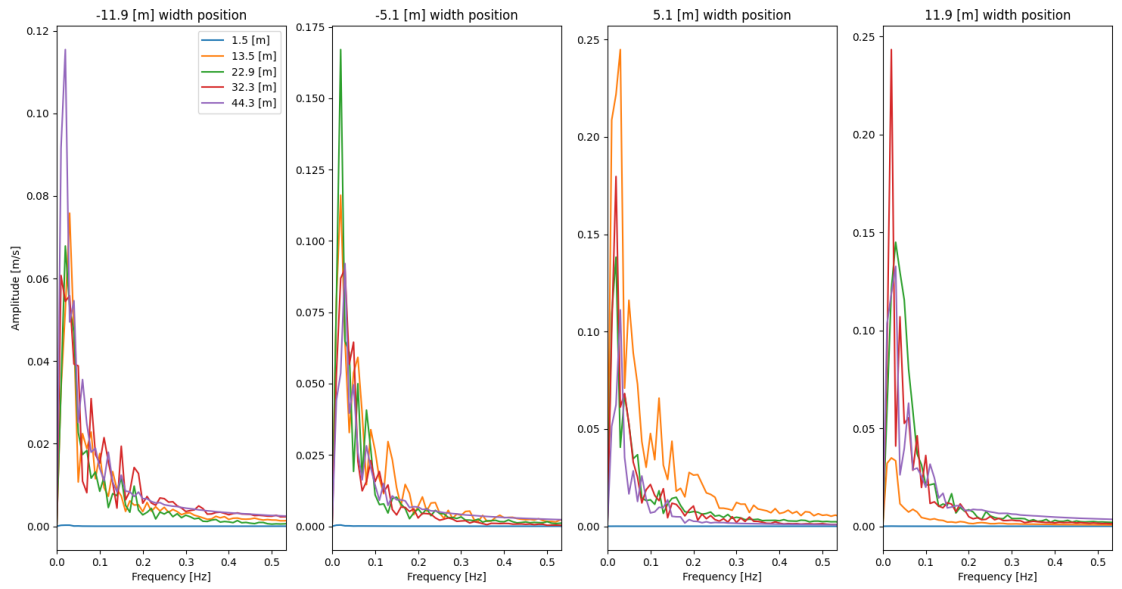
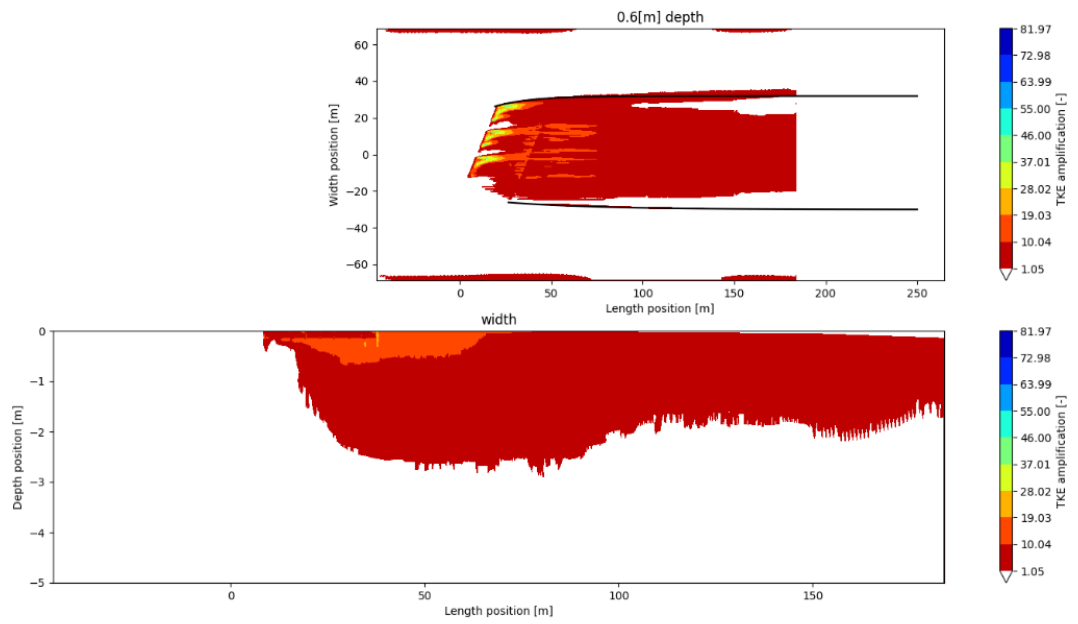


A.2.4 67.5 degree – 0.4 m/s

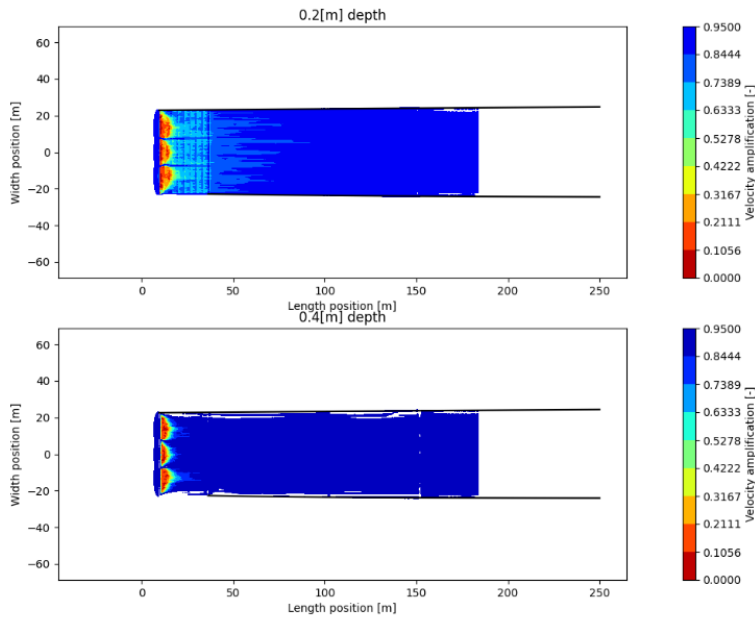
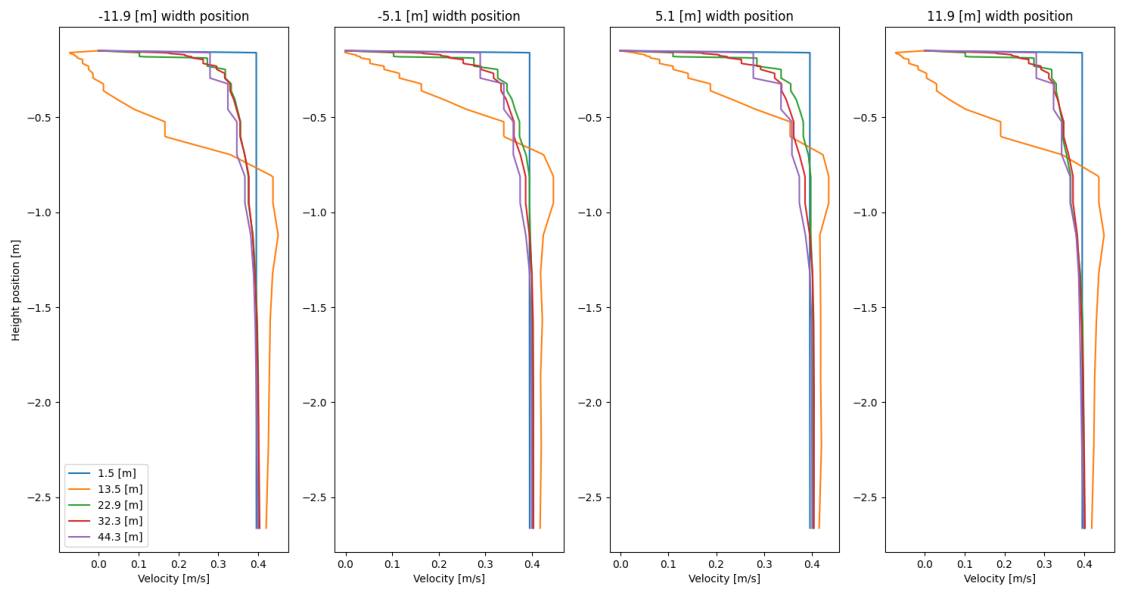


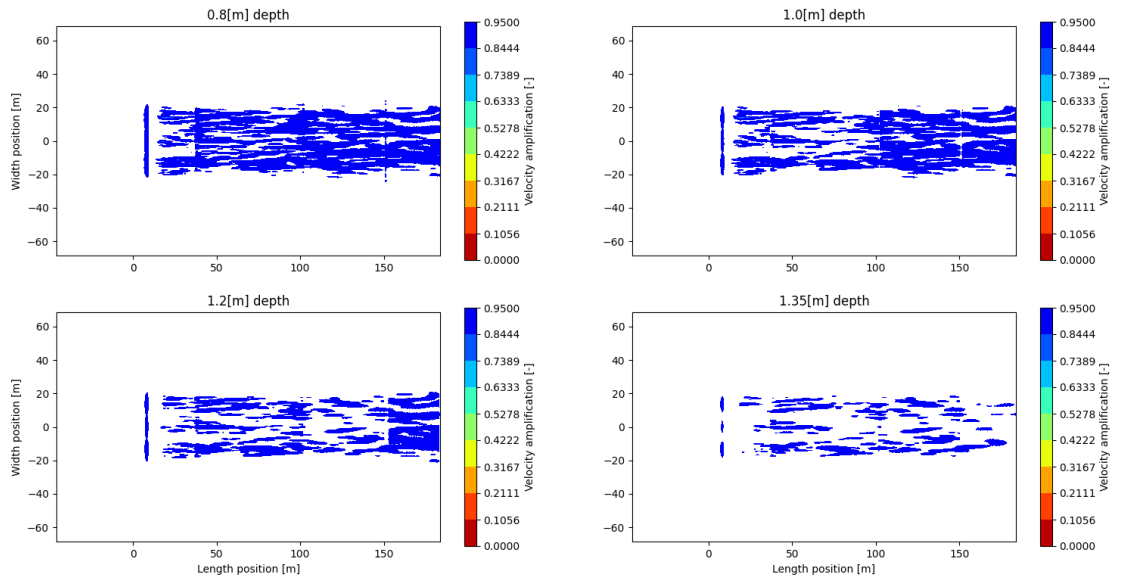
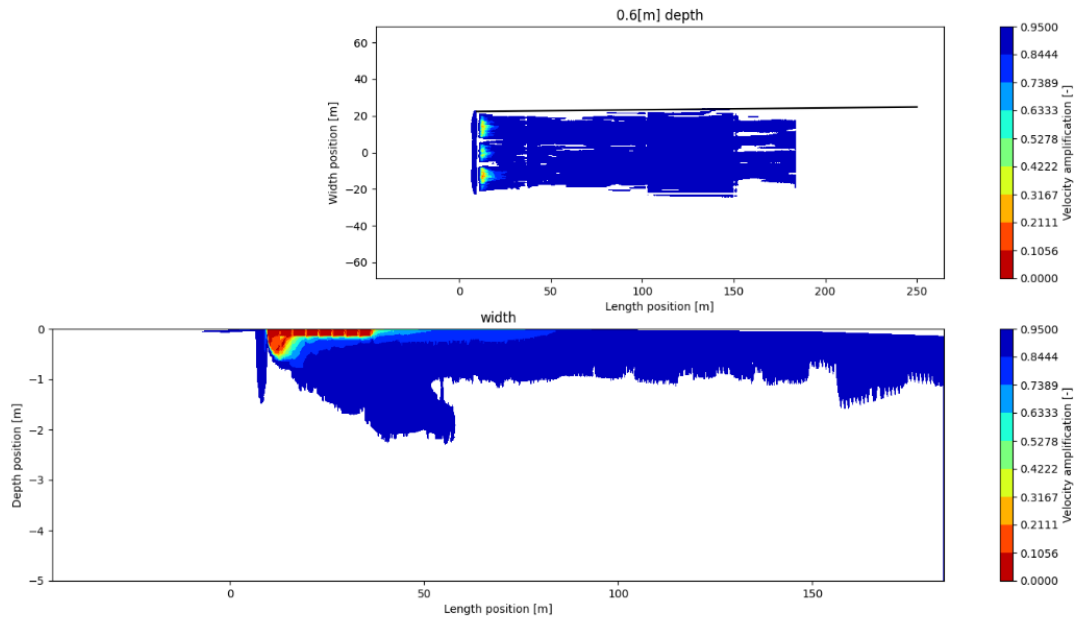


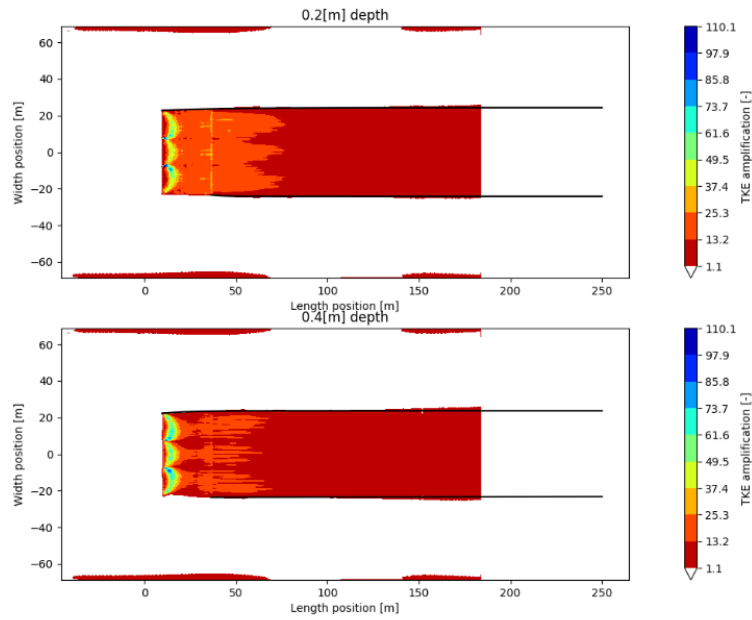
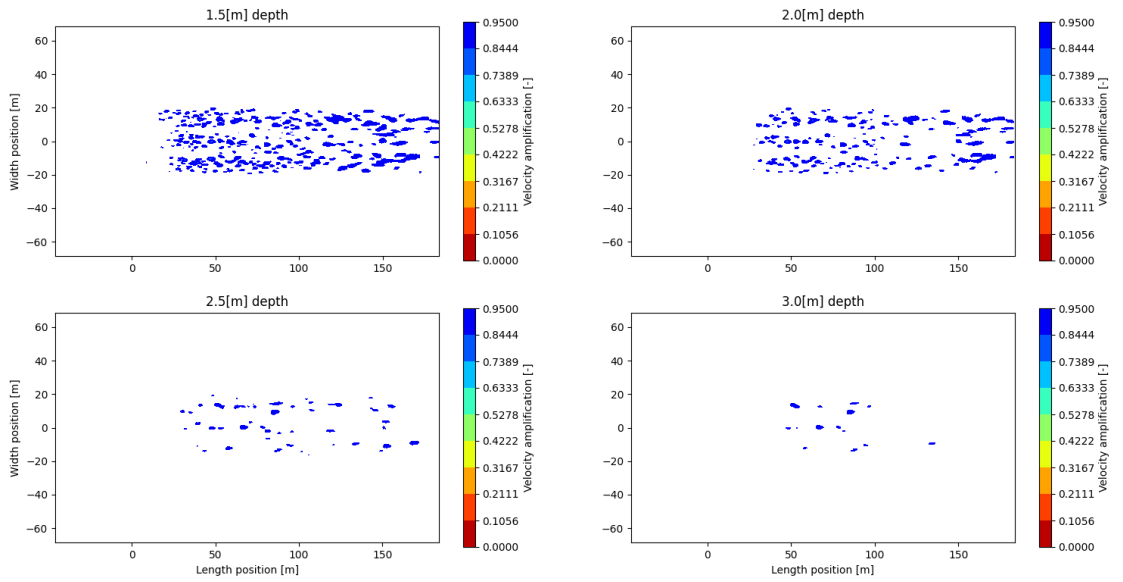


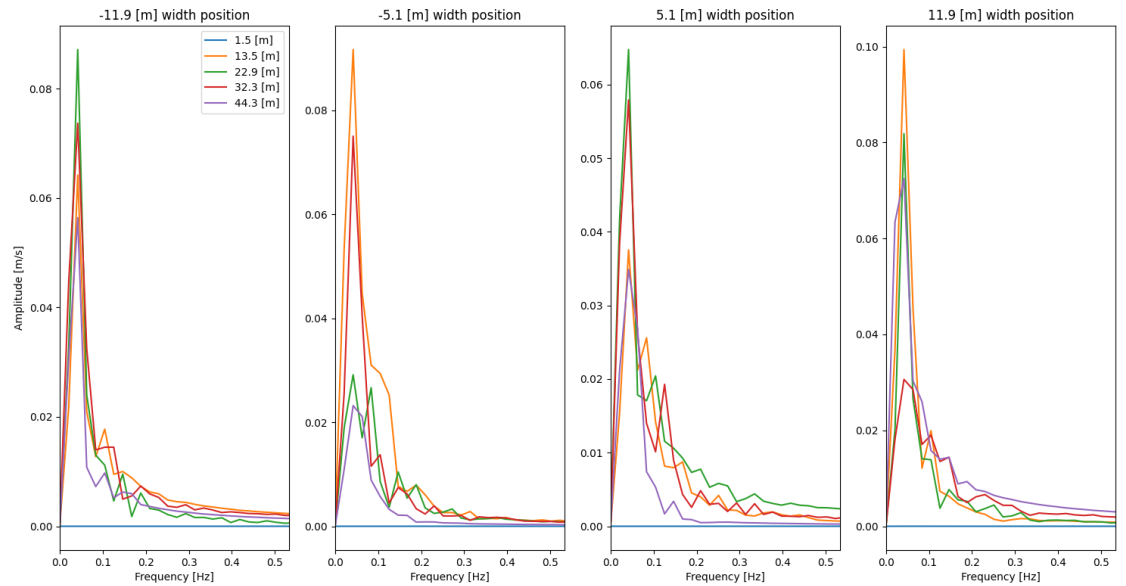
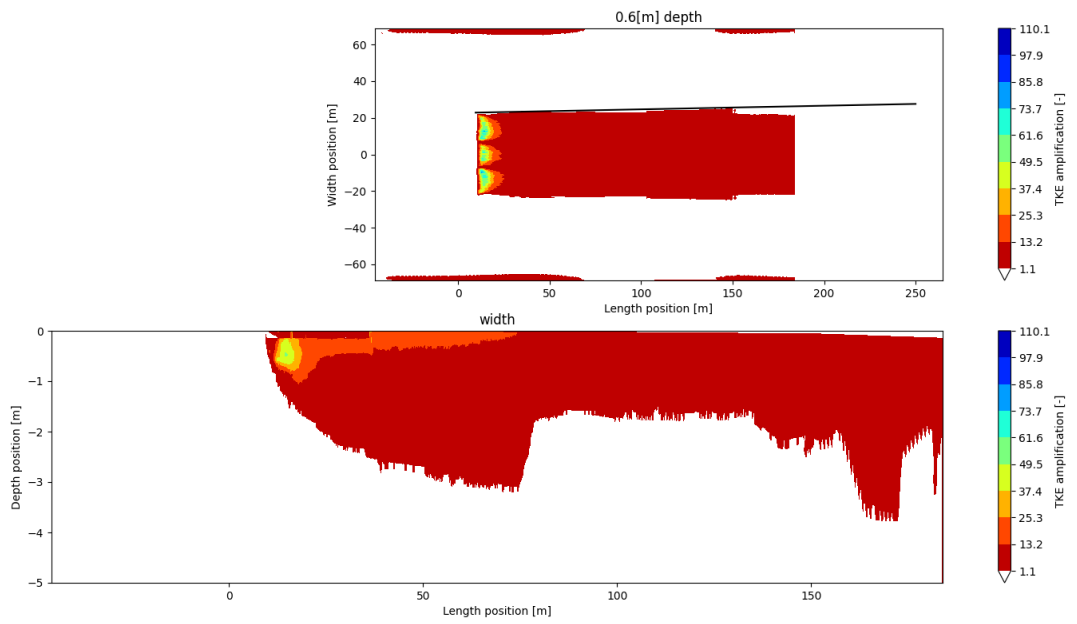


A.2.5 90.0 degree – 0.4 m/s

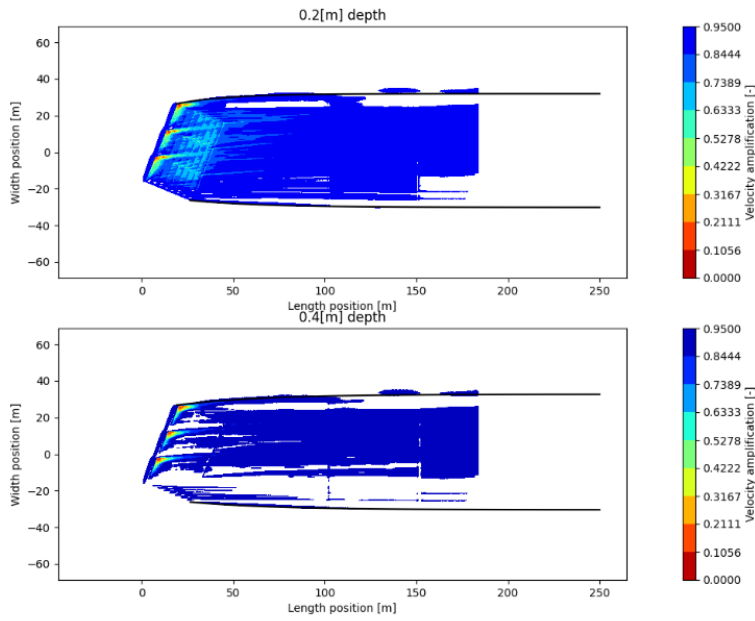
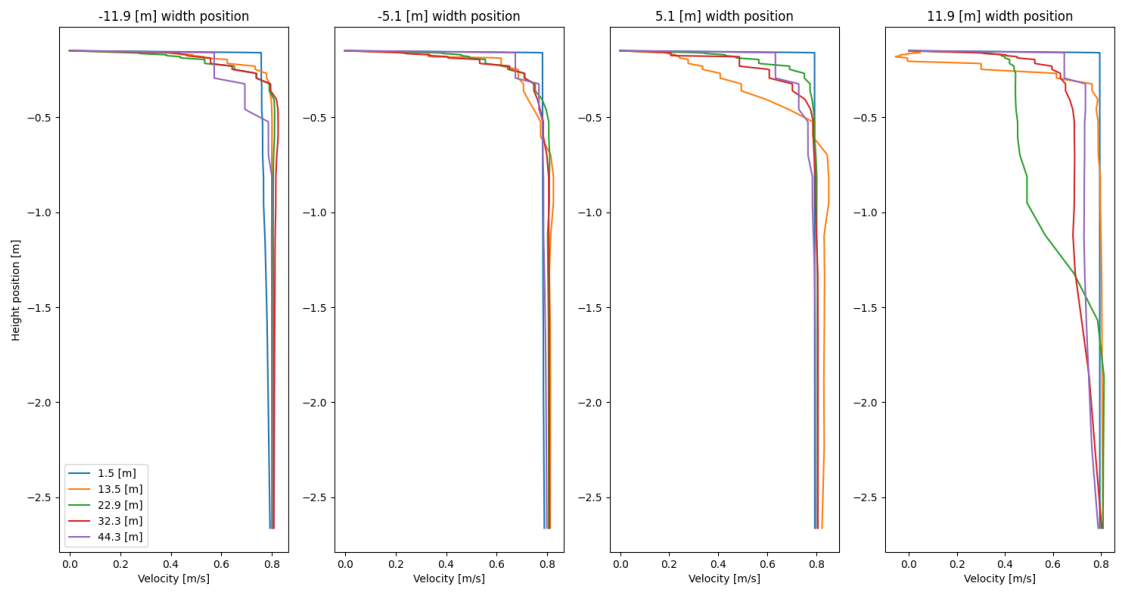


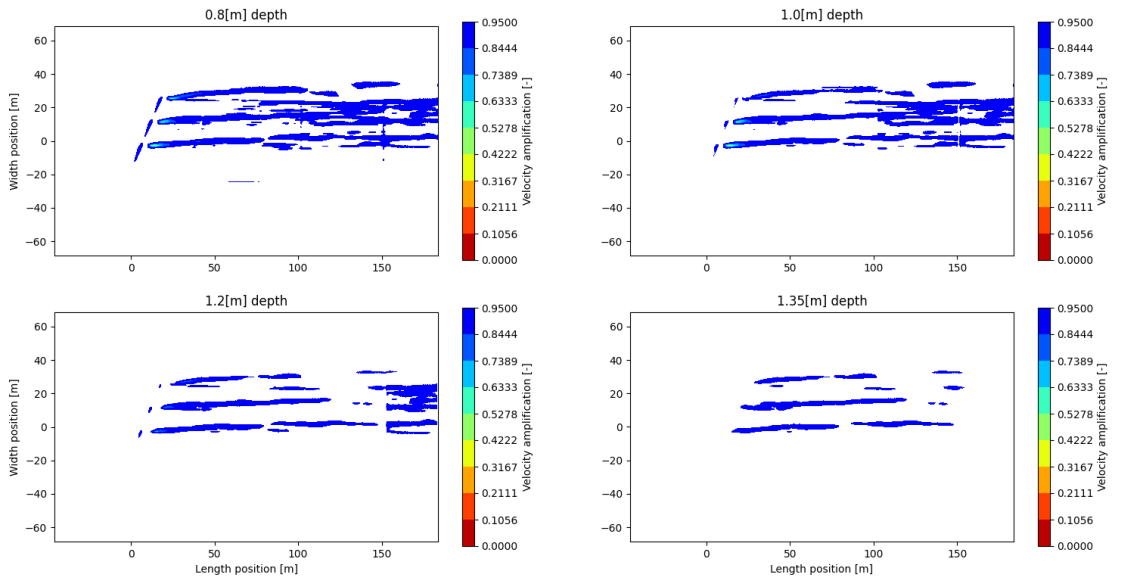
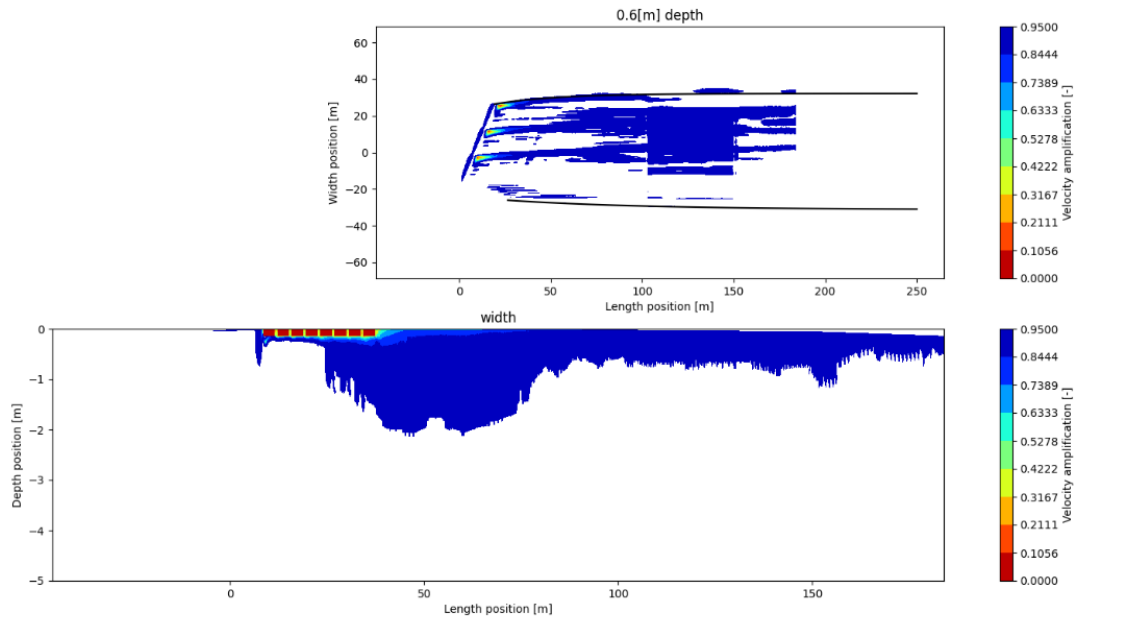


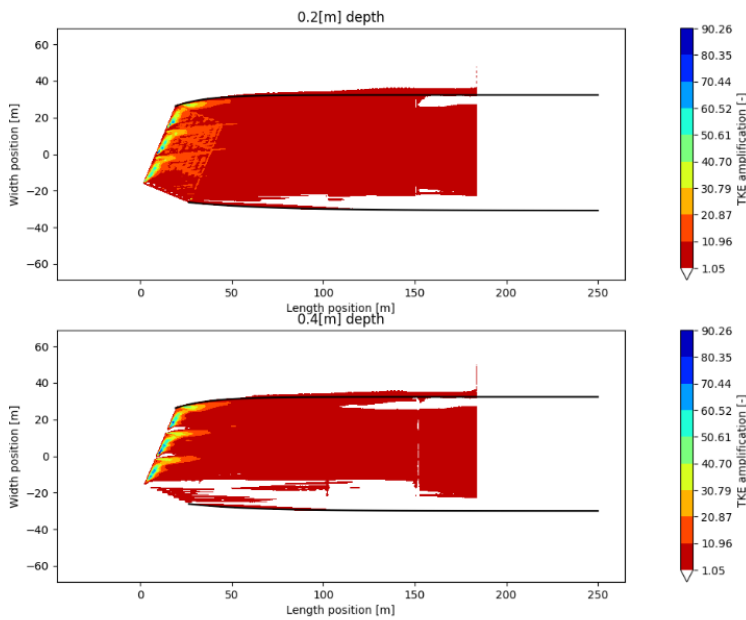
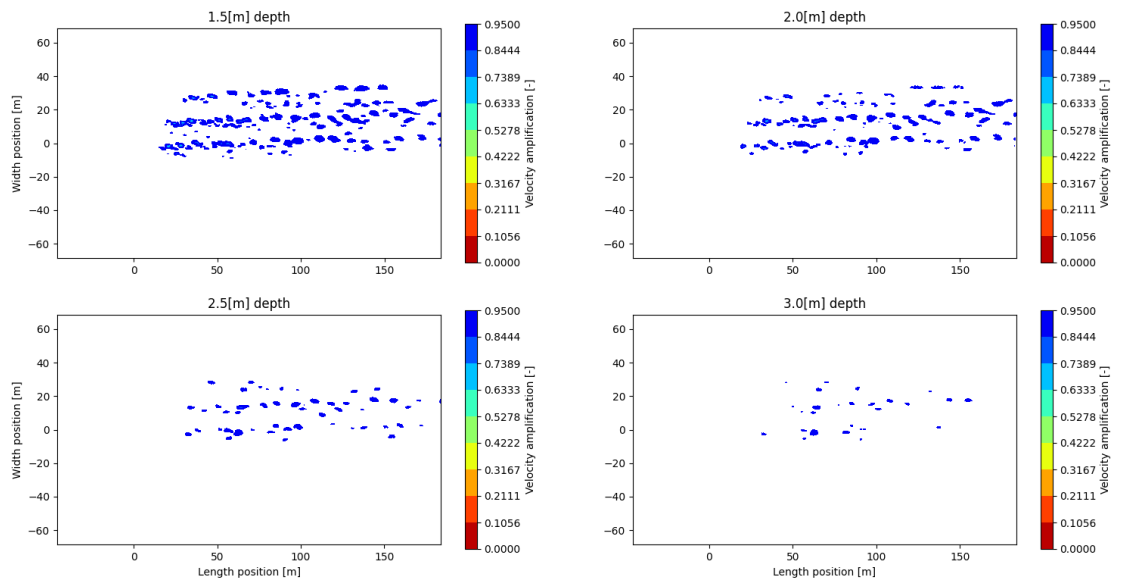


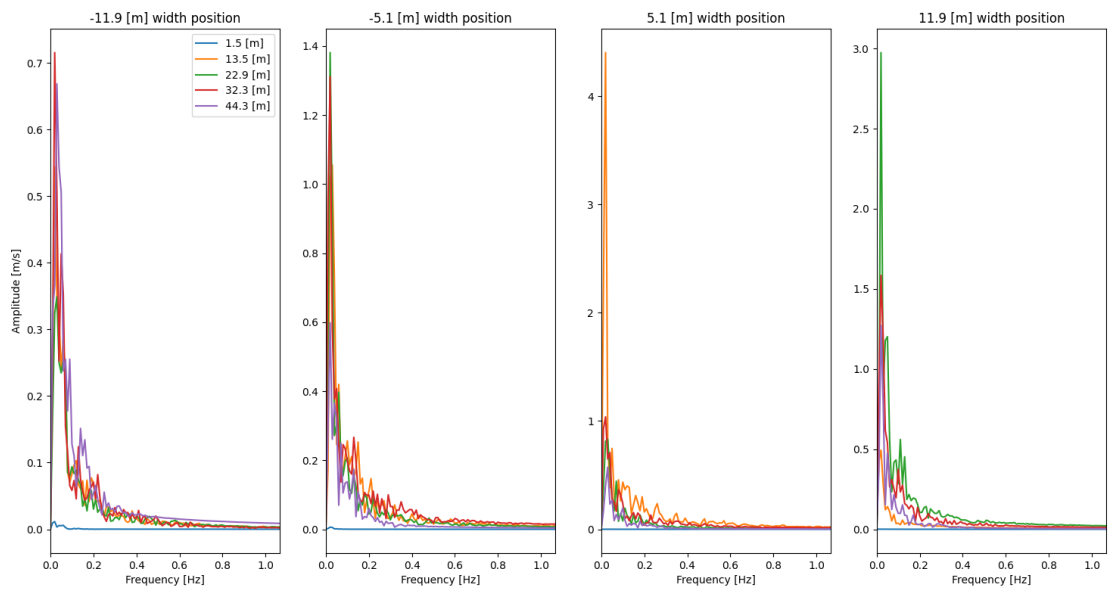
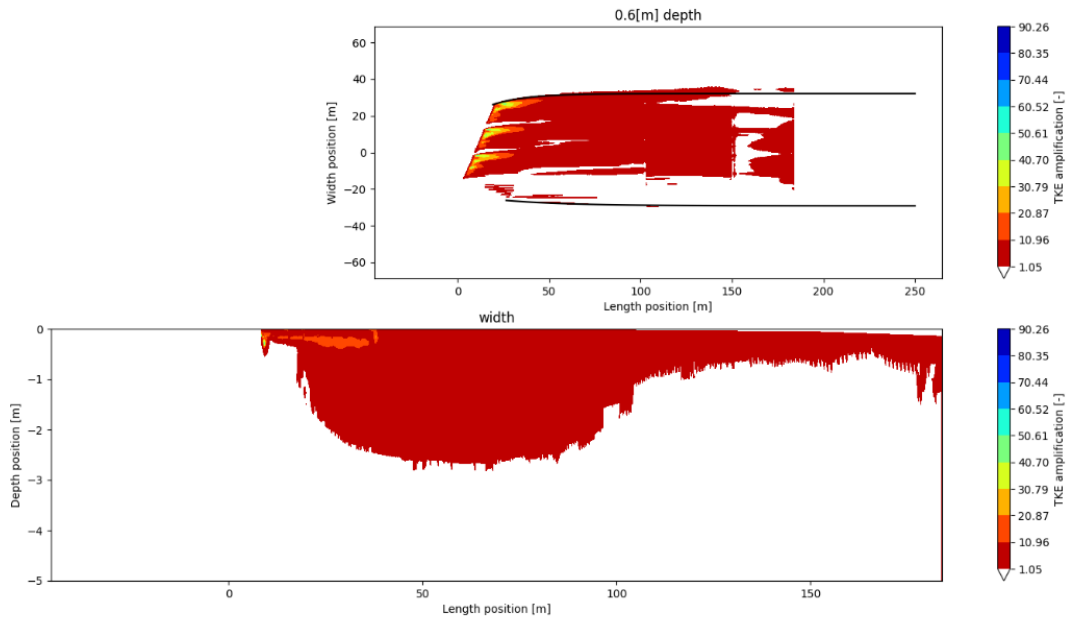


A.2.6 67.5 degree – 0.8 m/s









Deltares is an independent institute for applied research in the field of water and subsurface. Throughout the world, we work on smart solutions for people, environment and society.

Deltares

www.deltares.nl